University of Bergen, Geophysical Institutt

Master thesis

Origin of moisture at Arctic sites

By: Trine Jonassen

Supervisor: Harald Sodemann

June 1, 2016

Abstract

The hydrological cycle is an important component in the understanding of the climate system, and a good understanding of the moisture transport in the atmosphere is important in a changing climate. The climate change may have large impact on the Arctic sites.

In this thesis we look at the moisture source for NEEM (North Greenland Eemian Drilling Project) in Greenland (77.45°N, 51.05°W, 2484m a.s.l.) and Tustervatn in Norway (65.83°N, 13.92°E, 439m a.s.l.), by diagnosing the origin of moisture through calculations of a back trajectory, and compare with the interpretation of stable isotope measurements.

Stable water isotopes are natural tracers in the global water cycle, and are powerful tools to assess the atmospheric water cycle. The processes involved in stable isotopes is however highly complex, and not fully exploited. This study can be considered as an approach to finding the mean conditions of the moisture source for two Arctic sites, and to investigate and increase the understanding of the stable isotopes.

The moisture sources to NEEM and Tustervatn show differences in the transport, between an inland location and a location near the coast, and agreements in their seasonal cycles, e.g. of the moisture uptake. The two Arctic sites also show a clear change from local moisture uptake in the winter to moisture transport from lower latitudes in the summer.

The secondary isotope parameter, d-excess, is found to have a high correlation with the latitude, and clear dependencies with the temperature and humidity from the evaporation site and the land fraction. The stable isotopes, δD and δ^{18}O, are found to have the highest dependencies with the temperature and humidity.

Acknowledgements

I would like to thank my supervisor Harald Sodemann. Thank for all help and guidance through this thesis.

And a thanks to all my co-student at the Geophysical Institute, for making the past years so fun and interesting.

Contents

Chapter 1

Introduction

The hydrological cycle is an important component in the understanding of the climate system. As reliable water resources are crucial for humanity, it is important to have a good knowledge of the moisture transport in the atmosphere. The hydrological cycle helps us connect the dominant water reservoir with the land surface through evaporation and precipitation. A good understanding of the mechanism governing the moisture transport in the atmosphere is even more important in a changing climate (Christensen and Christensen, 2003). Climate change may also have large impact on the freshwater reservoirs in high latitudes. The large freshwater reservoirs are important for both the global sea level and the salinity in the surrounding oceans, especially changes in the mass balance of Greenland.

The aim of this thesis is to look at the moisture source for NEEM (North Greenland Eemian Drilling Project) in Greenland (77.45°N, 51.05°W, 2484m a.s.l.) and Tustervatn in Norway (65.83°N, 13.92°E, 439m a.s.l.), by diagnosing the origin of moisture through calculations of a back trajectory, and compare with the interpretation of stable isotope measurements. The location of NEEM and Tustervatn are shown in Figure 1.1. The reason for choosing NEEM and Tustervatn was their difference in climate and location; Tustervatn is located near the coast while NEEM is located inland.

Stable water isotopes are natural tracers in the global water cycle, and are powerful tools to assess the atmospheric water cycle (Gat, 1996). Measurements can provide insight about the storm physics, water transport and the moisture source (Dansgaard, 1964). Measurements of stable water isotopes from ice cores is also used to gain information about the long-term temperature changes. Because of this, analyzing stable water isotopes is a useful technique to asses past climate variability, and the atmospheric water cycle. The dynamical and microphysical processes involved in stable isotopes are however highly complex, and together with the sparsity of the measurements, the stable water isotopes used as meteorological recorders are not fully exploited (Duetsch *et al.*, 2013).

A secondary isotope parameter, deuterium excess (d-excess) was defined by Dansgaard (1964). It is recognized as a tracer to identify the moisture source, by preserving the condition from the evaporation location (Gat, 1996), and is used as a tool to assess the moisture origin. The Arctic-origin moisture is investigated (e.g. Kurita 2011, Steen-Larsen *et al.* 2011) and is found to have a higher d-excess than what's observed at lower latitudes.

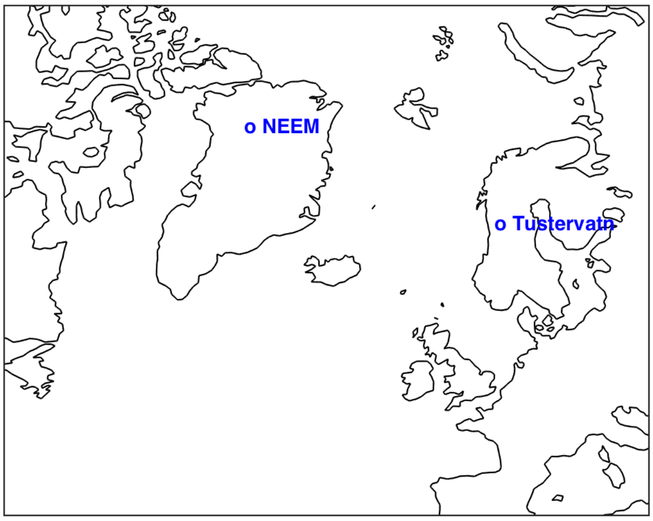

Figure 1.1: Map showing the location of NEEM (77.45°N, 51.05°W, 2484m a.s.l.) in Greenland and Tustervatn (65.83°N, 13.92°E, 439m a.s.l.) in Norway.

Since the d-excess is highly distinct it can be used as a tool to assess the moisture coming from higher latitudes. Several other studies are also conducted to look for characteristic in the d-excess value (e.g. Werner *et al.* 2001, Cappa *et al.* 2003, Benetti *et al.* 2014, Samuels-Crow *et al.* 2014). Observations of the relationship between d-excess and the ocean surface conditions are still limited (Uemura *et al.*, 2008), and there is still controversy around the d-excess as an isotopic parameter. Comparing the d-excess to the meteorological and isotopic observations could therefore give a better understanding of the local mechanism and advection that are important contributers to the d-excess.

To diagnose the origin of the moisture reaching the Arctic sites, a method for analyzing the water transport introduced by Sodemann *et al.* (2008) will be used. Through a back trajectory, changes in the specific humidity for an air parcel will tell us about the precipitation and evaporation to the air parcel. The aim of this model is to identify the location of the moisture uptake and estimate how much each uptake or precipitation contributes to the total moisture increase or decrease. This makes it possible to look for the variability of the isotopic composition and the effect from the source region.

The Lagrangian moisture source diagnostic introduced by Sodemann *et al.* (2008), have earlier been used to trace precipitation. Here the Lagrangian moisture source diagnostic is used both for tracing precipitation and atmospheric vapour. Using this method for tracing the atmospheric vapour has not earlier been done.

This study can be considered as an approach to finding the mean conditions of the moisture source for NEEM and Tustervatn, and to investigate and increase the understanding of the stable isotopes.

The thesis is structured as follow: Chapter 2 present a general description of the stable isotopes in the atmospheric water cycle. The Lagrangian moisture source diagnostic used to diagnose the origin of the moisture reaching the Arctic sites is introduced in Chapter 3. The study sites are presented in Chapter 4. Chapter 5 presents our result for the moisture transport to the two Arctic sites, and a comparison of the isotopic observations with meteorological observations and moisture sources. Further discussion and conclusion are given in Chapter 6.

Chapter 2

Background - Stable Isotopes of water

2.1 Background and definitions

Isotopes are atoms with the same number of protons and electrons but with different number of neutrons. Different isotopes therefore has similar charge, but differ in weight. The most abundant isotopes in the atmosphere are ^{16}O and ^{2}H, with an abundance of 99.76% and 99.985%. ^{18}O and ^{2}H (also called Deuterium, D) are also of great significance, with respectively 0.200% and 0.015%. The corresponding molecules are deuterated water (HDO) and heavy-oxygen water ($H_2^{18}O$). The isotopes ^{17}O and ^{3}H plays a minor roles in the atmosphere.

To quantify the ratio between the rare isotope and the abundant isotope in a volume a quantity known as the isotopic ratio R is used. R is calculated from the concentration of the rare molecule divided by the concentration of the abundant molecule. For the rare isotope $H_2^{18}O$ and the abundant isotope $H_2^{16}O$ it will look like:

$$^{18}R = \frac{amount\ of\ rare\ isotope}{amount\ of\ abundant\ isotope} = \frac{[H_2^{18}O]}{[H_2^{16}O]} \tag{2.1}$$

As a result of different mass between the isotopes, a separation of the isotopes from naturally occurring processes could happened. Mass differences could change the physical properties of the element, e.g. melting point, vapour pressure and density. Processes such as evaporation or condensation, melting or crystallization will lead to separation. This separation of the isotopes is being called isotopic fractionation, and is further explained in chapter 2.4.

Since fractionation processes could lead to isotopic enrichment and depletion, it is useful to express the isotope as isotope relative ratio (δ), relative to a standard. In the atmosphere this standard is the Vienna Standard Mean Ocean Water (VSMOW).

$$\delta^* = \left(\frac{R_{Sample} - R_{std}}{R_{std}}\right) \cdot 1000 = \left(\frac{R_{Sample}}{R_{std}} - 1\right) \cdot 1000 \quad (‰) \tag{2.2}$$

Where δ^* would denote $\delta^{18}O$ or δD, and R_{sample} and R_{std} are the isotopic ratio of the sample and the standard.

$\delta^* > 0$ indicates that the sample is enriched in heavy isotopes, meaning that the sample will have more heavy isotopes than the standard. $\delta^* < 0$ indicates that the samples will be depleted.

2.2 Equilibrium fractionation

Equilibrium isotope fractionation is an reversible process and can be written A $\rightleftharpoons$ B. An equilibrium fractionation will after sufficient time be in equilibrium between the phases in the reaction.

The isotopic fractionation is driven by the different mass of the molecules involved in the reaction, mainly for two reasons: (1) molecules with heavier weight will have slower diffusion velocity and (2) molecules with larger mass favored stronger bonds (solid > liquid > vapour) (Sodemann, 2006).

The ratio of the two phases in the isotopic equilibrium is calculated by the equilibrium fractionation factor, α:

$$\alpha_{v/l} = \frac{R_v}{R_l} \tag{2.3}$$

The equilibrium fractionation factor is a constant for the equilibrium reaction, telling the effectiveness of the reaction to either side.

The value $\alpha_{v/l}$ displays where the heavy isotopes are displaced. For $\alpha_{v/l} < 1$ the heavy isotopes will be shifted towards the liquid phase, and for $\alpha_{v/l} > 1$ the heavy isotopes will be shifted towards the vapour phase.

For the atmosphere the only depending factor for the equilibrium fractionation is the temperature. The temperature dependency is most crucial for low temperatures, meaning that $\alpha_{v/l}$ will be smaller for lower temperatures. For high temperatures the rotational and vibrational modes in the molecule will increase, leading to higher equilibrium fractionation factor.

2.2.1 Non-equilibrium fractionation

Non-equilibrium isotopic fractionation or kinetic fractionation is an irreversible process, and can be written A $\rightarrow$ B. A non-equilibrium reaction takes place when the phase change cannot reach equilibrium, and will be forced toward one side of the reaction.

Diffusion velocities are essential for non-equilibrium fractionation. The heavier isotopes will have a slower diffusion velocity than light isotopes, which will lead to deviation from the isotopic ratios under equilibrium conditions.

Non-equilibrium fractionation in the atmosphere could have been caused by a numerous of reasons, such as the temperature of the air and water, the relative humidity gradient and the evaporative cooling (Merlivat and Jouzel 1979, Cappa *et al.* 2003).

2.3 Deuterium excess

Deuterium excess, or d-excess, is recognized as a tracer to identify the moisture source, by looking at deuterated water (HDO) and heavy-oxygen water ($H_2^{18}O$). Under equilibrium conditions a ratio of 1:8 is found between $\delta^{18}O$ and δ^2H, which originates from the binding energy of HDO being approximately 8 times stronger than for $H_2^{18}O$.

The HDO and $H_2^{18}O$ molecules will however mostly not be in equilibrium and deviate from the 1:8 ratio. This deviation was defined by Dansgaard (1964) as deuterium excess:

$$d = \delta D - 8 \cdot \delta^{18}O \tag{2.4}$$

The reason behind the deviation is the different diffusion velocities for the two molecules HDO and $H_2^{18}O$. The $H_2^{18}O$ molecule is heavier than the HDO molecule and will therefore move more slowly, and there will not be enough time to reach equilibrium conditions.

D-excess is expected to preserve the trademark from the moisture source (Dansgaard, 1964), as it is specifically sensitive to the conditions during the evaporation of water from the (ocean) surface. The reason behind this is that the isotopic composition from the moisture source is being controlled by the kinetic effects at the evaporation, related to the conditions of the surface. D-excess is especially sensitive to the wind speed, sea surface temperature and relative humidity at the evaporation site (Cappa *et al.*, 2003). The sea surface temperature could impact the fractionation from the temperature dependency of the equilibrium fractionation factor. The exact formula for non-equilbrium fractionation depending on the wind speed, sea surface temperature and relative humidity is still not know (Pfahl and Sodemann, 2014).

Steen-Larsen *et al.* (2013) points out several things that also can contribute to the d-excess; evaporation in the source region, condensation along the parcels path, cleanliness of the air, the super saturation in the clouds, and the temperature where the snow crystals begin to develop.

Both Kurita (2011) and Steen-Larsen *et al.* (2013) found in their studies from the Arctic Ocean that the moisture originating from the Arctic Ocean had higher d-excess than those originating from lower latitudes. Steen-Larsen *et al.* (2013) argued that the high d-excess originates from the cold polar air masses with low humidity crossing the sea-ice margin, will lead to strong evaporation from the open-water bodies and lead to depletion. Since the high d-excess value is largely separated from other moisture sources, it can be used as a diagnostic tool to evaluate the contribution of moisture from the Arctic (Kurita, 2011).

There is however still controversy around d-excess as an isotopic parameter. D-excess is usually treated as the signal from the evaporation location, but kinetic fractionation is also occurring in the atmosphere. The precipitation and d-excess value on a single location can be affected by evaporation from different source regions. The kinetic fractionation effect from the atmosphere is especially important in the Arctic when snow occur (Pfahl and Sodemann, 2014).

The global average d-excess is 10‰ (Kurita, 2011).

2.4 Fractionation processes

Isotopic fractionation describes processes that could alter the relative abundance of the isotopes, through separation during phase transition. Figure 2.1 illustrate the most relevant physical mechanism and their isotopic fractionation processes in the hydrological cycle, and are here briefly explained (following Sodemann (2006)).

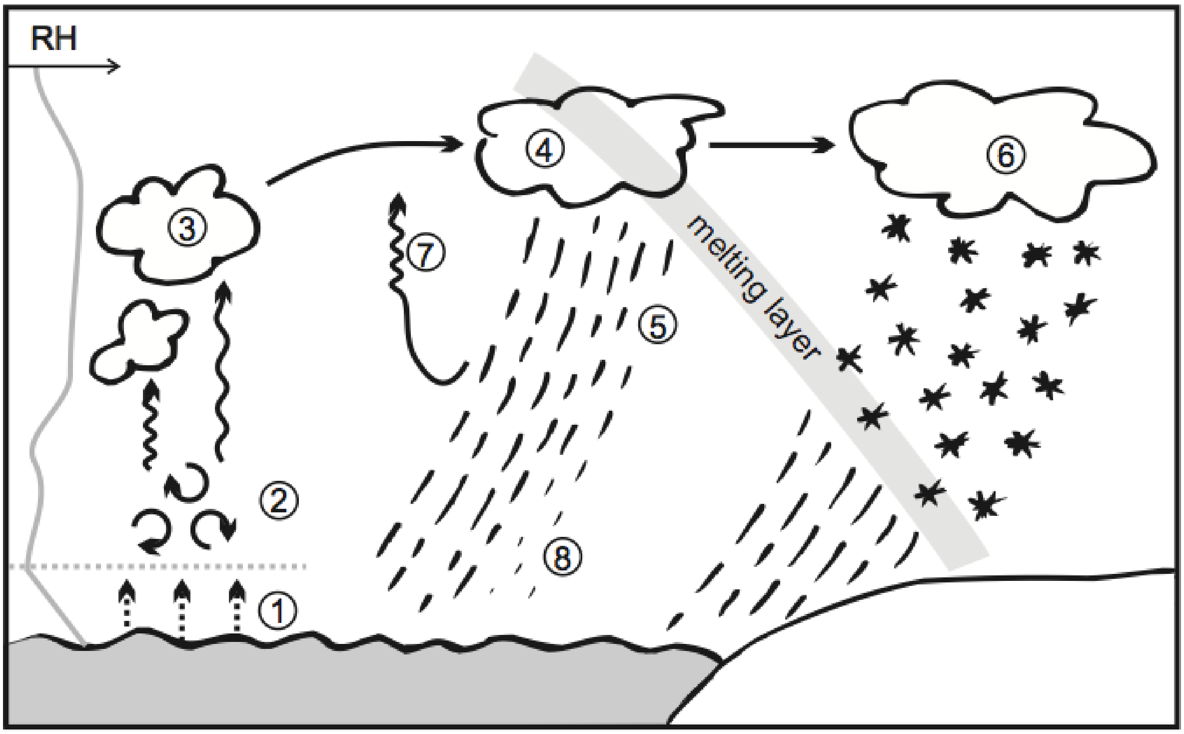

Figure 2.1: Illustration of the most relevant physical mechanism and their isotopic fractionation processes in the hydrological cycle. Adapted from Sodemann (2006).

- The evaporation of water from the ocean surface (1) is divided in both equilibrium and non-equilibrium effects. At the interface between water and air the two phases are in equilibrium, the atmospheric air will be drained for heavy isotopes with respect to the sea surface. Above the interface and below the turbulent boundary layer, a small layer is dominated by molecular diffusion, and is not in equilibrium. The total evaporation of water from the ocean surface is however assumed to occur without fractionation.
- The transport of water within the turbulent boundary layer (2) is assumed to occur without fractionation.
- Water condense (3) and form clouds, is assumed to be an equilibrium process.

- The remaining cloud water after precipitation (4) will be depleted from the heavy isotopes, since the heavy isotopes are preferable in the condensed phase, and will eventually fall as precipitation (5). This is also the case for the ice crystals (6), but with a different fractionation factor (Sodemann, 2006).
- The precipitating water (5) will be in equilibrium with the surrounding moisture. The equilibrium time will depend on the drop size and relative humidity (Sodemann, 2006). The moisture at lower level will often be less depleted than at cloud base, leading to that the precipitation reaching the surface will be enriched in heavy isotopes compared to the precipitation at the cloud base. Larger raindrops will also have higher fall velocity, given a lower exchange with the surrounding moisture (Sodemann, 2006).
- When ice crystals forms (6) an additional fractionation mechanism enters, this is however not well observed, and is only parameterized. Because of requirement of supersaturated environment for development of ice crystals, it will not be in isotopic equilibrium.
- The water is being reevaporated from the falling rain drops (7), leading to further enrichment in heavy isotopes (Gat, 1996).
- Precipitation falling through a layer containing low relative humidity (8). The precipitation will lead to an enrichment of the surrounding moisture, and lead to an enrichment of the isotopic signal at the surface.

The isotopic composition of precipitated rain will often resemble that of the surface, since the lower level is less depleted than the cloud base. Snow will however not be in equilibrium with the surrounding as it falls through the atmosphere, and shows a much more depleted signal when arriving at the surface (Sodemann, 2006). The hail stones may give information about the different levels in the atmosphere.

The melting layer is important for the altitude from transition between rain and snow, and their isotopic signals. The further down the melting layer is, the more of the signal coming from the snow will be retained.

As a consequence of this, the $\delta^{18}O$ and δD will be better at representing the condition from the precipitation formation for snow than for rain. The values obtained from the rain will resemble more of the condition near the surface (Sodemann, 2006).

Chapter 3

Method - A Lagrangian moisture source diagnostic

To diagnose the origin of moisture, a method for analyzing the water transport introduced by Sodemann *et al.* (2008), will be used. Through a back trajectory, changes in the specific humidity for an air parcel will principally tell us about the precipitation and evaporation to the air parcel, when mixing with neighboring parcels are neglected. The aim of this model is to identify the location of the moisture uptake, and estimate how much each uptake or precipitation contribution to the total moisture increase or decrease. The moisture source diagnostic look at evaporation or precipitation at temporal sequences of the air parcel, to find the moisture source region.

The moisture changes during a time interval are given as:

$$\frac{Dq}{Dt} \approx \frac{\Delta q}{\Delta t} = E - P \ \left(g \ kg^{-1} \ (6 \ h)^{-1}\right) \tag{3.1}$$

Where Δq is the moisture change, Δt is the time interval, E is evaporation and P is precipitation. In this thesis Δt is selected to be 6 h, and is dropped in the following expressions for simplicity. It is assumed that during the 6 h time interval, either evaporation or precipitation dominates, and is given by the sign of Δq (Sodemann *et al.*, 2008).

3.1 Identifying the moisture source

An illustration of the Lagrangian moisture source diagnostic is shown in Figure 3.1. It illustrates the trajectory of an air parcel from the Atlantic Ocean to Greenland. Since it is a back trajectory, the arrival point in Greenland is the starting point, while the earliest point in the Atlantic Ocean is called the end point. The trajectory of the air parcel is shown by the blue line. The thick blue lines, labeled 1 and 3, denotes moisture uptake, $\Delta q^0 > 0$. Label 2 and 4 shows moisture decrease, $\Delta q^0 < 0$.

The subscript of Δq^0 express that it is the total diagnosed moisture change at the source region (compared to the weighted value (Sodemann, 2006)). It is given by the changes in

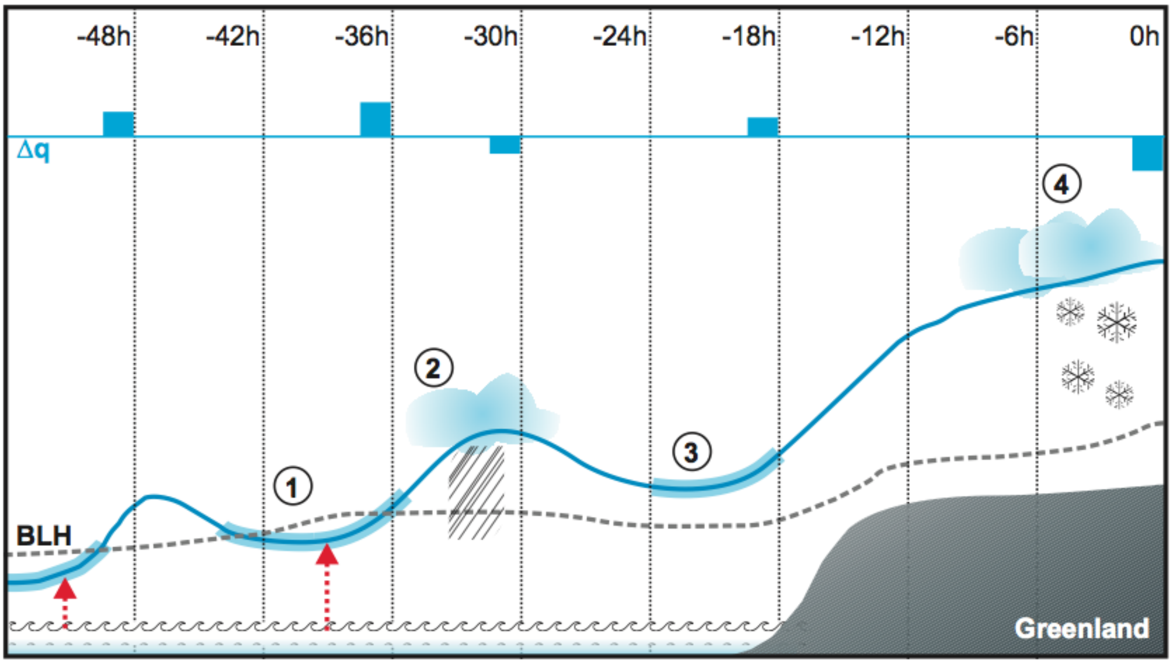

Figure 3.1: Sketch of the trajectory of an air parcel going from the Atlantic Ocean to Greenland. The blue line shows the backward trajectory from the Atlantic Ocean to Greenland. The time is shown at the top, with 6 h intervals. The straight blue line in the top panel is the change in the parcels specific humidity, Δq (g kg^{-1}). Bars above the line, $\Delta q > 0$, denotes moisture increases and bars below, $\Delta q < 0$, denotes moisture decreases during the 6 h time intervals. The thick blue sections along the trajectory also denotes moisture increase, while the red arrows denotes evaporation locations. BLH stands for boundary layer height, and is shown by the black line. Adapted from Sodemann (2006)

q, from the parcel position at time t, given by $\vec{x}(t)$, to the parcel position at time $t - 6h$, given by $\vec{x}(t - 6h)$:

$$\Delta q^0 = q(\vec{x}(t)) - q(\vec{x}(t - 6h)) \tag{3.2}$$

The model has two different starting conditions, the first being that only parcels that precipitate at the starting point of the trajectory is traced backwards in time, and the second being that all the water vapour at the starting point is being traced backwards. For tracing precipitation, a relative threshold is chosen to be 80%, which is in agreement with the ECMWF model (Sodemann *et al.*, 2008). Whenever the threshold is exceeded it is assumed that clouds exist and precipitation falls.

To derive an expression for the precipitation or water vapour at the surface, the target area is discretized both horizontally and vertically into a large number of parcels. Sodemann *et al.* (2008) choose two simplifying assumption, the first being that when $\Delta q^0 < 0$ all the moisture decrease is due to precipitation. The second being that all the precipitation falls immediately. The precipitation at the surface, P_{sfc}, is therefore derived from the decrease in moisture over a column of air parcels, as expressed in:

$$P_{surface} = -\frac{1}{g}\sum_{k=1}^{k_{top}} \Delta q_k^0(t=0)\cdot 10^{-3}\cdot \Delta p_k \qquad (mm\ 6h^{-1}) \tag{3.3}$$

where g is the gravity, k is the vertical index from the starting point in the trajectory, $\Delta q_k^0(t=0)$ is the precipitation at the starting point (in g kg^{-1}) and Δp is the change in pressure (in hPa).

The water vapour at the surface, WV_{sfc} is expressed as:

$$WV_{surface} = -\frac{1}{g}\sum_{k=1}^{k_{top}} q_k^0(t=0)\cdot 10^{-3}\cdot \Delta p_k \qquad (mm\ 6h^{-1}) \tag{3.4}$$

where $q_k^0(t=0)$ is the water vapour at the starting point (in g kg^{-1}).

An estimate for the precipitation or water vapour is calculated for the start point in the trajectory from equation 3.3 or 3.4. The air parcels are then traced backwards until Δq^0 is larger than the threshold for moisture uptake.

The uptake of moisture to the air parcels is divided into uptake above or under the height of the boundary layer. Under the boundary layer it is assumed that the moisture is exchanged between the air parcels and the surrounding air, because of the turbulent fluxes (Sodemann *et al.*, 2008). A moisture uptake under the boundary layer will therefore give a moisture uptake point at this location. A moisture uptake above the boundary layer could not be assessed to an evaporation source at the surface, and it is assumed that other physical or numerical processes will produce the moisture increase. Factors that can contribute to a moisture increase above the boundary layer are convection, evaporation of precipitating hydrometeors, subgrid-scale turbulent fluxes, numerical diffusion, physical inconsistencies from the ECMWF time steps or numerical errors related to the trajectory (Sodemann *et al.*, 2008).

To check if the moisture increase is within the BL, meaning, if the parcels altitude is under the boundary layer height from the ECMWF model, the following equation is used:

$$1.5\cdot BLH \geq 8000\cdot ln(\frac{4000}{p}) \qquad (m) \tag{3.5}$$

The factor 1.5 on the left side is used so that the moisture uptake at the top of the boundary layer is considered to originate from the location. It was used so that even the small-scale variability should be considered, which is especially sensitive over the marine boundary layer. The expression on the right convert a standard atmosphere of an air parcel with pressure p to an altitude (Sodemann *et al.*, 2008).

A moisture uptake locations is identified at the time interval (t - 6, t), if equation 3.5 if fulfilled, and Δq^0 and other meteorological parameters is stored. If however the moisture uptake is above the defined boundary layer height, only the location and the amount of the moisture increase is stored.

The trajectory is calculated backward until either the trajectory reach $q \leq 0.05$ g kg^{-1}, meaning that all the moisture has rained out, or until it reach the end point of the trajectory.

3.2 Assumptions and limitations of the Lagrangian diagnostic

The Lagrangian moisture source diagnostic contains both assumptions and limitations. Some are listed below.

- A considerable simplification in the precipitation estimate is the neglecting of microphysical processes, and that a decrease in specific humidity will immediately lead to surface precipitation. This assumption are quite different from the precipitation parameterizations in the ECMWF model, and may lead to a positive bias in areas with high precipitation (Sodemann *et al.*, 2008).
- Another simplification which may lead to a displacement of the estimated precipitation is from the value of the precipitation estimate at the arriving location. The precipitation estimate at the arriving location is assumed to be given from the value of Δq^0 for the last 6 hours before the arriving location, instead of being distribution over the whole area crossed by the parcel.
- The moisture uptake is sensitive to the parameter choices, especially the uptakes for threshold and precipitation.The thresholds must be low enough for it to identify the dominant moisture source but also high enough to exclude the noise in the moisture uptake.
- Trajectory calculations beyond 10 days can lead to inconstancy in the air masses, from errors in the wind field (Stohl and Seibert, 1998).
- Several moisture transport processes have been neglected in the Lagrangian diagnostic, including turbulence, numerical diffusion, moisture change from convection and the evaporation of rainwater (Sodemann *et al.*, 2008).
- The Lagrangian moisture source diagnostic could contain analysis errors, from uncertainties in the observations or in the data assimilation.

3.3 The settings chosen in the Lagrangian moisture source diagnostic

The Lagrangian moisture source diagnostic is chosen to run on a target area of 5^o x 1^o around the location of the observations and the gridding box is chosen to be 10^o x 5^o

around the same location. A greater longitude was chosen because of the location being far north. The grid are 0.5 x 0.5.

The thresholds for uptake and precipitation are chosen to be 0.1. The minimum precipitation threshold is chosen to be -0.1, while for water vapour the minimum threshold is set to be a positive number, to make sure everything is included.

The maximum altitude is chosen to be 2500 km for Tustervatn and 3500 km for NEEM, because of its higher location.

Chapter 4

The study sites

4.1 NEEM

NEEM (North Greenland Eemian Drilling Project) in Greenland (77.45°N, 51.05°W, 2484m a.s.l.) had from 2007 to 2012 been used as a site for an international deep drilling program. The measurements have provided information about the climatology and glaciology since the last interglacial period. In this thesis the data from the summer field campaign from 2010, 2011 and 2012 introduced by Steen-Larsen *et al.* (2013; 2014) is further investigated. The data from the summer field campaign is further presented in section 4.1.1.

In 2006 an automatic weather station was stationed at NEEM for meteorological observations. It measured air temperature and relative humidity using a Campbell Scientific HMP45C, wind direction and speed was measured using an RM Young propellertype vane and the pressure was measured using Vaisala PTB101B. Two laser instrument, Picarro CRDS and LGR analyzers, was used to measure the composition of $H_2^{16}O$, HDO and $H_2^{18}O$. This is being further introduced in section 4.1.2, together with the field setup.

4.1.1 NEEM data

The summer field campaign, conducted by Steen-Larsen *et al.* (2013; 2014), was active from 24 May to 4 August 2010, 4 July to 4 August 2011, and 20 May to 4 August 2012. 4 August was the date of the closure of the summer camp each year. The 2010, 2011 and 2012 observations of temperature, humidity, wind direction and speed, δD and d-excess are displayed in Figure 4.1, 4.2, and 4.3. The measurements were done every 6 hours.

4.1.2 Laser instrument and field setup

The compositions of $H_2^{16}O$, HDO and $H_2^{18}O$, which gives the d-excess, are given by two laser instruments. In this field campaign a Picarro CRDS (cavity ring down spectroscopy) analyzer and an LGR analyzer (LGR inc. ICOS - integrated cavity output spectroscopy) were used. The Picarro CRDR analyzer measured samples at a 1.5 m tower, while the LGR analyzer measured samples on a 13.5 m tower.

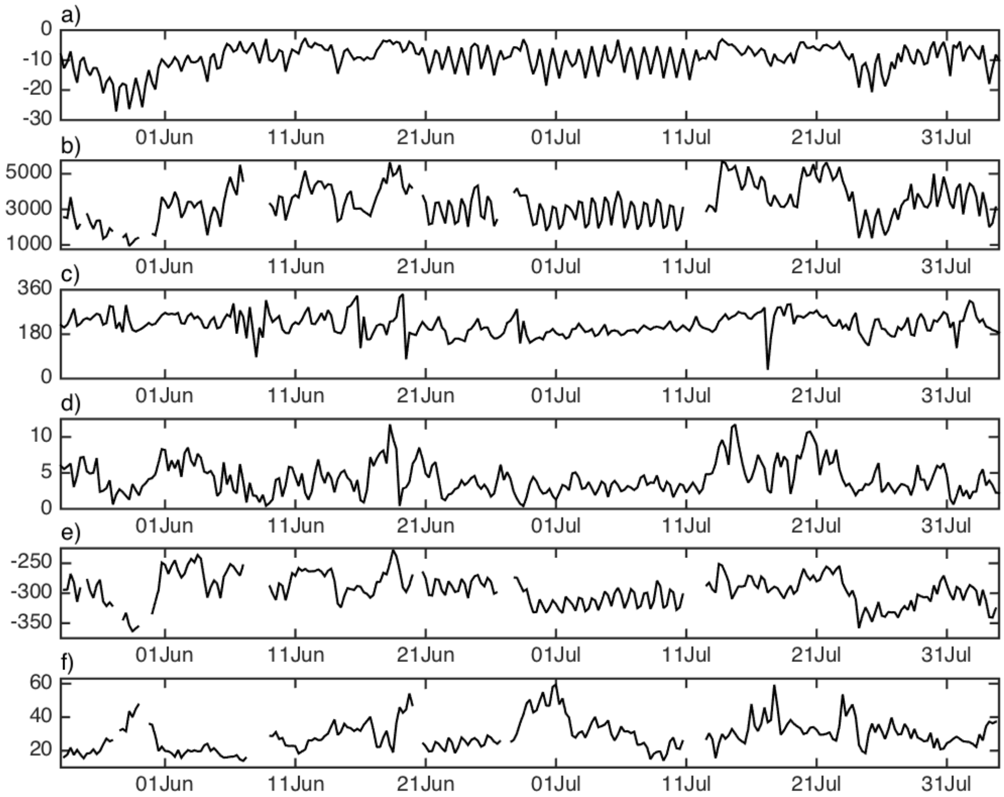

Figure 4.1: Measurements from the summer field campaign in 2010, from 24 May to 4 August. (a) Temperature [°C]. (b) Humidity [ppmv]. (c) Wind direction [°]. (d) Wind speed [m s^{-1}]. (e) δD [‰]. (f) D-excess [‰].

Both the Picarro CRDR analyzer and the LGR analyzer used a cavity technique, with near infrared laser absorption spectroscopy (CEAS). Cavity ring down spectroscopy (CRDS) as used by Picarro, sends radiation with different wavelength into the cavity, based on the absorption wavelength for the molecules. $H_2^{16}O$, HDO and $H_2^{18}O$ absorbs different wavelengths, and the measurements of the reflected radiation from the cavity indicates the composition. CRDS uses a time-based measurement of the decay of the radiation back from the cavity. The LGR analyzer used an integrated cavity output spectroscopy (ICOS), and is based on the radiation that is transmitted through the cavity, by using different wavelengths and comparing the intensity on both sites. ICOS used a ring down measurement to verify the absorption of the baseline (Steen-Larsen *et al.*, 2013). To calculate the concentration, Beer-Lambert law was applied by both analyzers (Steen-Larsen *et al.*, 2013).

Both of the analyzers were placed inside a tent, about 50 m from the NEEM camp. The setup for the two analyzers are shown in Figure 4.4. In 2011 and 2012 both the

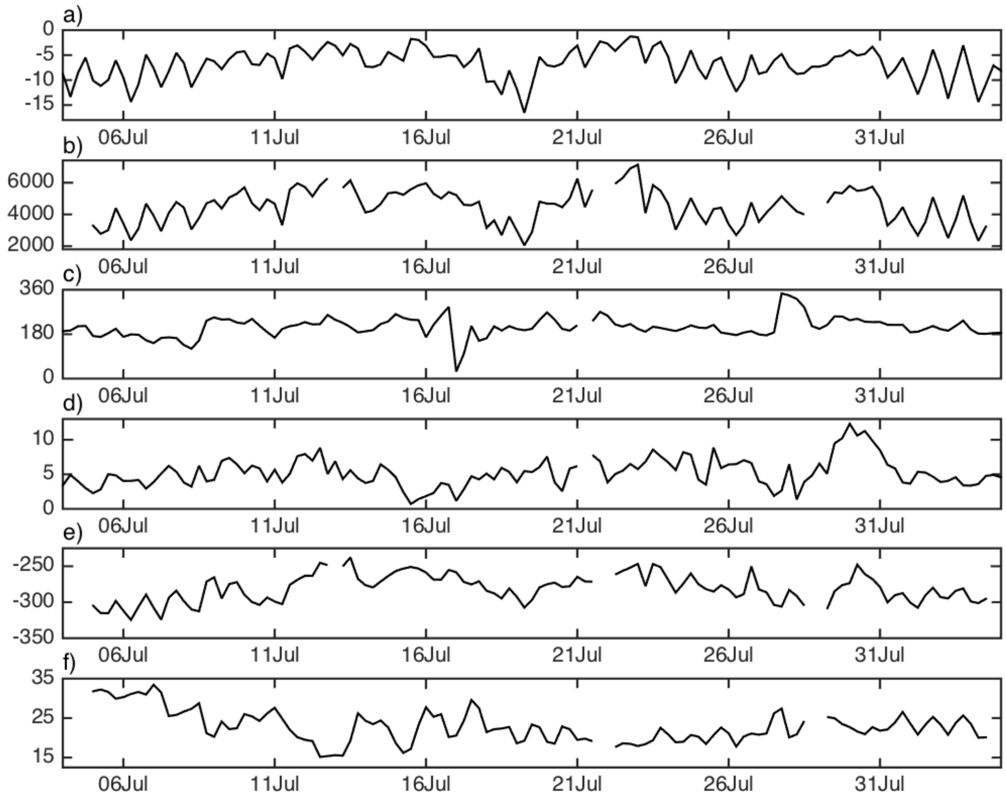

Figure 4.2: Measurements from the summer field campaign in 2011, from 4 July to 4 August. (a) Temperature [°C]. (b) Humidity [ppmv]. (c) Wind direction [°]. (d) Wind speed [m s^{-1}]. (e) δD [‰]. (f) D-excess [‰].

analyzers were placed inside a temperature-regulated box, controlling the temperature to within ± 0.2°C. Without the temperature regulator the temperature fluctuation inside the tent would be up to 20°C during a day (Steen-Larsen *et al.*, 2013), because of the local weather. In 2010 the LGR analyzers were placed inside an active temperature-regulated box, controlling the temperature to within ± 0.2°C. The Picarro analyzers were placed inside a passive temperature-regulated box, which was not as sufficient as the active temperature-regulated box.

The accuracy of the instrument used to measure the air temperature, relative humidity, wind direction and speed, and the station pressure is shown in Table 4.1.

Further details of the field setup can be read in Steen-Larsen *et al.* (2013).

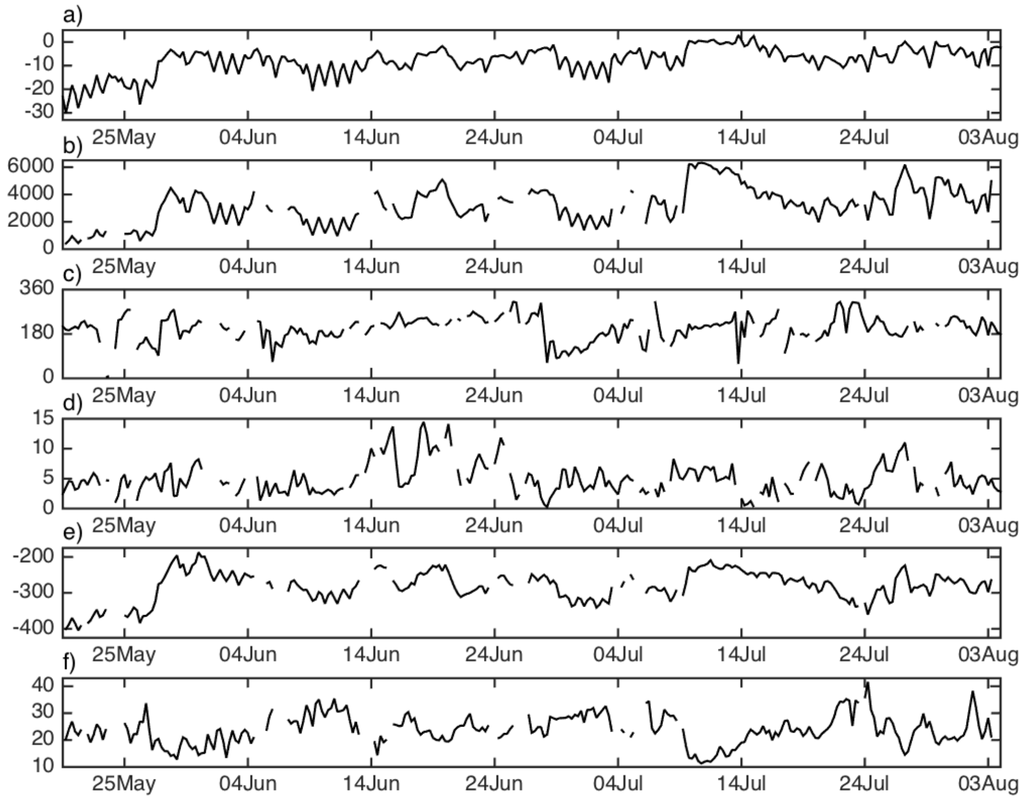

Figure 4.3: Measurements from the summer field campaign in 2012, from 20 May to 4 August. (a) Temperature [°C]. (b) Humidity [ppmv]. (c) Wind direction [°]. (d) Wind speed [m s^{-1}]. (e) δD [‰]. (f) D-excess [‰].

4.1.3 Climate at NEEM

The average summer (JJA) temperature for the years from 2006 to 2011 is estimated to be $\sim -11 \pm 5$°C (Steen-Larsen *et al.*, 2013). The annual average accumulation rate for the years from 1964 to 2005 is estimated to be 20 $cm\ a^{-1}$, with the largest contribution occurring in the summer months (Steen-Larsen *et al.*, 2011).

A seasonality chart of temperature, humidity, d-excess and δD for the measurements from NEEM are displayed in Figure 4.5.

The temperature had a clear increase from May (-15.2 ± 6.6°C) to June (-8.3 ± 3.5°C). The summer temperature was more stable, reaching its highest average value in July (-7.0 ± 4.0°C). The humidity had also a clear increase from May (2067 ± 1175 ppmv) to its highest value in July (3945 ± 1234 ppmv). D-excess showed a smaller increase from May (23.0 ± 7.5‰) to June (26.5 ± 7.9‰) and δD showed an increase from May (-309.4 ± 60.2‰) to June (-278.3 ± 25.8‰).

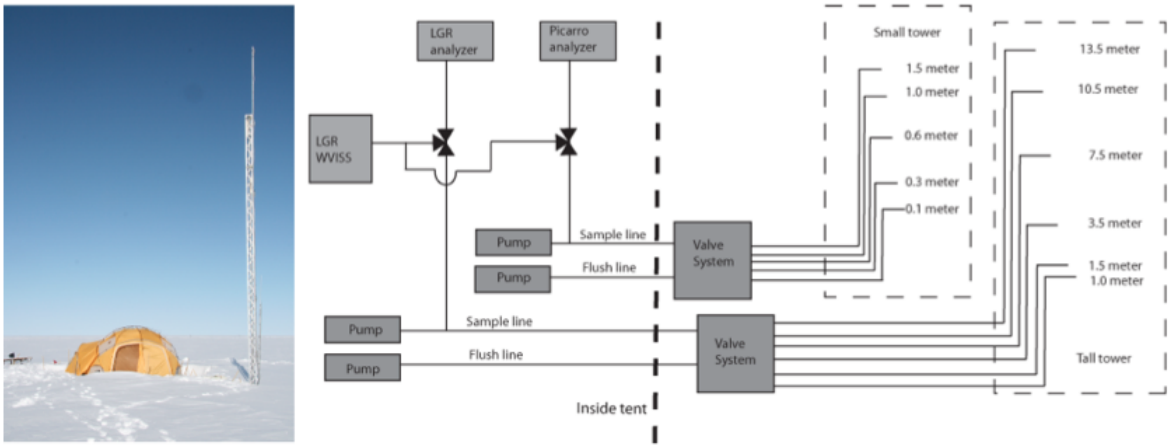

Figure 4.4: An illustration of the setup for the two laster instruments introduced in the text. Adapted from Steen-Larsen *et al.* (2013).

Table 4.1: Instrument performance. From Steen-Larsen *et al.* (2013)

Instrument	Measurements	Performance
Campbell Sci. HMP45C	Air temperature	± 0.1°C
	Relative humidity	± 5%, < 90%
		± 10%, > 90%
R.M. Young propeller-type vane	Wind direction	± 5°
	Windspeed	± 0.1 m s^{-1}
Vaisala PTB101B	Pressure	± 0.1 mb

δD was highly correlated with temperature (R^2 = 0.60) and humidity (R^2 = 0.53). D-excess had its highest correlation with δD (R^2 = 0.21), while the correlation with temperature (R^2 = 0.04) and humidity (R^2 = 0.05) was poor.

The wind direction and speed was more arbitrary. The direction had its biggest contribution from the south, with a span from east to west. The wind speed seemed to have a small increase in the spread of the measurements in the late summer.

4.2 Tustervatn

In Tustervatn (65.83°N, 13.92°E, 439m a.s.l.) in Norway, precipitation samples have been collected since 1973. The samples were measured daily at 07.00h local time. Here we will look closer into the measurements of the daily precipitation $\delta^{18}O$ values from 10 September 1997 to 12 October 2004, introduced by Theakstone (2008; 2011). Analyzes of the oxygen isotopes were made whenever the daily precipitation exceeded 2 mm.

The isotopic samples were sealed in a vial to prevent from evaporation, before taken to

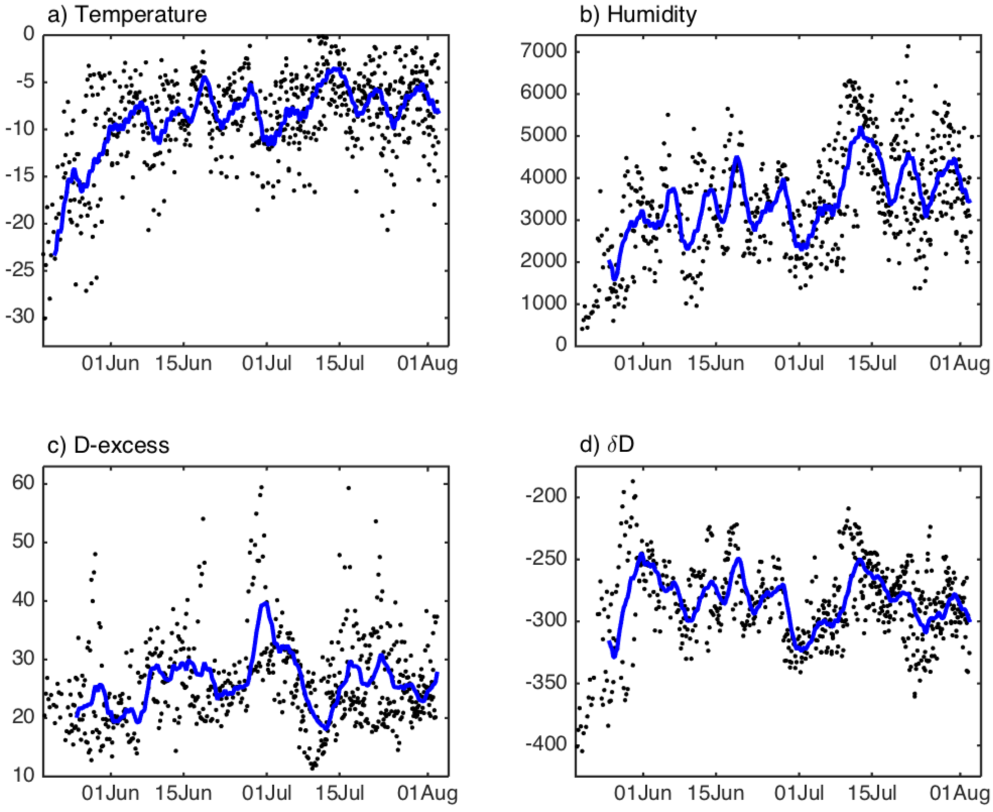

Figure 4.5: Seasonality charts of the temperature [°C], humidity [ppmv], d-excess [‰] and δD [‰] measurements from NEEM. The dots indicate the measurements done every 6 hours. The blue line shows the running mean.

Copenhagen University's Niels Bohr Institute for analysis. At the Copenhagen University they were analyzed using a mass spectrometer, with an accuracy of ± 0.08‰.

During the 7 years 930 samples were collected of the isotopes, accounting for 91.8% of the total precipitation (Theakstone, 2011).

4.2.1 Tustervatn data

The measurements from 10 September 1997 to 12 October 2004, conducted by Theakstone (2008; 2011), are displayed in Figure 4.6. Since the measurements only were conducted when the precipitation exceeded 2 mm there are only few continuous periods.

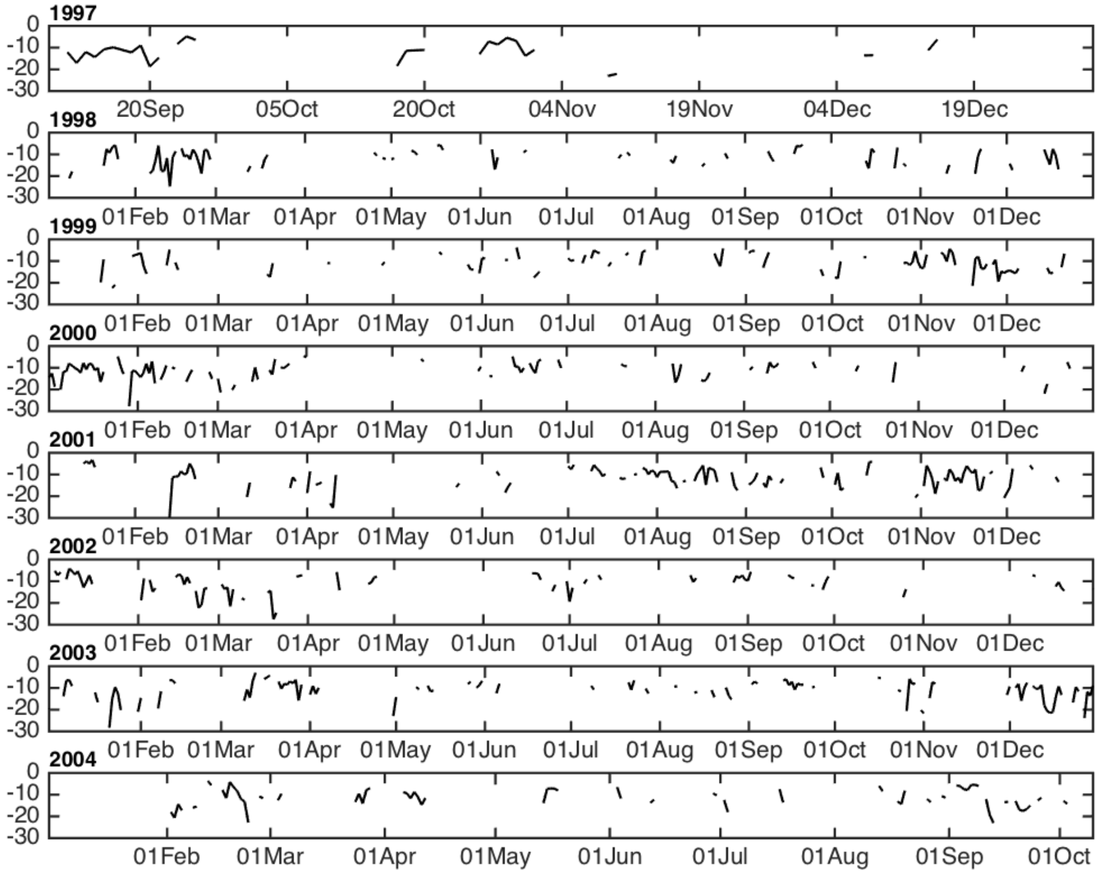

Figure 4.6: Measurements of $\delta^{18}O$ [‰] at Tustervatn from 10 September 1997 to 12 October 2004.

4.2.2 Climate at Tustervatn

A seasonality chart for the measurements at Tustervatn are shown in Figure 4.7, showing a small increase in $\delta^{18}O$ for the summer months. $\delta^{18}O$ had a yearly average of -11.7 ± 4.6‰. The minimum $\delta^{18}O$ value occurred in the winter months (DJF; -12.5 ± 5.4‰), and the highest in the summer months (JJA; -10.5 ± 3.1‰). The variability was higher in the winter, with a span from ~ -30 to -3‰. The summer had a span from ~ -20 to -4‰.

The measurements from 1997 to 2004 were showing a small linear trend equal to 0.0003‰ per year (Theakstone, 2011), which could suggest a warming trend during the period.

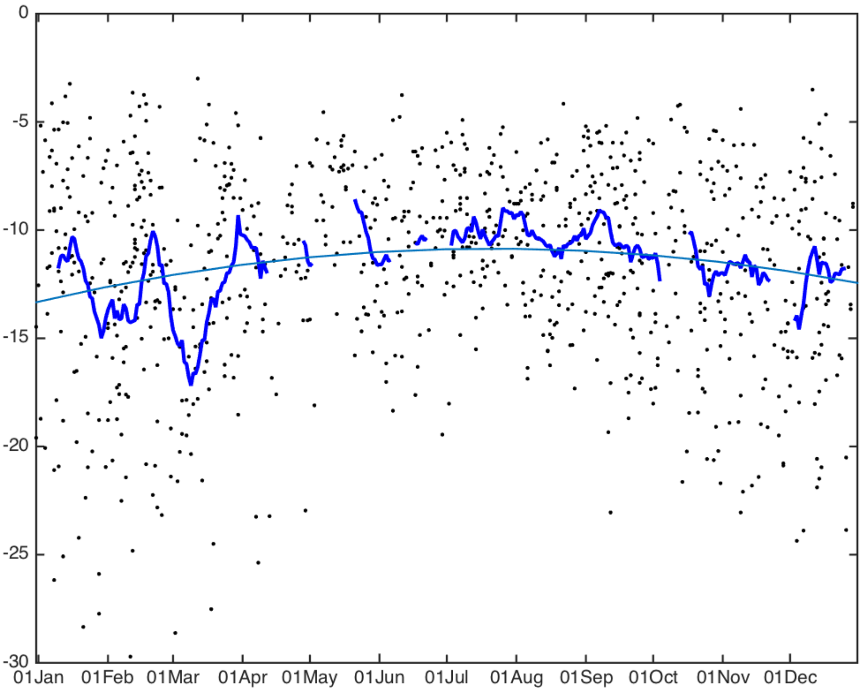

Figure 4.7: Seasonality charts of $\delta^{18}O$ [‰] from Tustervatn. The dots indicate the daily measurements. The thin blue line shows the linear trend and the thick blue line shows the running mean.

Chapter 5

Results

To identify the origin of moisture to the Arctic, the Lagrangian moisture source diagnostic have been run for NEEM and Tustervatn. The moisture source and annual trends are investigated in section 5.1. The comparison with the measurement is introduced in section 5.2. Because of the poor sampling at Tustervatn, and the fact that variations in δ^{18}O and δD are primarily driven by air mass distillation and the equilibrium fractionation, while d-excess preserve the information from the evaporation location, the NEEM data is emphasized. Three case studies were selected from the measurements from NEEM, and are introduced in section 5.3.

For the moisture source the Lagrangian moisture source diagnostic have been used to trace the vapour at the starting position. In section 5.2.2 the Lagrangian moisture source diagnostic have been used to trace the precipitation at Tustervatn, corresponding with the measurements taken from the precipitated water.

5.1 Moisture source and annual trends

5.1.1 NEEM

The Lagrangian moisture source diagnostic have been run for NEEM, in the time period from 2010 to 2012. The moisture uptake for each month in 2012 is illustrated in Figure 5.1. The data from 2010 and 2011 are shown in Appendix A.1. The moisture uptake showed a clear change in the uptake throughout the year. The biggest moisture uptake took place in the summer, (JJA; average of 970 mm/month), while the minimum uptake occured in the winter (DJF; average of 130 mm/month). The yearly average was 410 mm/month.

The winter months (DJF) were characterized by the smallest uptake, with a minimum uptake in February (110 mm). The winter uptakes were primarily located over ocean, and had contribution from the Norwegian Sea and the North Atlantic Ocean. The months from March (160 mm) to May (380 mm) showed an increase in the moisture uptake and extension. The spring also showed an increase in the moisture uptake from higher latitudes and from the west. This was a clear shift from the winter months, the exact time of the

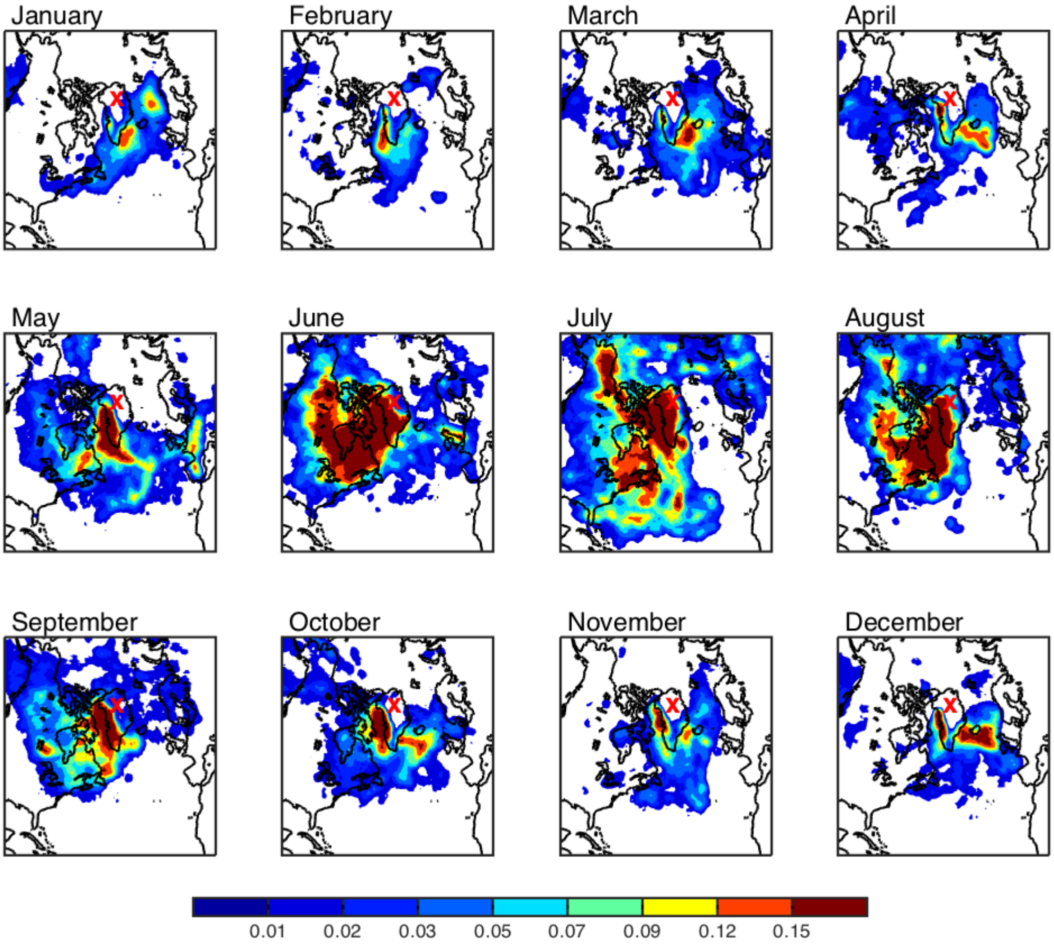

Figure 5.1: The moisture source for water vapour at NEEM identified with a 20-days back trajectory for 2012, showing the location of the moisture uptake (in mm/month) for each month. The red cross shows the location of NEEM (77.45°N, 51.05°W).

shift was different for the three years investigated. From March to May we saw an increase in the moisture taken up over land, from Greenland and the north of Canada. The summer months exhibited a clear increase in the moisture uptake, especially from an increased area of high moisture uptake. The extension of the moisture uptake was also clearly increased. The highest uptake took place in July (1140 mm). June, July and August showed higher uptakes from the west of Greenland, Baffin Bay, David Strait and smaller contributions from the north of Canada and the North Atlantic Ocean. From September (460 mm) the amount and extension of the moisture uptake started to decrease, before reaching its lowest value in the winter months. The months from September to November showed a decrease in the moisture from higher latitudes and the west of NEEM, going towards a bigger contribution from the east of NEEM in the winter months.

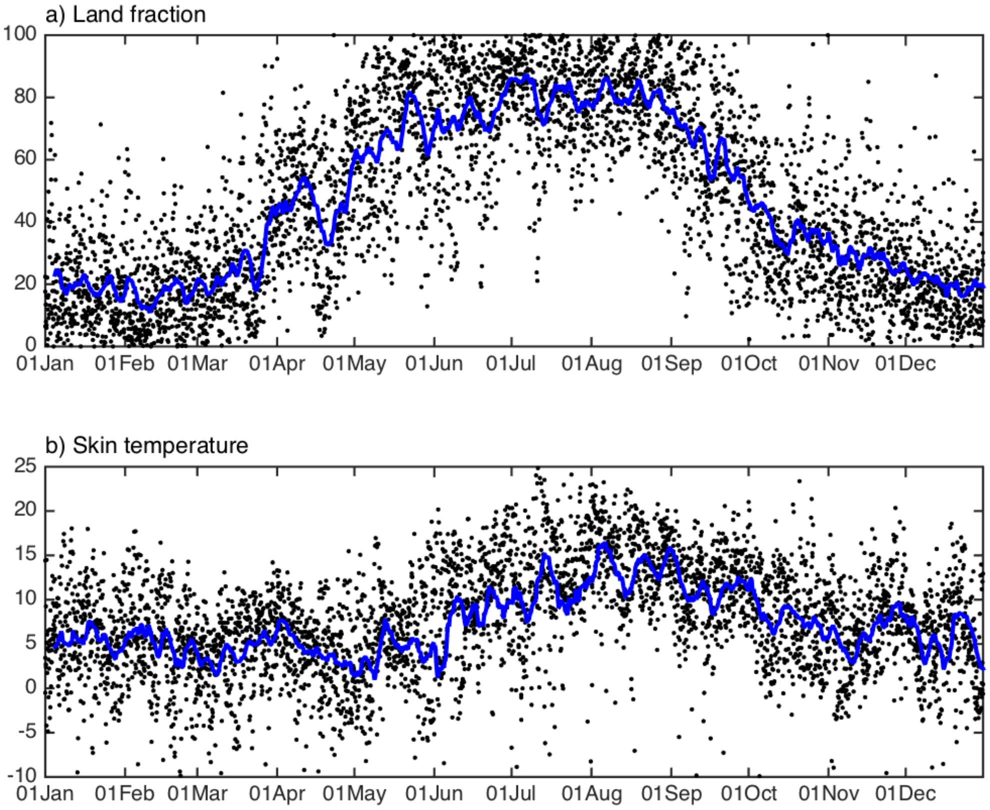

Figure 5.2: Time series of the moisture source properties for the years from 2010 to 2012. (a) Land fraction [%] of the moisture uptake. (b) Skin temperature [°C] at the location of the moisture uptake. The black dots indicate an average of the moisture reaching NEEM every 6 hours. The blue line indicate the running mean.

The diagnosed land fraction is shown in Figure 5.2a. Land fraction shows the amount of moisture taken up over land. The land fraction for NEEM exhibited a clear seasonal cycle. For the winter months the uptake was primarily from the ocean, while the summer months had its prime uptake from land. The land fraction increased markedly from 19 ± 13% in the winter to 79 ± 15% in the summer. The land fraction showed a clear increase from March (27 ± 18%) to May (68 ± 20%) and a clear decrease from September (61 ± 20%) to November (28 ± 15%).

The skin temperature is shown in Figure 5.2b, showing an average of the skin temperature at the evaporating locations. The skin temperature also exhibited a seasonal cycle, with an increase in the summer. The months from December to May had a rather stable source temperature, with an average of 4.7 ± 5.7°C. The period corresponded well in time with the main uptake coming from the ocean, which is assumed to give a stable skin temperature. The skin temperature increased from June (8.9 ± 8.4°C), before reaching

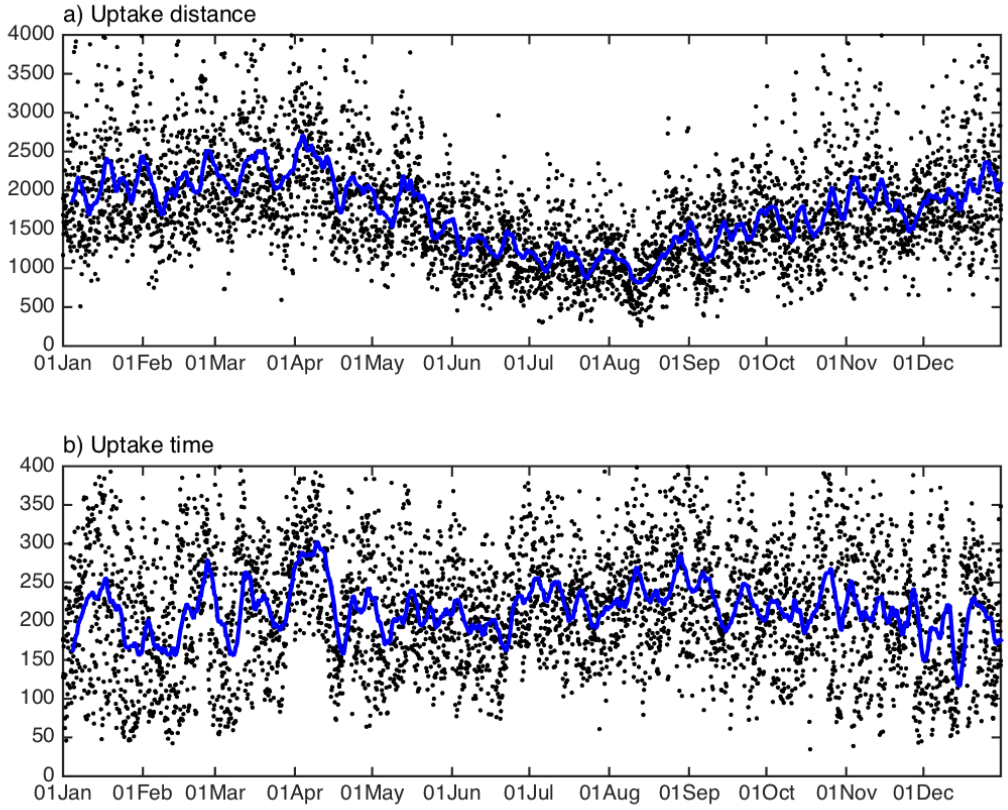

Figure 5.3: Time series of the moisture source properties for the years from 2010 to 2012. (a) Uptake distance [km] for the moisture uptake. (b) Uptake time [h] for the moisture uptake. The black dots indicate an average of the moisture reaching NEEM every 6 hours. The blue line indicate the running mean.

its highest value in August (14.0 ± 5.8°C). From September (11.0 ± 8.9°C) to November (6.5 ± 5.8°C) the skin temperature gently decreased. The gentle decrease was likely from the moisture uptake going from land towards oceans. The oceans will have a bigger heat capacity, and give a more gentle temperature decrease.

The uptake distance is shown in Figure 5.3a. The uptake distance is the distance from the evaporating location to NEEM. The uptake distance also exhibited a clear seasonal cycle, with longer distances in the winter and spring, and shorter in the summer. The maximum value was reached in March and April (2220 ± 680 km), and the minimum value was reached in July (1120 ± 360 km). The variability was however much higher in the winter, with values between 500 to 4500 km (primarily from 1000 to 4000 km). The summer values had a more narrow span with values between 300 to 3000 km (primarily from 500 to 2000 km). The decrease in the uptake distance was consistent in time with the increase in the land fraction, which was also consistent with the great uptake from

a) Source longitude

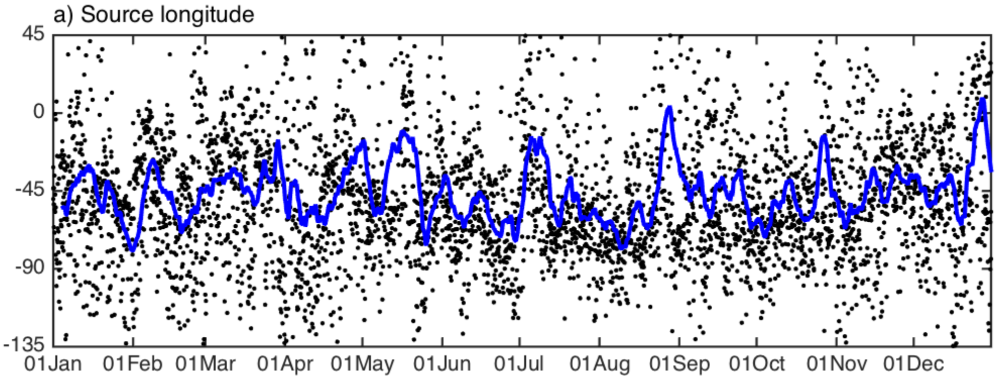

b) Source latitude

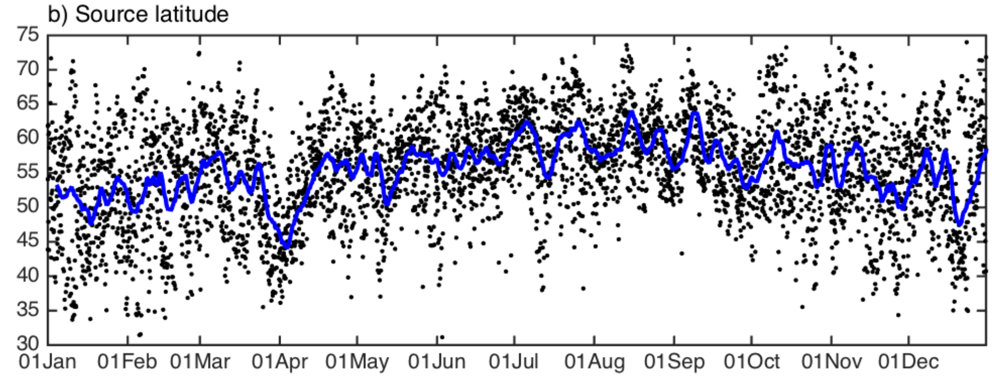

Figure 5.4: Time series of the moisture source properties for the years from 2010 to 2012. (a) Source longitude [°] of the moisture uptake. (b) Source latitude [°] of the moisture uptake. The black dots indicate an average of the moisture reaching NEEM every 6 hours. The blue line indicate the running mean.

Greenland in Figure 5.1.

The uptake time is shown in Figure 5.3b. The uptake time is the time from the vapour evaporated until it reaches NEEM. The uptake time showed no clear trends or seasonal cycle. The smallest uptake time was however located in the winter months (DJF; 200 ± 85 h), and the biggest uptake time in April (240 ± 75 h) and in the late summer, July, August and September (230 ± 65 h). The uptake time had a span from 35 to 435 hours, and showed large variability. The variability was slightly smaller in the summer. The highest uptake time being in the summer and the shortest in the winter, is opposite of what would be excepted from the uptake distance. This means that the local moisture uptake in the summer must stay longer in the atmosphere.

The source longitude is shown in Figure 5.4a, showing the average longitude of the evaporation location. The source longitude had an average of 45 ± 45°W, meaning that it was primarily from areas around NEEM (51.05°W). The source longitude showed no seasonal cycle. March (40 ± 119°W), May (39 ± 132°W) and December (36 ± 156°W) showed the months with the biggest contribution from the east, while the biggest contribution from the west was January (52 ± 112°W) and June (59 ± 118°W). The source longitude had however a wide span from 150°E to 150°W, with its biggest contribution from 35 to 90°W.

July and August seemed to have a clear contribution from 60 to 90°W, which was consistent with more uptake west of NEEM, seen in Figure 5.1. The reason for its higher average value may be due to the higher variability for the contribution from the east of NEEM. This could also be the case for December, January and February with a clear contribution from around 30 to 50°W of NEEM, but with more variability in the west. This is also consistent with the uptake from the Norwegian Sea shown in Figure 5.1.

The source latitude is shown in Figure 5.4b, showing the average latitude of the evaporation location. The source latitude showed a seasonal cycle, with an increase of $\sim$ 10° from winter to summer. The moisture source closest to NEEM (77.45°N) was located in July and August (59 ± 6°N). The winter months, from December to April had large contributions from the south (53 ± 8°N). The lowest average source latitude was found in January (52 ± 8°N). From May and June the source latitude was increasing, while September and October showed a decrease. The increased source latitude in the summer corresponded well with the decrease in the uptake distance.

The source latitude had a span from $\sim$ 30 to 75°N, with the biggest variance in the winter months. The winter months had the biggest contribution from $\sim$ 40 to 65°N, while the summer had the biggest contribution from $\sim$ 55 to 65°N.

The moisture source in April showed a clear anomaly in the source properties for all three years. The land fraction showed a clear increase, skin temperature was increasing, uptake distance and time were increasing, source longitude was decreasing and the source latitude showed a clear decrease. The clear change in April was however not as easily visible in Figure 5.1. The reason behind the changes could be due to changes in the radiation from the winter, primarily starting in March and April (van den Broeke *et al.*, 2011). An increase in the short wave radiation from the winter conditions may have lead to sublimation from the snow surface. From the moisture source (Figure 5.1, A.1 and A.2), the uptake over Greenland seemed to increase from the winter conditions. The figures also show an increase in the uptake over the north of Canada, corresponding with a clear decrease in the source latitude.

5.1.2 Tustervatn

The Lagrangian moisture source diagnostic have been run for Tustervatn for the years from 1997 to 2004, corresponding with the measurements from Theakstone (2008; 2011). The moisture uptake for each month in 2001 is illustrated in Figure 5.5. The figures from 1997, 1999 and 2003 are shown in Appendix A.2.

Tustervatn contains a high moisture uptake and extension throughout the year, with an average of 2830 mm/month. The highest moisture uptake occured in the summer (JJA; 4710 mm/month), while the minimum uptake occured in the winter (DJF; 1360

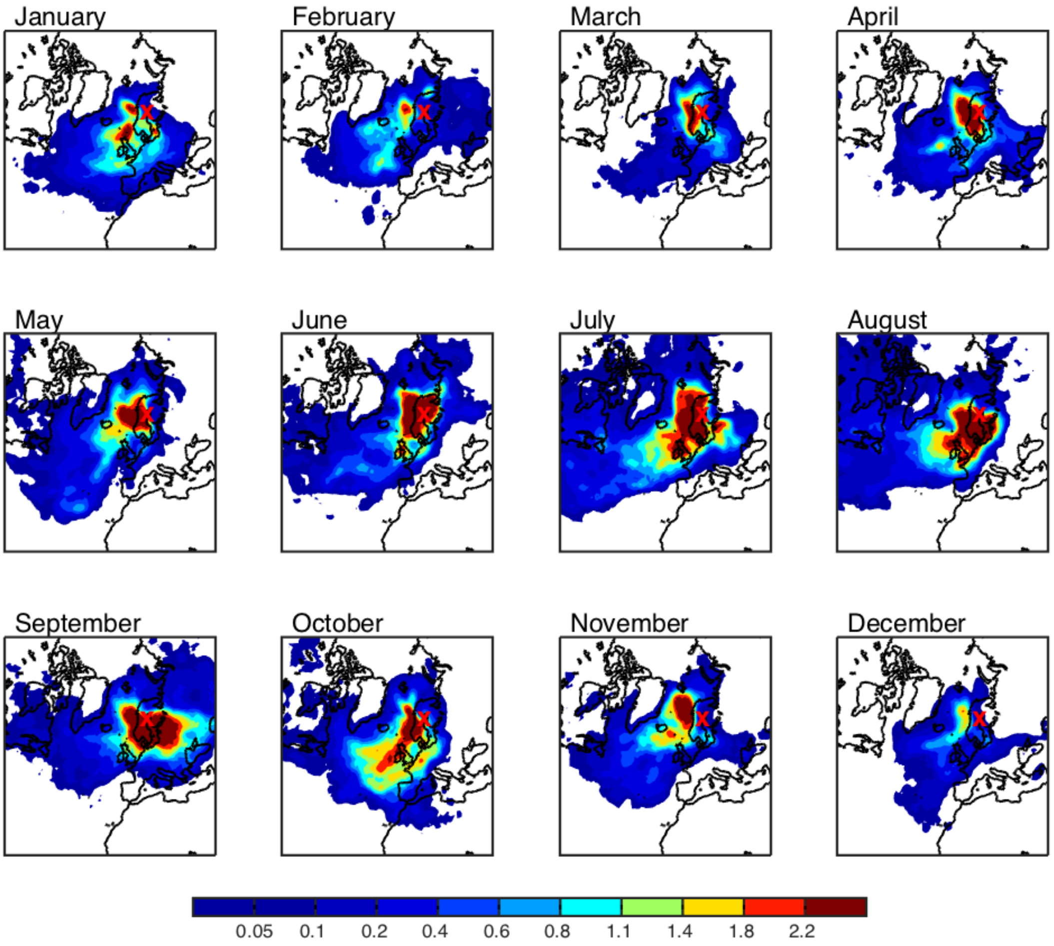

Figure 5.5: The moisture source for water vapour at Tustervatn identified with a 20-days back trajectory for 2001, showing the location of the moisture uptake (in mm/month) for each month. The red cross shows the location of Tustervatn (65.83°N, 13.92°E).

mm/month).

The winter months (DJF) got most of their uptake from the ocean. The greatest uptake was located outside the coast of Norway in the Norwegian Sea, but it also contained a clear contribution from the North Atlantic Ocean. From February (1410 mm) to May (2950 mm) we saw a markedly increase in the moisture uptake and extension. The area with high moisture uptake was also increased. The spring showed an increase in the uptake from land, with higher uptake from the south of Norway. The uptake from the North Atlantic Ocean was also increased in length. The spring showed a shift in uptake from higher latitudes, which also was the case for NEEM.

The summer months (JJA) exhibited an even higher moisture uptake, both in amount and extension. The highest moisture uptake took place in July (5180 mm). The area

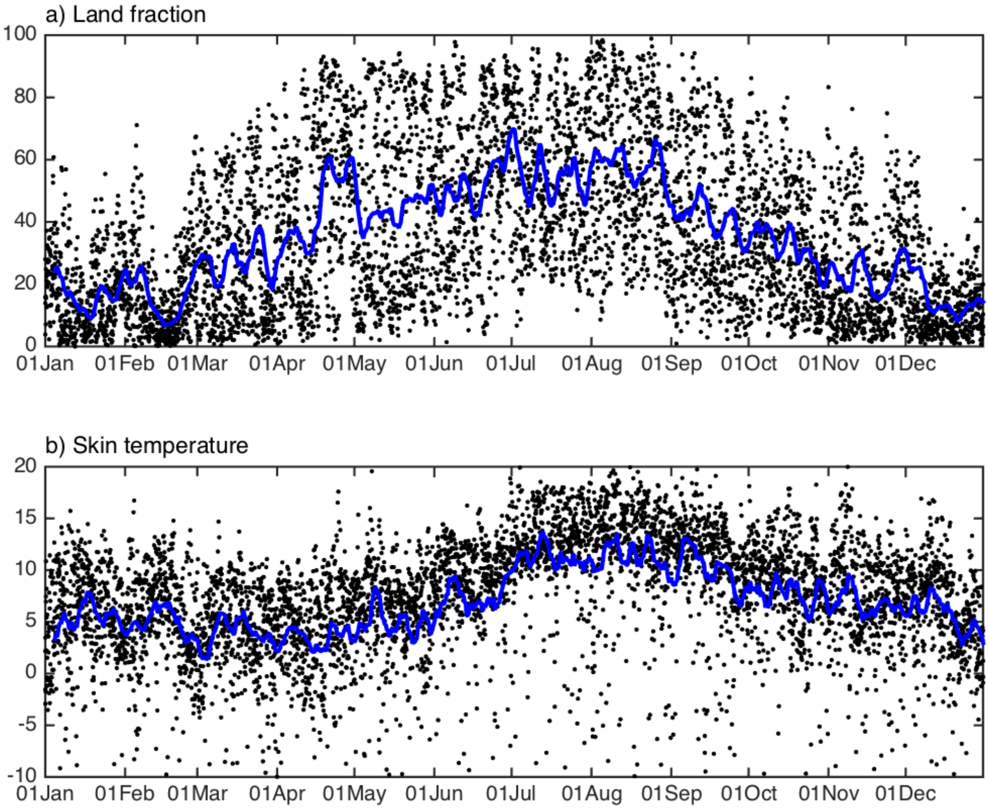

Figure 5.6: Time series of the moisture source properties for Tustervatn, for the years from 2001 to 2004. (a) Land fraction [%] of the moisture uptake. (b) Skin temperature [°C] at the location of the moisture uptake. The black dots indicate an average of the moisture reaching Tustervatn every 6 hours. The blue line indicate the running mean.

with the high moisture uptake also increased in size. The summer months exhibited a high moisture uptake over Norway, the Norwegian Sea and the North Atlantic Ocean, southwest of Norway. From September (3850 mm) we saw a decrease in the uptake and extension, until the smallest uptake was reached in December (930 mm). The autumn showed a shift away from the higher uptake over land and the contribution from higher latitudes.

The high uptake to Tustervatn from the North Atlantic Ocean, seemed to be located at the remains of the Gulf Stream. The Gulf Stream carries warm equatorial surface water to the North Atlantic. Warmer ocean surface could cause an increase in the evaporation.

The land fraction is shown in Figure 5.6a. The land fraction showed a clear seasonal cycle with a clear increase in the uptake from land during the summer. The smallest land fraction was in the winter (DJF), with an average of 15 ± 12%, and the biggest in the summer (JJA), with an average of 55 ± 22%. The period from March (27 ± 20%) to June (53 ± 23%) showed an increase, and the period from August (57 ± 23%) to November (23

a) Uptake distance

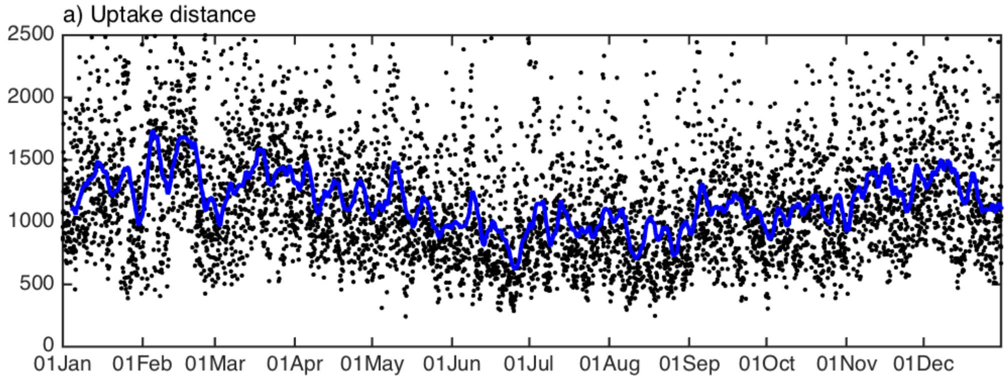

b) Uptake time

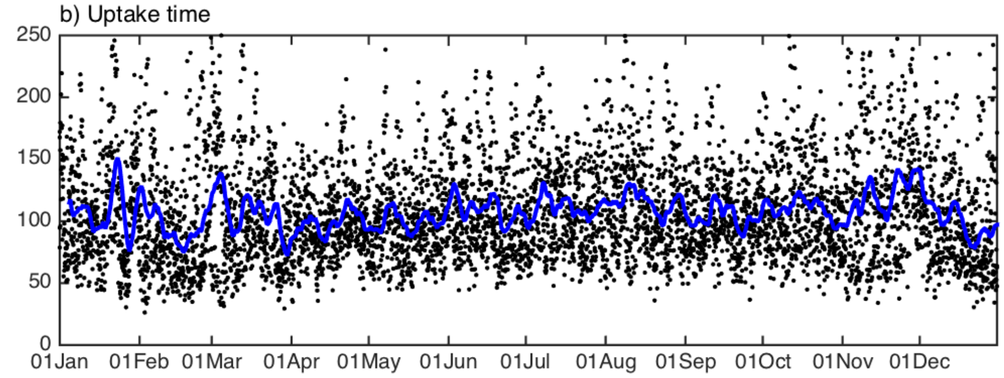

Figure 5.7: Time series of the moisture source properties for the years from 2001 to 2004. (a) Uptake distance [km] for the moisture uptake. (b) Uptake time [h] for the moisture uptake. The black dot indicate an average of the moisture reaching Tustervatn every 6 hours. The blue line shows the running mean.

± 17%) showed a decrease. The summer months exhibited a much higher variability. The summer months had a span from ∼ 0 to 100%, with their highest contribution between ∼ 20 to 90%, while the winter months had a span from ∼ 0 to 60%, with their biggest contribution from ∼ 0 to 40%

The skin temperature, shown in Figure 5.6b, is also exhibiting a clear seasonal cycle. The highest average temperatures were located in July and August (11.3 ± 7.6°C), and the lowest in March and April (3.7 ± 5.6°C). The winter months (DJF; 5.3 ± 5.4°C) being higher than March (3.8 ± 5.0°C) and April (3.5 ± 6.2°C), could originating from the high moisture uptake from the ocean, corresponding with what we found for NEEM. The period from April (3.5 ± 6.2°C) to July (11.4 ± 6.9°C) showed an increase in the skin temperature, and the period from August (11.1 ± 8.2°C) to November (6.7 ± 6.0°C) showed a decrease. This corresponded well in time with when the land fraction increased and decreased.

The uptake distance is shown in Figure 5.7a. It exhibited a clear seasonal cycle with

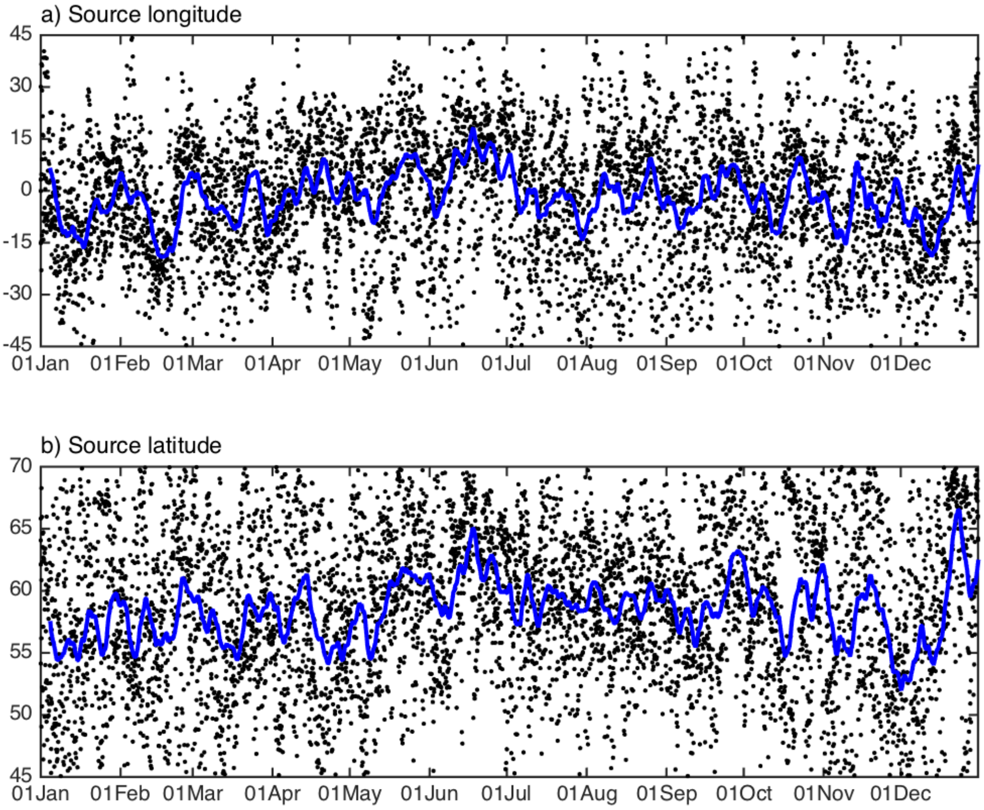

Figure 5.8: Time series of the moisture source properties for the years from 2001 to 2004. (a) Source longitude [°] of the moisture uptake. (b) Source latitude [°] of the moisture uptake. The black dots indicate an average of the moisture reaching Tustervatn every 6 hours. The blue line shows the running mean.

an increase of ∼ 400 km from winter to summer. The highest uptake distance was from December, January and February (1320 ± 510 km), the shortest in June, July and August (940 ± 410 km). The seasonal cycle of the uptake distance corresponded well with the land fraction, shown in Figure 5.6a. The period with the lowest uptake distance corresponded with the period with the biggest contribution from land, and the period with the highest uptake distance corresponded with the contribution from the ocean. The variability was slightly higher in the winter than the summer, and contained more abnormal high values (not shown).

The uptake time is shown in Figure 5.7b, showing no clear trends or seasonal cycle. The highest uptake times were located in November (120 ± 55 h) and August (115 ± 40 h), and the lowest in February (95 ± 45 h) and December (100 ± 40 h). The uptake time was located within ∼ 25 to 310 h, with the biggest contribution from ∼ 50 to 150 h. The winter months had a slightly higher variability, and contains some abnormal high values (not shown).

The source longitude is shown in Figure 5.8a. Tustervatn (13.92°E) had its biggest contribution between 30°W to 30°E (whole span from 100°W to 100°E). December, January and February (6 ± 17°W) showed the months with the biggest contribution from the west, while May and June (5 ± 19°E) showed the biggest contribution from the east.

Tustervatn had from Figure 5.5, a big contribution from the Norwegian Sea, which corresponds with the average being west of Norway. That the summer months had its source longitude closer to Tustervatn, was expected from the increased land fraction, and moisture uptake over Norway. The summer had also the highest outliers from the west, which is consistent with Figure 5.5. The winter uptake primarily coming from the Norwegian Sea was consistent with the time of the biggest contribution from the west.

The source latitude is shown in Figure 5.7b, exhibiting a smaller seasonal cycle. The summer (JJA) had an average of 60 ± 5°N, while the winter (DJF) had an average of 58 ± 7°N. The winter months had however a lower span, from ∼ 35 to 70°N, while the summer had a span from ∼ 40 to 75°N.

The moisture uptake for 1997, 1999 and 2003 is shown in Figure A.3 - A.5. The moisture uptake showed no clear trends through the years, but contained fluctuations from one year to another. Time series of the properties for the years from 1997 to 2000 are shown in Figure A.6 - A.8. The time series shows no clear changes from the data from 2001 to 2004.

5.2 Comparison with the measurements

5.2.1 The summer field at NEEM

Data from the summer field at NEEM from 20 May to 4 August 2012 are shown in Figure 5.9. D-excess and δD from the measurements at NEEM are shown in (a) - (b). The result from the Lagrangian moisture source diagnostic are shown in (c) - (i). The periods shaded in red and blue are periods with high and low d-excess. The blue are periods with markedly higher d-excess, and the red are periods with markedly lower d-excess than average at NEEM. The relationship between d-excess and δD, land fraction, skin temperature, surface specific humidity, uptake distance and time, and source longitude and latitude is shown in Figure 5.10 and 5.11.

The observed d-excess (23.9 ± 5.5‰) was higher than the global average (10 ‰). The measurements for 2012 had a span from 11.4 to 41.6‰, and showed an increase from May (20.7 ± 4.5‰) to August (26.7 ± 5.8‰). D-excess and δD exhibited a clear anticorrelation ($R = -0.56$), shown in Figure 5.10a, and the highest d-excess appeared with the lowest δD.

From Figure 5.9, the higher (lower) d-excess is related to higher (lower) land fraction, lower (higher) skin temperatures, lower (higher) surface specific humidity, lower (higher) uptake distance and higher (lower) source latitude. The uptake time and source longitude showed no clear association with the changes in d-excess.

The relationship between d-excess and land fraction is shown in Figure 5.10b. Land

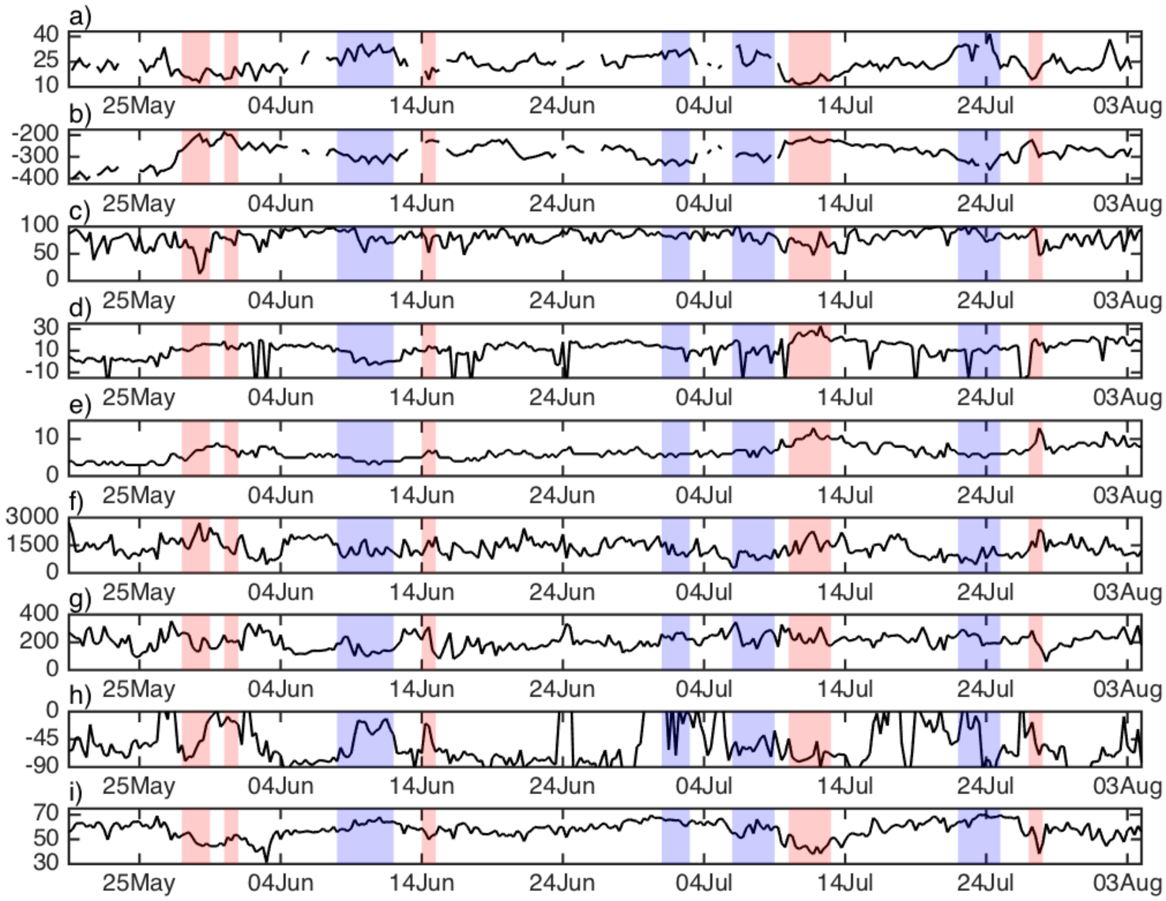

Figure 5.9: Data from the summer field campaign at NEEM, from 20 May to 4 August 2012. (a) Shows the d-excess [‰], (b) δD [‰], (c) land fraction [%], (d) skin temperature [°C], (e) surface specific humidity [g kg^{-1}], (f) uptake distance [km], (g) uptake time [h], (h) source longitude [°] and (i) source latitude [°]. The black curve shows the average of all the moisture reaching NEEM in an interval of 6 h. The blue and red shaded periods are periods with high and low d-excess.

fraction showed a smaller correlation with d-excess (R = 0.25). The higher d-excess corresponded with higher uptake over land. The low d-excess had an average land fraction of 67.4 ± 18.7‰, while the high d-excess had an average of 83.2 ± 10.5‰. Moisture uptake from ocean areas also had a higher ability for uptake of the heavier δD molecule. An increase in δD without a similar 1:8 increase in δ^{18}O will lead to an increase in the d-excess.

The skin temperature, shown in Figure 5.10c, exhibited an anticorrelation with d-excess (R = −0.19). The effect seemed however to have been bigger for lower d-excess ($R^2 = 0.19$, period in red) than for the higher d-excess ($R^2 = 0.01$, blue period). This also seemed to be

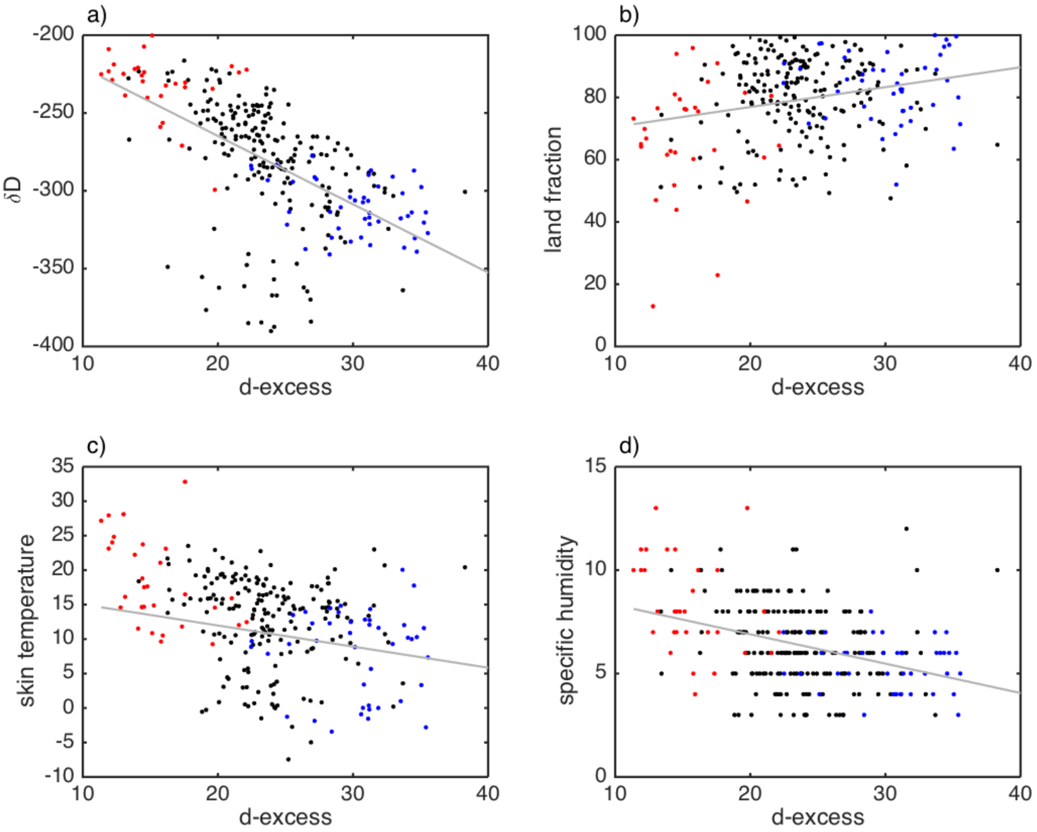

Figure 5.10: The relationship between deuterium excess and (a) δD [‰], (b) land fraction [%], (c) skin temperature [°C], (d) surface specific humidity [g kg^{-1}]. The dots indicate an average of the moisture reaching NEEM every 6 h. The blue and red dots indicate the periods with high and low d-excess, shown in Figure 5.9. The grey line shows the linear trend.

the case for the surface specific humidity, shown in Figure 5.10d. Showing an anticorrelation with d-excess (R = -0.39), with bigger effect for the lower d-excess ($R^2 = 0.15$), than for the higher d-excess ($R^2 = 0.02$). The low d-excess had an average skin temperature of 16.8 ± 8.4°C, and surface specific humidity of 8.2 ± 2.3 g kg^{-1}. The high d-excess had an average skin temperature of 7.3 ± 7.8°C, and surface specific humidity of 5.5 ± 1.1 g kg^{-1}. The heavier $H_2^{18}O$ molecules need more energy to vaporize than the lighter HDO molecule, and an increase in temperature is therefore consistent with an enrichment of the heavier δ^{18}O, which could lead to a decrease in d-excess.

The uptake distance and time, shown in Figure 5.11a-b, both showed an increase in d-excess for decreasing values. The uptake distance ($R^2 = 0.06$) and time ($R^2 = 0.02$) was poorly correlated. The low d-excess had an average uptake distance of 1584 ± 443 km, while the high d-excess had an average distance of 1039 ± 342 km. The difference in the

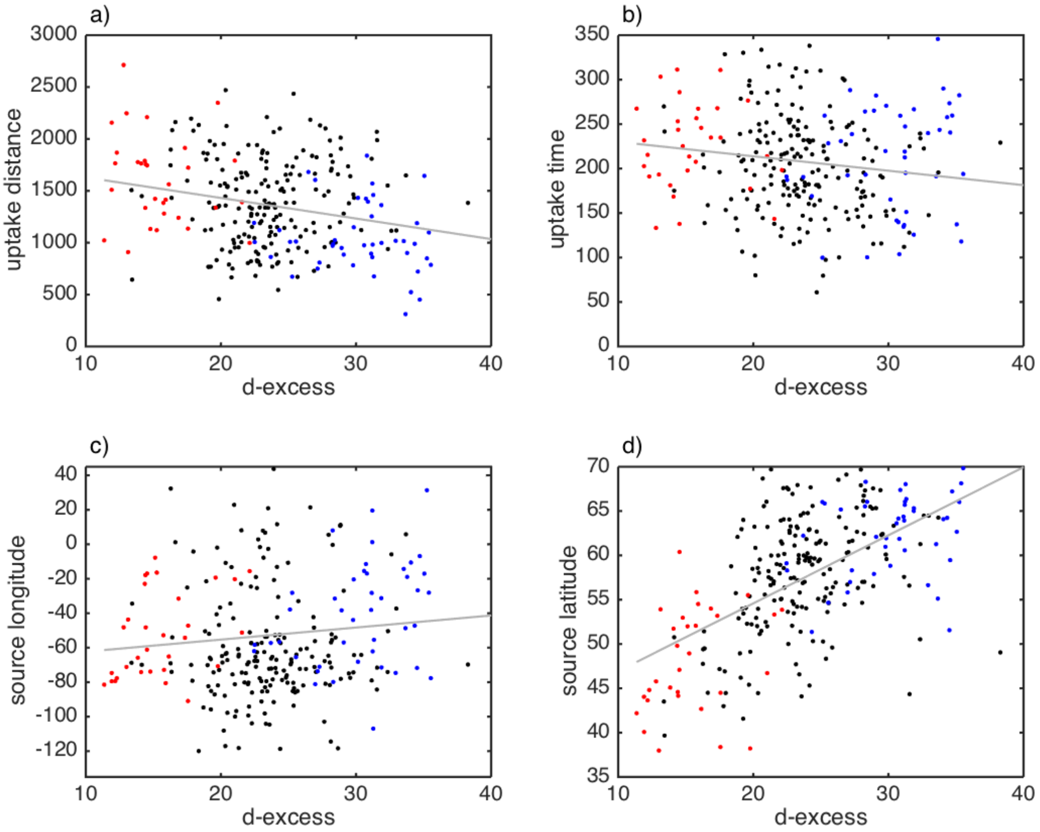

Figure 5.11: The relationship between deuterium excess and (a) uptake distance [km], (b) uptake time [h], (c) source longitude [°], (d) source latitude [°]. The dots indicate an average of the moisture reaching NEEM every 6 h. The blue and red dots indicate the periods with high and low d-excess, shown in Figure 5.9. The grey line shows the linear trend.

uptake time was low, and the low d-excess had an average of 225 ± 48 h, while the high d-excess had an average of 210 ± 60 h.

The source longitude, shown in Figure 5.11c, showed the smallest correlation with d-excess (R = 0.10). The low d-excess had an average source longitude of 53.2 ± 24.8°W, while the high d-excess had an average of 38.5 ± 37.6°W. Meaning that the low d-excess have come from areas over Greenland, while the high d-excess have come from ocean areas east of Greenland. The longitudinal dependency could originate from the dependency on land fraction found earlier.

The source latitude, shown in in Figure 5.11d, showed the highest correlation with d-excess, R = 0.58. Uptake from lower latitudes corresponded with lower d-excess and uptake from higher latitudes corresponded with higher d-excess. This is consistent with findings from Kurita (2011) and Steen-Larsen *et al.* (2013), of a distinct higher d-excess from higher latitudes. The low d-excess had an average source latitude of 48.5 ± 6.2°N, while the high d-excess had an average of 62.6 ± 4.8°N. The latitudinal dependency could be the reason behind the small trend in the uptake distance and time.

Figure 5.12 illustrate the latitudinal effect on d-excess. The high d-excess, shown in (a), shows moisture uptake from higher latitudes, while the low d-excess, shown in (b) shows moisture uptake from lower latitudes.

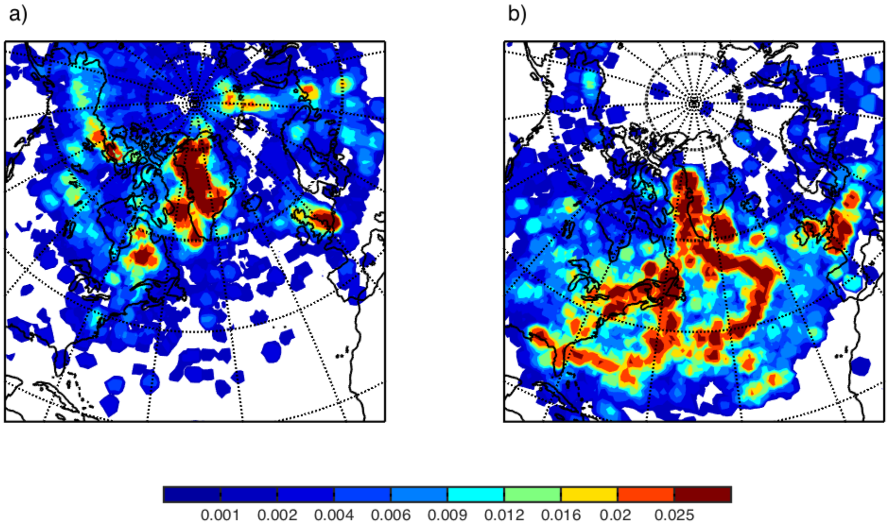

Figure 5.12: The moisture source for water vapour identified with a 20-days back trajectory, showing the location of the moisture uptake (in mm $6h^{-1}$). The high d-excess from Figure 5.9 is shown in (a), and the low d-excess is shown in (b).

The average values of the periods displayed in Figure 5.9 are shown in Table 5.1. The average values showed a clear difference between the high and low d-excess, most markedly was the dependency on δD, land fraction, skin temperature, uptake distance and source latitude.

The high and low d-excess for the years 2010 and 2011 were also studied, and their respective periods are shown in Figure B.1 and B.2 in Appendix B. The average values for the years from 2010 to 2012 are shown in Table B.1 in Appendix B. The average values from 2010 to 2012 support our findings of a dependency between d-excess and the land fraction, skin temperature, surface specific humidity, uptake distance and source longitude

Table 5.1: The average values of d-excess [‰], δD [‰], , land fraction [%], skin temperature [°C], surface specific humidity [g kg^{-1}], uptake distance [km], uptake time [h], source longitude [°W] and latitude [°N], for the period shown in Figure 5.9.

	Red period: Low d-excess	Black period:	Blue period: High d-excess
D-excess	15.5 ± 2.9	23.6 ± 3.9	30.5 ± 3.9
δD	−228.1 ± 22.1	−282.1 ± 40.5	−311.7 ± 18.8
Land fraction	67.4 ± 18.7	80.4 ± 12.7	83.2 ± 10.5
Skin temperature	16.8 ± 8.4	10.6 ± 9.8	7.2 ± 7.8
Surface specific humidity	8.2 ± 2.3	6.2 ± 1.9	5.5 ± 1.1
Uptake distance	1584.4 ± 443.2	1385.4 ± 432.1	1038.6 ± 342.0
Uptake time	225.3 ± 47.7	204.1 ± 56.0	210.7 ± 60.5
Source longitude	53.2 ± 24.8	55.4 ± 39.3	38.5 ± 37.6
Source latitude	48.5 ± 6.2	57.9 ± 6.3	62.6 ± 4.8

and latitude.

NEEM also conducted data of δD. δD is not expected to preserve the conditions from the evaporation location, and the correlation with the variables from the Lagrangian moisture source diagnostic is expected to be poor. δD have however greater correlation with surface specific humidity ($R^2 = 0.33$) and source latitude ($R^2 = 0.28$). Skin temperature ($R^2 = 0.12$) also had some relevance. The correlation with land fraction ($R^2 = 0.01$), uptake distance ($R^2 = 0.02$) and time ($R^2 = 0.00$), and source longitude ($R^2 = 0.02$) was poor.

A summary of the correlation for d-excess and δD is shown in Table 5.2.

Table 5.2: Correlation for d-excess and δD, with the variables from the Lagrangian moisture source diagnostic for NEEM.

	D-excess: R	R^2	δD: R	R^2
Land fraction	0.25	0.06	−0.08	0.01
Skin temperature	−0.19	0.03	0.35	0.12
Surface specific humidity	−0.39	0.15	0.58	0.33
Uptake distance	−0.24	0.06	0.12	0.02
Uptake time	−0.15	0.02	0.04	0.00
Source longitude	0.10	0.01	−0.13	0.02
Source latitude	0.58	0.33	−0.53	0.28

The correlations for d-excess and δD for the years from 2010 to 2012 are shown in Table B.2 in Appendix B. The correlation from 2010 to 2012 being lower than for 2012 alone, may be due to the measurements from 2010 being less accurate than the measurements from 2011 and 2012. This was due to changes in the temperature-regulated box where the measurements were conducted (Steen-Larsen *et al.*, 2014).

5.2.2 δ^{18}O measurements from Tustervatn

The δ^{18}O measurements from Tustervatn are further investigated. Since δ^{18}O was conducted from precipitation samples, the Lagrangian moisture source diagnostic was run to trace the precipitation at Tustervatn.

The relationship between δ^{18}O and land fraction, skin temperature, surface specific humidity and a precipitation estimate is shown in Figure 5.13. The relationship between δ^{18}O and uptake distance and time, and the source longitude and latitude is shown in Figure 5.14. The lowest and highest δ^{18}O are highlighted to look for difference in their average values. The red dots indicate δ^{18}O values less than -19.0‰, and the blue dots indicate δ^{18}O values higher than -6.2‰. δ^{18}O had an interval from -3.2 to -29.7‰.

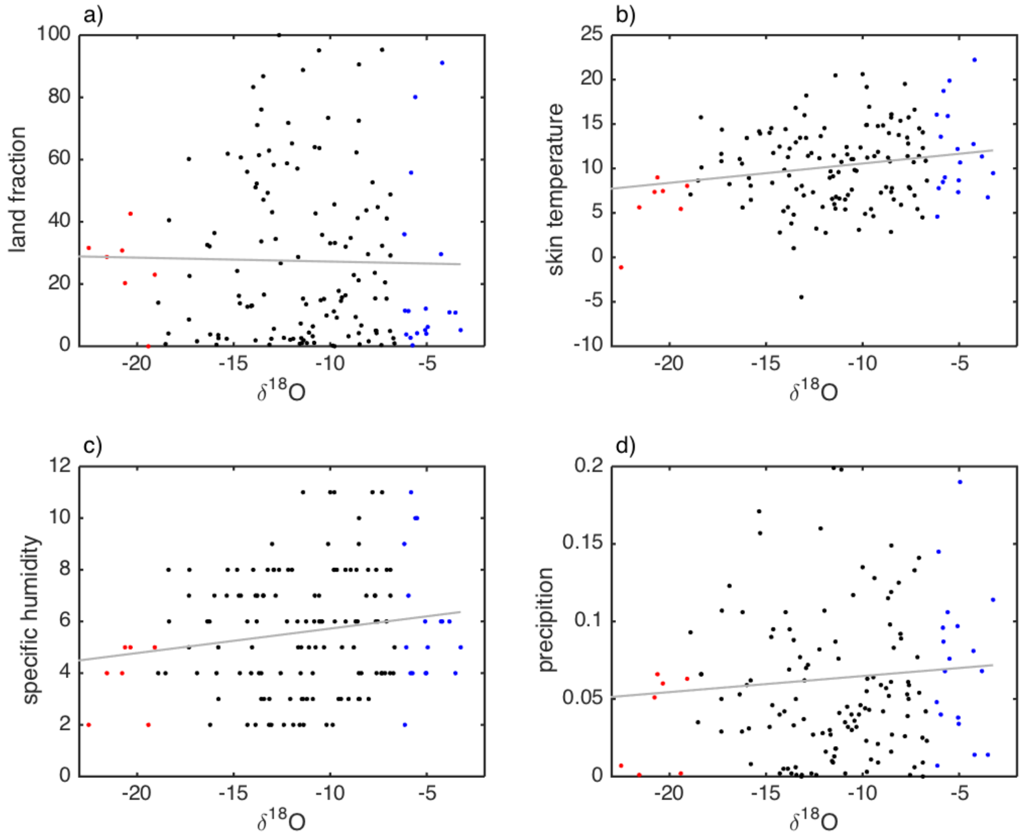

Figure 5.13: The relationship between $\delta^{18}O$ [‰] and (a) land fraction [%], (b) skin temperature [^oC], (c) surface specific humidity [g kg^{-1}], (d) precipitation estimate [mm 6h^{-1}]. The dots indicate an average of the moisture reaching Tustervatn every 6 h. The blue dots indicate values of $\delta^{18}O >$ -6.2‰, and the red dots indicate values of $\delta^{18}O <$ -19.0‰.

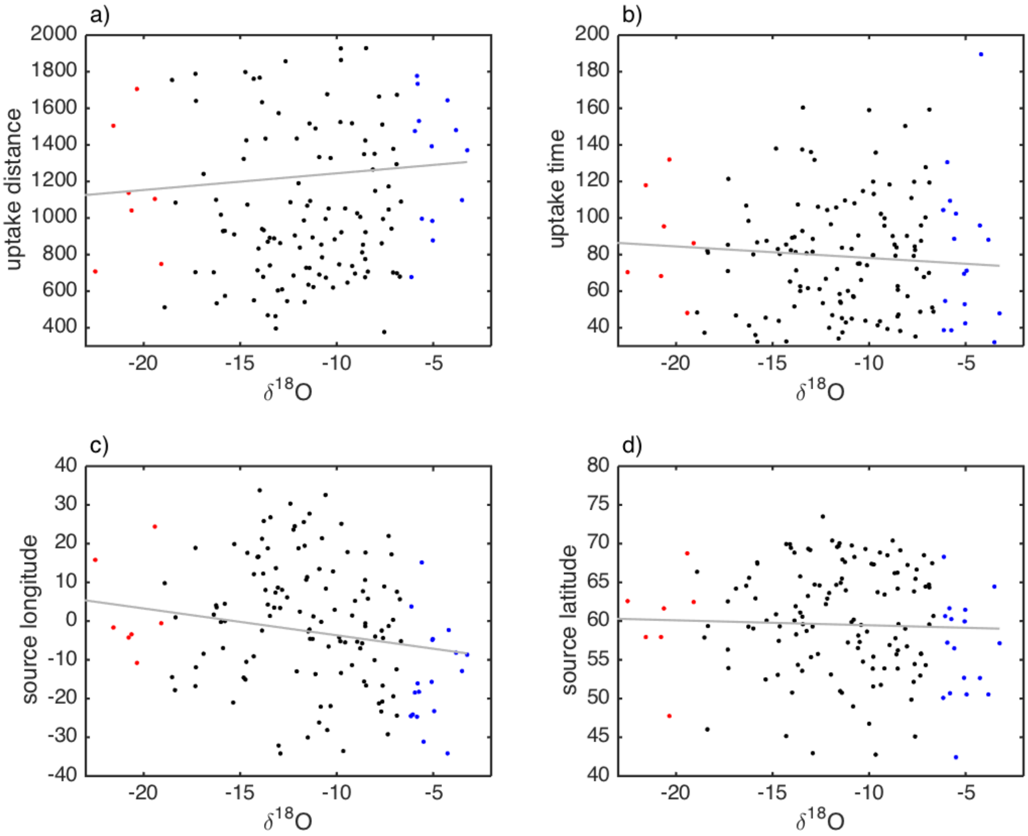

Figure 5.14: The relationship between $\delta^{18}O$ [‰] and (a) uptake distance [km], (b) uptake time [h], (c) source longitude [°], (d) source longitude [°]. The dots indicate an average of the moisture reaching Tustervatn every 6 h. The blue dots indicate values of $\delta^{18}O >$ -6.2‰, and the red dots indicate values of $\delta^{18}O <$ -19.0‰.

δ^{18}O is not expected to preserve the information from the evaporation site, as is mostly driven by air mass distillation. Hence, the correlation with the result from the evaporation location was expected to be poor.

The relationship with land fraction is shown in Figure 5.13a. The land fraction showed no clear correlation with δ^{18}O ($R = -0.02$), and both the high and low δ^{18}O values had an average of $\sim 20\%$. The high δ^{18}O had however a much higher variability.

The highest dependency for δ^{18}O was found with the skin temperature ($R = 0.24$) and surface specific humidity ($R = 0.20$). The skin temperature is shown in Figure 5.13b. The low δ^{18}O values had an average skin temperature of 6.4 ± 2.9°C, while the high δ^{18}O had an average of 12.0 ± 4.9°C. This is consistent with the fact that the heavier $H_2^{18}O$ molecules need more energy to vaporize. The surface specific humidity, shown in Figure 5.13b, also showed an increase for increasing δ^{18}O. The low δ^{18}O had an average surface specific humidity of 4.0 ± 1.2 g kg^{-1}, while the high δ^{18}O had an average of 6.0 ± 2.5 g kg^{-1}. Increased surface humidity give higher ability of uptake of the heavy isotope δ^{18}O.

The precipitation estimate is shown in Figure 5.13d, and is an estimate of the precipitation at the measuring site. The precipitation estimate showed a small increase in δ^{18}O for increasing precipitating amount. The low δ^{18}O had an average of 0.05 ± 0.04 mm 6h^{-1}, while the high δ^{18}O had an average of 0.07 ± 0.05 mm 6h^{-1}. The high δ^{18}O had however a much higher variability.

The uptake distance and time, shown in 5.14a-b, showed a smaller relationship with δ^{18}O. The uptake distance (R = 0.08) showed a small correlation, while the uptake time (R = −0.09) showed a small anticorrelation. The high δ^{18}O values corresponded with the lowest uptake distances (1266.5 ± 483.7 km) and the highest uptake times (93.9 ± 37.6 h), while the low δ^{18}O values corresponded with the highest uptake distances (1570.0 ± 562.7 km) and the lowest uptake times (76.9 ± 41.5 h). Both the uptake distance and time had a large variability, and the changes seemed to be arbitrary.

The relationship with the source longitude is shown in Figure 5.14c and it showed one of the highest dependencies for δ^{18}O. The correlation was R = −0.19. The low δ^{18}O had an average of 1.4 ± 13.0°W, while the high δ^{18}O had an average of 14.1 ± 12.6°W. Both averages were located in the Norwegian Sea. This could correspond with a higher ability for uptake of the heavier δ^{18}O molecule over water. Longer distances over water will give a higher enrichment.

The relationship with the source latitude is shown in Figure 5.14d. The low δ^{18}O values showed an average of 58.5 ± 6.8°N, while the high δ^{18}O values showed an average of 54.8 ± 8.9°N. The correlation was however poor, R = − 0.04.

The average values of each period are shown in Table 5.3, and a summary of the correlation for δ^{18}O is shown in Table 5.4.

Table 5.3: The average values of δ^{18}O [‰], land fraction [%], skin temperature [°C], surface specific humidity [g kg^{-1}], precipitation estimate [mm 6h^{-1}], uptake distance [km], uptake time [h], source longitude [°W] and latitude [°N], for the periods displayed.

	Red period: δ^{18}O < -19.0‰	Black period: -19.0 < δ^{18}O < -6.2‰	Blue period: δ^{18}O > -6.2‰
$\delta^{18}O$	-22.6 ± 3.3	-11.6 ± 3.3	-5.1 ± 0.9
Land fraction	23.6 ± 14.8	28.7 ± 26.9	21.2 ± 27.4
Skin temperature	6.4 ± 2.9	10.3 ± 4.4	12.0 ± 4.9
Surface specific humidity	4.0 ± 1.2	5.6 ± 2.3	6.0 ± 2.5
Precipitation estimate	0.05 ± 0.04	0.06 ± 0.06	0.07 ± 0.05
Uptake distance	1266.5 ± 483.7	1176.0 ± 555.8	1570.0 ± 562.7
Uptake time	93.9 ± 37.6	78.2 ± 33.0	76.9 ± 41.5
Source longitude	-1.4 ± 13.0	-0.9 ± 18.5	-14.1 ± 12.6
Source latitude	58.5 ± 6.8	60.4 ± 7.0	54.8 ± 8.9

The low δ^{18}O values were showing a higher correlation with uptake distance (R^2 =

Table 5.4: Correlation between δ^{18}O and the variables from the Lagrangian moisture source diagnostic for Tustervatn.

	δ^{18}O: R	 R^2
Land fraction	−0.02	0.00
Skin temperature	0.24	0.06
Surface specific humidity	0.20	0.04
Precipition estimate	0.09	0.01
Uptake distance	0.08	0.01
Uptake time	−0.09	0.01
Source longitude	−0.19	0.04
Source latitude	−0.04	0.00

0.20), source longitude (R^2 = 0.29) and latitude (R^2 = 0.10). The high δ^{18}O showed no clear changes from the correlation with the whole period.

The δ^{18}O measurements from 2002 to 2004 were also compared to the variables from the Lagrangian moisture source diagnostic. The average values for the high and low δ^{18}O values are shown in Table B.3 in Appendix B.2, and the correlations between δ^{18}O and the variables from the Lagrangian moisture source diagnostic are displayed in B.4.

Our findings from 2001, of the dependency between δ^{18}O and the skin temperature, surface specific humidity and source longitude, were supported by the data from 2002 to 2004. The land fraction showed a slightly higher dependency for the data from 2002 to 2004, while the source latitude showed a smaller dependency.

5.3 Case studies

Smaller periods (2 to 3 days) from NEEM, with markedly changes, are further investigated. Their respective periods are shown in Table 5.5.

Table 5.5: The period, d-excess, temperature and humidity interval for the case studies at NEEM.

	Period	Interval of d-excess [‰]	Temperature interval [°C]	Humidity interval [ppmv]
Case 1:	06.07.12 - 11.07.12	11.4 to 34.5	-12.1 to 0.9	1842.7 to 6316.0
Case 2:	16.06.10 - 21.06.10	19.0 to 54.0	-14.5 to -3.4	2150.9 to 5647.9
Case 3:	25.06.10 - 03.07.10	22.5 to 59.4	-18.5 to -3.2	1792.7 to 4337.3

2012 contained two periods with abnormally high temperatures, namely 6 to 12 July and 24 to 29 July, the first is being further investigated in section 5.3.1. The data from 2010 contained a lot of fluctuations in d-excess, and two of the periods are further investigated in section 5.3.2 and 5.3.3. The data from 2011 is much more smooth and no particular period has been chosen to look further into.

5.3.1 6 July - 11 July 2012

The period from 6 to 11 July 2012 was characterized by an extreme warm and moist conditions over Greenland, causing one of the largest meltings of the ice sheet ever recorded in the last century (Nghiem *et al.*, 2012). Because of the rare event, it have been the topic for several studies (e.g. Nghiem *et al.* (2012), Neff *et al.* (2014) and Bonne *et al.* (2015)).

The measurements from NEEM for the period are illustrated in Figure 5.15, showing a large change in d-excess from 34.5‰ to 11.4‰. The d-excess values were highly correlated with the measurements of temperature ($R^2 = 0.82$), humidity ($R^2 = 0.89$) and δD ($R^2 = 0.82$).

The largest change was from 8 to 10 July, with temperatures going from -12.1°C to 0.5°C, the humidity increased from 2009.6 ppmv to 6224.7 ppmv and d-excess decreased from 29.8‰ to 13.1‰. In only 12 hours on 9 July, the changes were huge, the temperature went from -10.3°C to 0.5°C, the humidity from 2626.7 ppmv to 6224 ppmv and d-excess from 24.3‰ to 13.4‰.

The rare warming continued, and reached its highest temperature value of 2.9 °C on 13 July (18 h). On the 12 July melting occurred over 98.6% of Greenland (Nghiem *et al.*, 2012). The warm period lasted to 15 July.

The Lagrangian moisture source diagnostic was used to investigate the origin the moisture, as was done in Bonne *et al.* (2015). A time series of our results is shown in Figure 5.16, and the trajectories and moisture uptake are shown in Figure 5.17 and 5.18.

The moisture source showed a clear change in the evaporation conditions. The two first days, till 8 July, were characterized by moisture coming from higher latitudes with shorter uptake time and distance. For the next two days, from 9 to 10 July, which contained the large change in d-excess, temperature and humidity, we saw a clear shift in the uptake pattern. The 9 July was characterized by a local moisture uptake, shown in Figure 5.18b. The 10 July had a clear increase in the uptake, and the moisture was transported all the way from the subtropical North Atlantic Ocean and North America, shown in Figure 5.18d. This corresponded with higher skin temperature, lower uptake from land, higher surface specific humidity and longer uptake distance and time, shown in Figure 5.16. The following days, with high temperature and humidity, were also characterized by moisture uptake from the subtropical North Atlantic Ocean and North America (not shown).

The d-excess from 8 to 10 July was highly correlated with source latitude ($R^2 = 0.69$) and uptake distance ($R^2 = 0.47$), the correlation with land fraction ($R^2 = 0.32$) and surface specific humidity ($R^2 = 0.31$) was also high.

The temperature and integrated water vapour plots are shown in Figure 5.19 and 5.20. On the 8 July, shown in Figure 5.19e, an air mass containing warm and moist air was hitting the southern part of Greenland, before moving further north on the 9 and 10 July

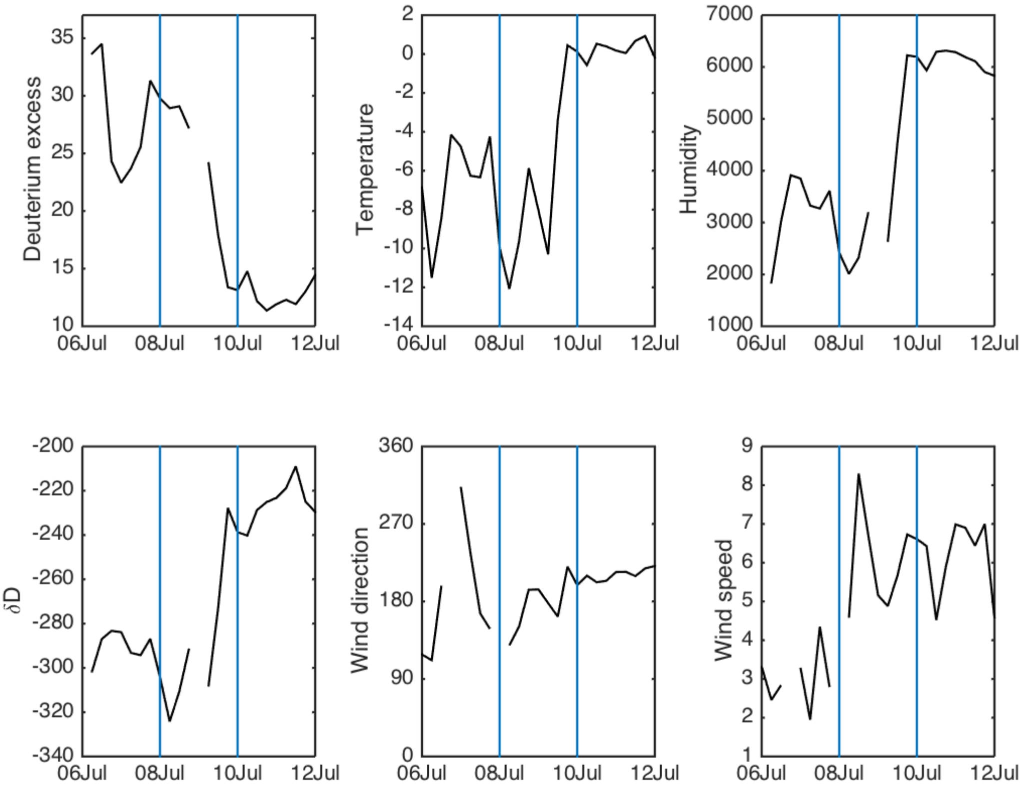

Figure 5.15: The measurements from NEEM for the period 06.07.12 (00 h) to 12.07.12 (00 h). Showing the changes in d-excess [‰], temperature [°C], humidity [ppmv], δD [‰], wind direction [°] and speed [m s^{-1}]. The blue vertical line shows the chosen division of the period, 08.07.12 and 10.07.12.

(Figure 5.20a and c). On the 11 July, shown in Figure 5.20e, the air mass went eastward, and the entire Greenland was covered by warm and moist air.

Neff *et al.* (2014) described the atmospheric mass hitting Greenland as an atmospheric river. An atmospheric river is a narrow corridor carrying a large amount of water vapour in the troposphere, and is seen to have a central role in the transport of moisture from the south to north (Newell *et al.* 1992, Sodemann and Stohl 2013). The atmospheric river is also easily notable in the integrated water vapour plot in Figure 5.20b.

Bonne *et al.* (2015) examined observation of snow pit impurities at NEEM for the specific period, and found an increase in the concentration of sodium (Na$^+$) for the days of the melting period. These high amount of sea salt had not earlier been recorded at NEEM. The high values may suggest that the moisture was coming from an air mass which was unusually enriched in sea salt, which corresponds well with our uptake from the subtropical North Atlantic Ocean.

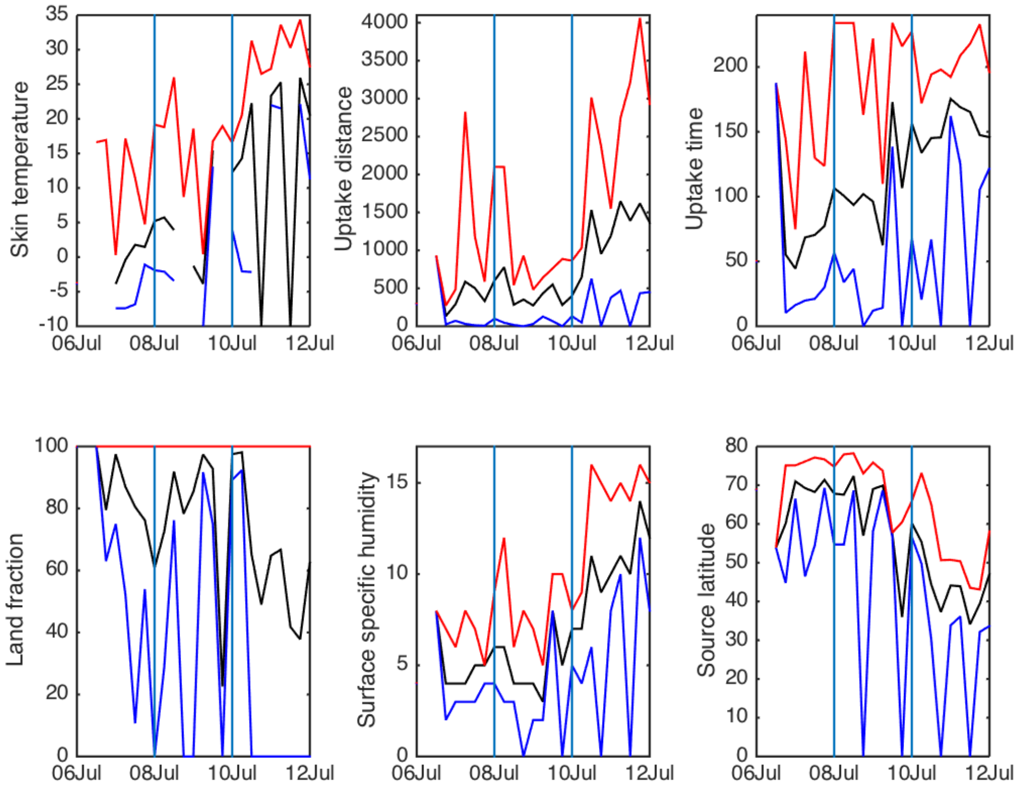

Figure 5.16: Time series of the moisture source properties for the period from 5 to 13 July 2012, showing the skin temperature [°C], uptake distance [km], uptake time [h], land fraction [%], surface specific humidity [g kg^{-1}] and source latitude [°N]. The black curve shows the average, the red the maximum and the blue the minimum values of the moisture source arriving at a given time (every 6 h).

From a sudden change in source latitude from $\sim$ 70 to 40°, we would expect changes in d-excess. An increase in the moisture coming from low latitudes with warmer moisture source, will contain low d-excess values. High relative humidity at the evaporation location will also cause low d-excess, which will likely be the case for the uptake at the subtropical North Atlantic. A corresponding increase in δD and decrease in d-excess is also a good indicator of subtropical moisture source (Bonne *et al.*, 2015).

We have shown that the period from 6 to 11 July support the hypothesis that d-excess conserve the values from the evaporation site.

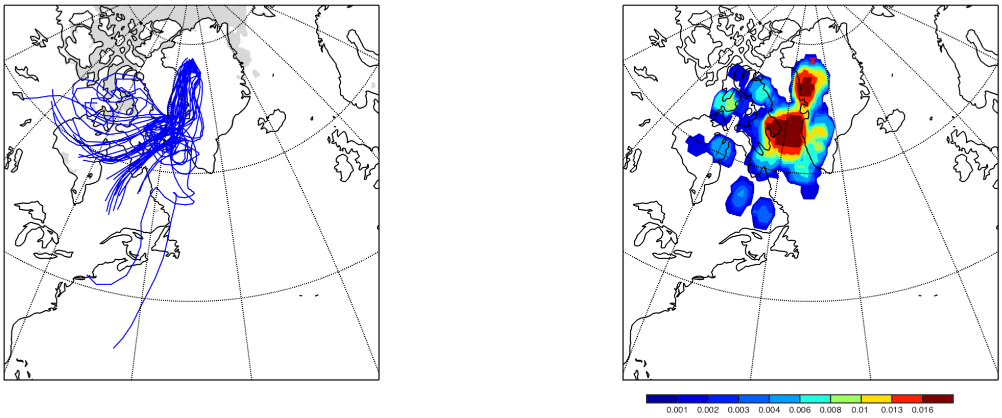

(a) Trajectories for 06.07.12. (b) Uptake for 06.07.12.

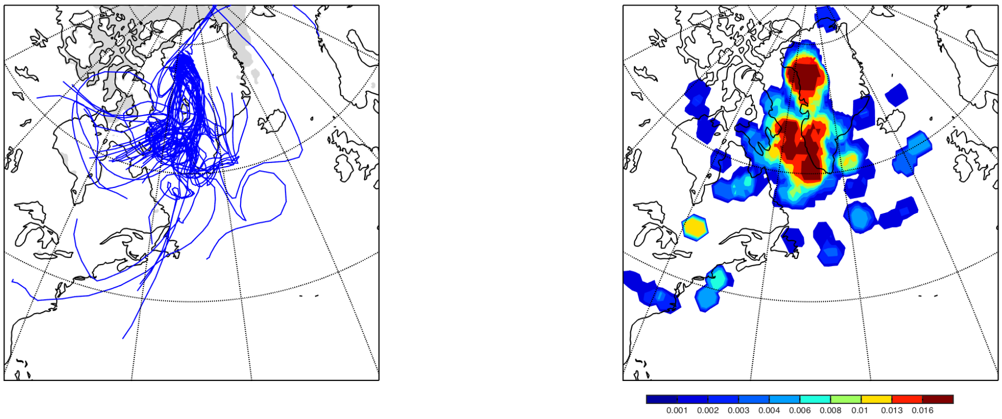

(c) Trajectories for 07.07.12. (d) Uptake for 07.07.12.

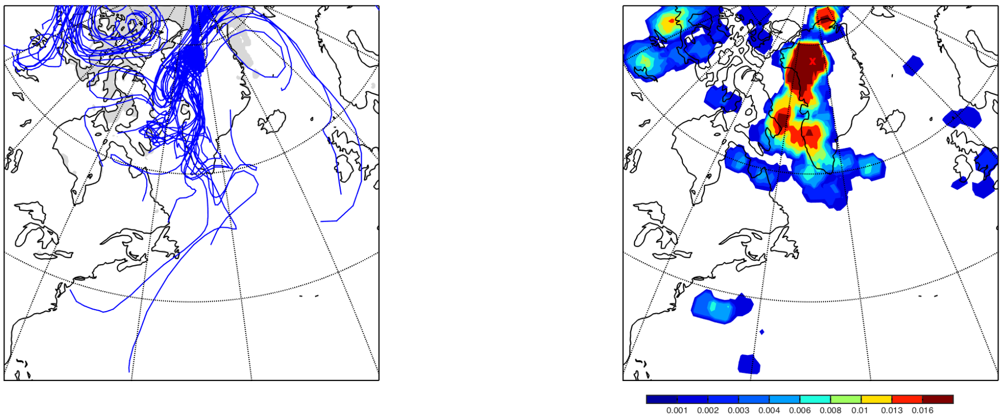

(e) Trajectories for 08.07.12. (f) Uptake for 08.07.12.

Figure 5.17: The moisture source identified with a 10-days back trajectory for 6 to 8 July 2012. The right panels shows the path of the water vapour (blue line). The grey area indicate where the sea ice concentration exceeds 50%. The left panels shows the location of the moisture uptake (in mm 6h^{-1}).

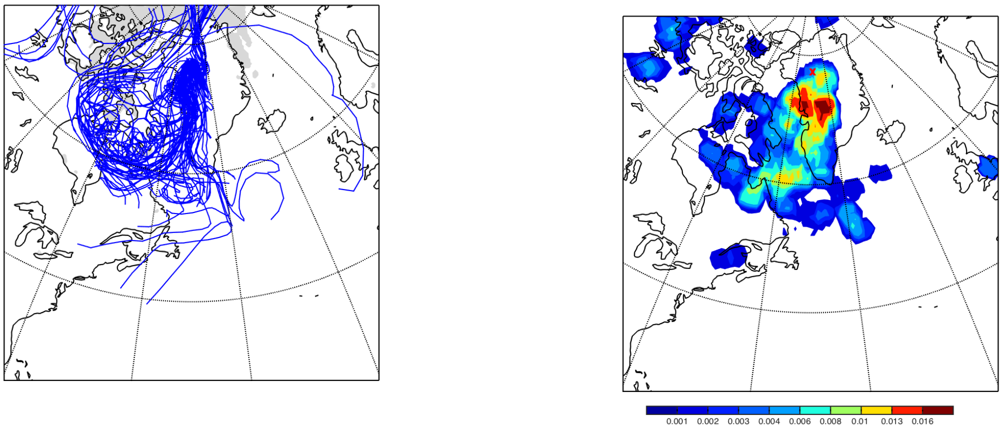

(a) Trajectories for 09.07.12.

(b) Uptake for 09.07.12.

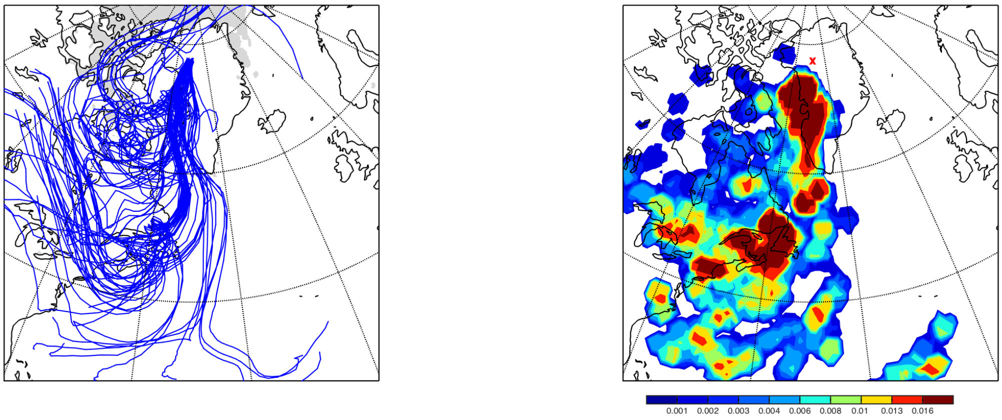

(c) Trajectories for 10.07.12.

(d) Uptake for 10.07.12.

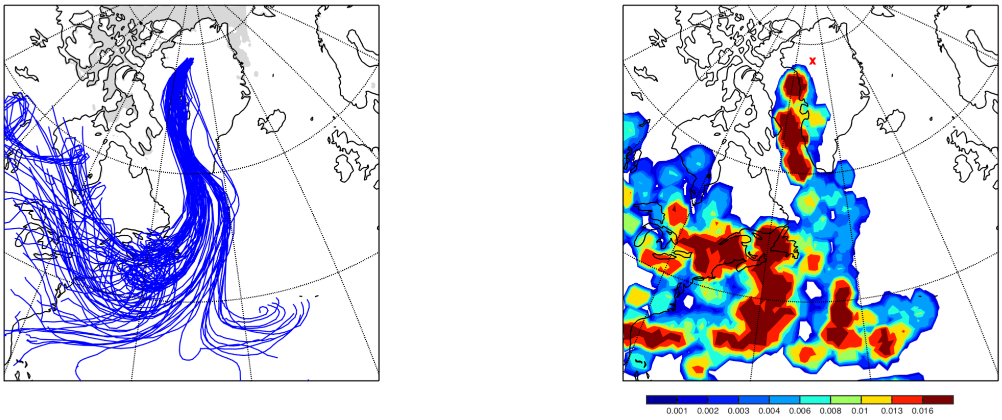

(e) Trajectories for 11.07.12.

(f) Uptake for 11.07.12.

Figure 5.18: The moisture source identified with a 10-days back trajectory for 9 to 11 July 2012. The right panels shows the path of the water vapour (blue line). The grey area indicate where the sea ice concentration exceeds 50%. The left panels shows the location of the moisture uptake (in mm $6h^{-1}$).

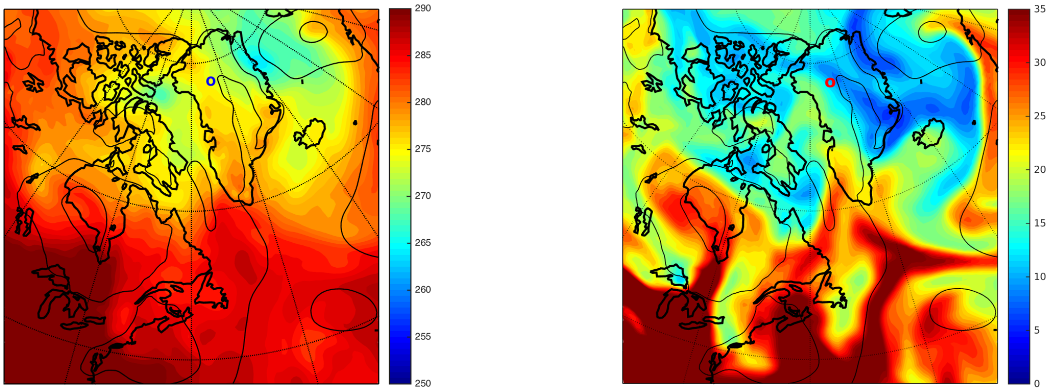

(a) Temperature on 06.07.12.

(b) Integrated water vapour on 06.07.12.

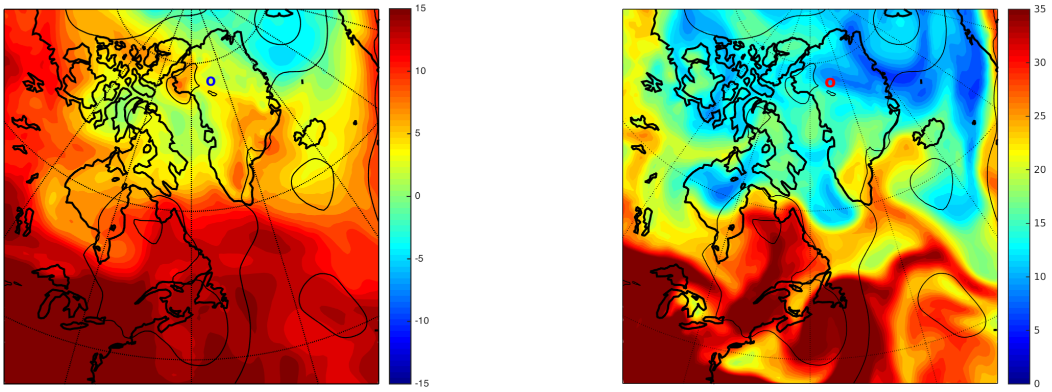

(c) Temperature on 07.07.12.

(d) Integrated water vapour on 07.07.12.

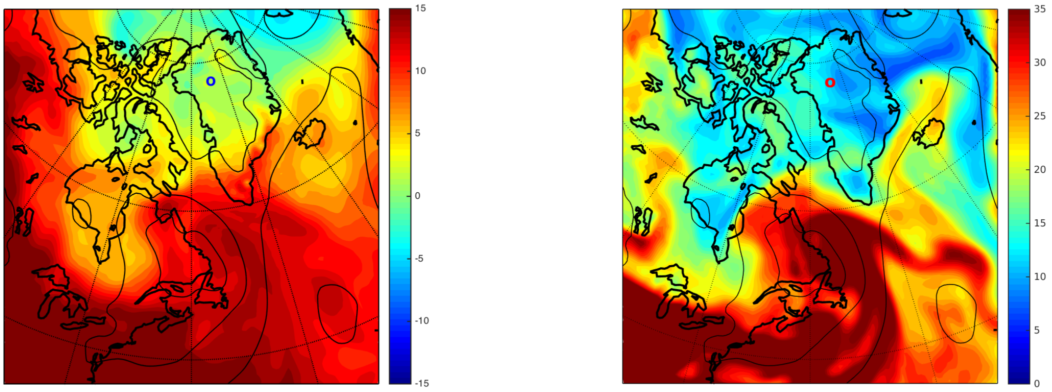

(e) Temperature on 08.07.12.

(f) Integrated water vapour on 08.07.12.

Figure 5.19: The temperature [°C] at 850 hPa (right panels) and the integrated water vapour [kg m^2] between 1000 and 500 hPa (left panels) for the period from 8 to 9 July 2012. The SLP contours are plotted for every 10 hPa. All the figures are at 00 h.

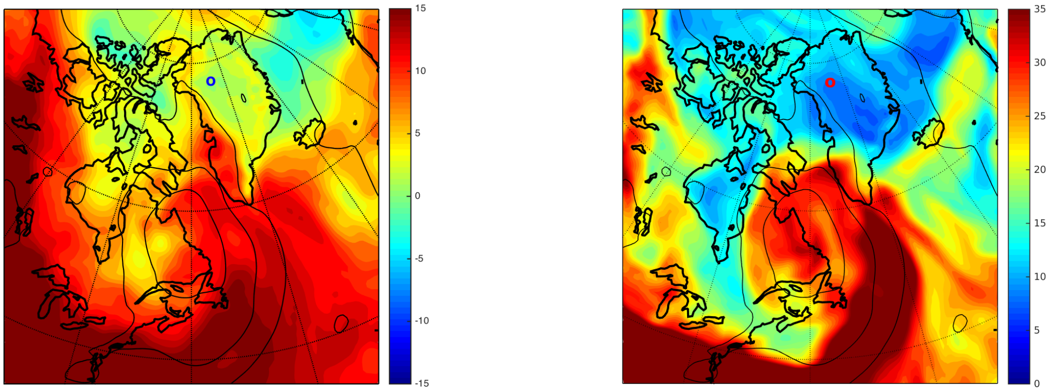

(a) Temperature on 09.07.12. (b) Integrated water vapour on 09.07.12.

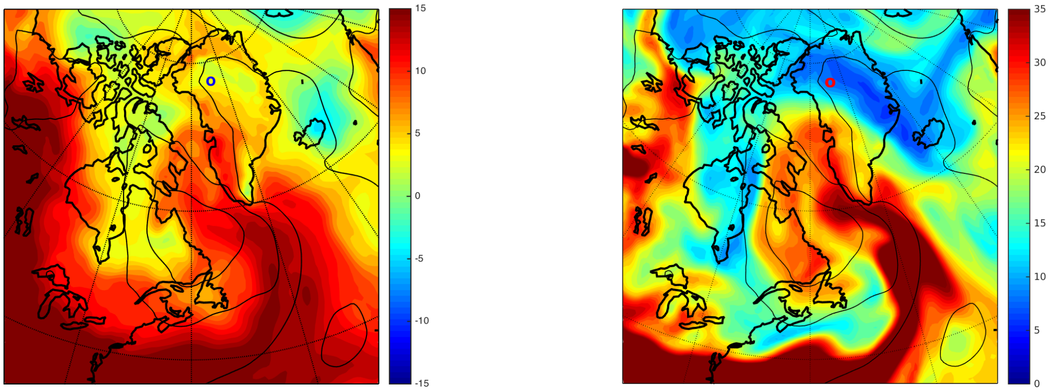

(c) Temperature on 10.07.12. (d) Integrated water vapour on 10.07.12.

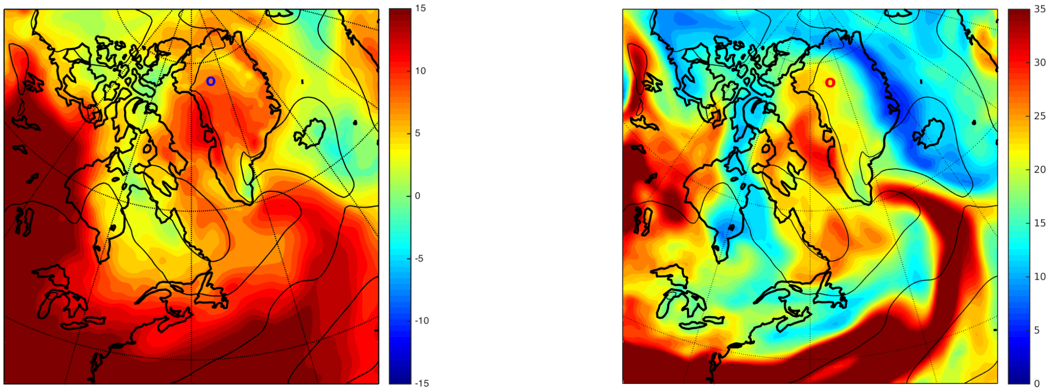

(e) Temperature on 11.07.12. (f) Integrated water vapour on 11.07.12.

Figure 5.20: The temperature [°C] at 850 hPa (right panels) and the integrated water vapour [kg m^2] between 1000 and 500 hPa (left panels) for the period from 10 to 11 July 2012. The SLP contours are plotted for every 10 hPa. All the figures are at 00 h.

5.3.2 16 June - 21 June 2010

The period from 16 to 21 June was chosen for its sudden peak in d-excess. The measurements from the period are shown in Figure 5.21. The days 18 and 19 June were characterized by a significant change in d-excess, and high values of temperature and humidity. In the following days the values returned to their earlier values, and 20 and 21 June were characterized by a decrease in d-excess, temperature and humidity.

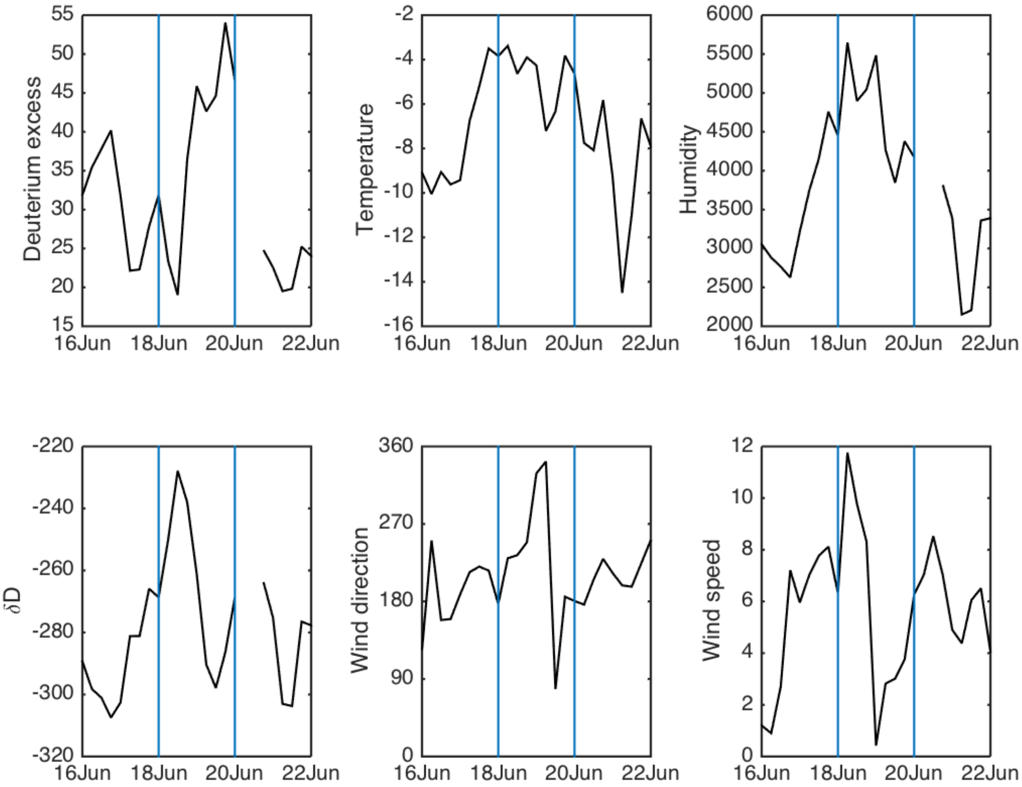

Figure 5.21: The measurements from NEEM for the period 16 June 00 h to 22 June 00 h, 2010. Showing the changes in d-excess [‰], temperature [°C], humidity [ppmv], δD [‰], wind direction [°] and speed [m s^{-1}]. The blue vertical line shows the chosen division of the period, 18.06.10 and 20.06.10

The changes in d-excess from 18 (12 h) to 19 (18 h) June, from a d-excess of 19‰ to 54.0‰, and the changes from 19 (18 h) to 21 (06 h) June, from a d-excess of 54.0‰ to 19.5‰ were two of the fastest changes of d-excess in the measurements.

The increase in d-excess was highly correlated with δD ($R^2 = 0.54$) and wind speed ($R^2 = 0.64$). The large change in d-excess was also exactly corresponding in time with the large decrease in wind speed. The decrease in d-excess was however highly correlated with temperature ($R^2 = 48$), humidity ($R^2 = 53$) and δD ($R^2 = 30$).

The Lagrangian moisture source diagnostic have been run to investigating the origin of moisture for the period. A time series of the data is shown in Figure 5.22, and the trajectories and moisture uptake are illustrated in Figure 5.23 and 5.24.

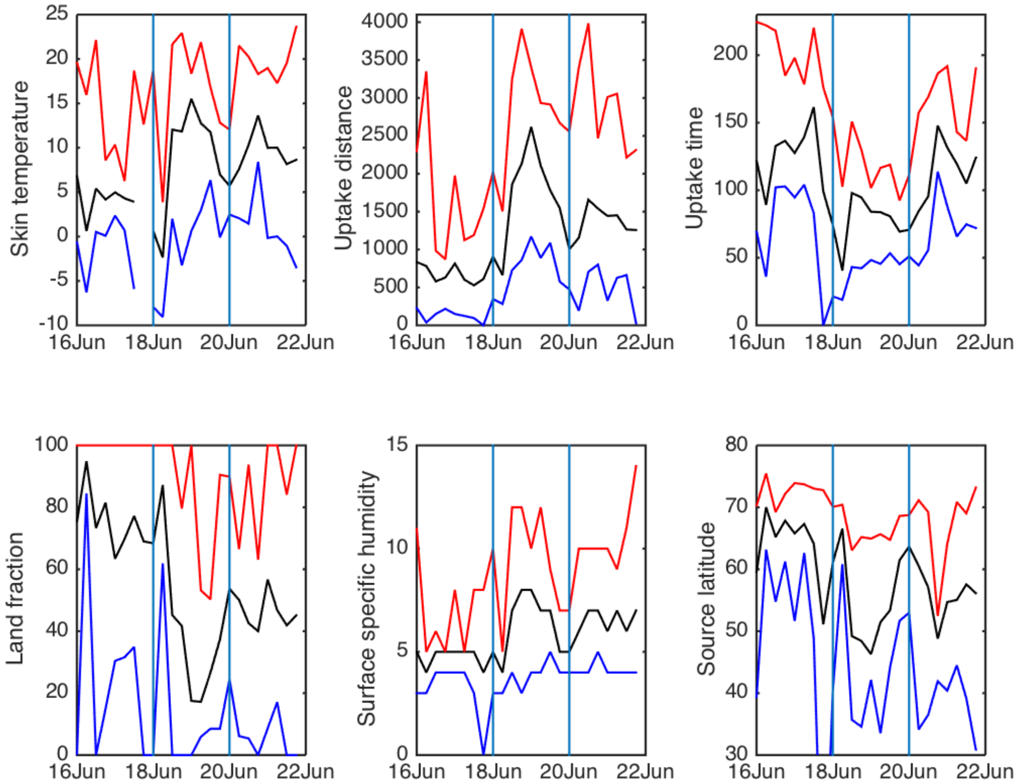

Figure 5.22: Time series of the moisture source properties for the period from 13 to 22 June 2010, showing the skin temperature [°C], uptake distance [km], uptake time [h], land fraction [%], surface specific humidity [g kg^{-1}] and source latitude [°N]. The black curve shows the average, the red the maximum and the blue the minimum values of the moisture source arriving at a given time (every 6 h).

From the moisture uptake from 17 and 18 June shown in Figure 5.23b and d, we saw a clear shift in the uptake. At the time of the peak in d-excess, from 18 to 19 June, the moisture uptake showed a small change. The 18 June, shown in Figure 5.23d, had its strongest uptake from the south of Greenland. 19 June, shown in Figure 5.24b, had a much larger extension in the moisture uptake, with its strongest uptake both from the south of Greenland and from the North Atlantic Ocean.

Figure 5.22 of the average values of what is reaching NEEM is also showing clear changes, the skin temperature, uptake distance and surface specific humidity had increased

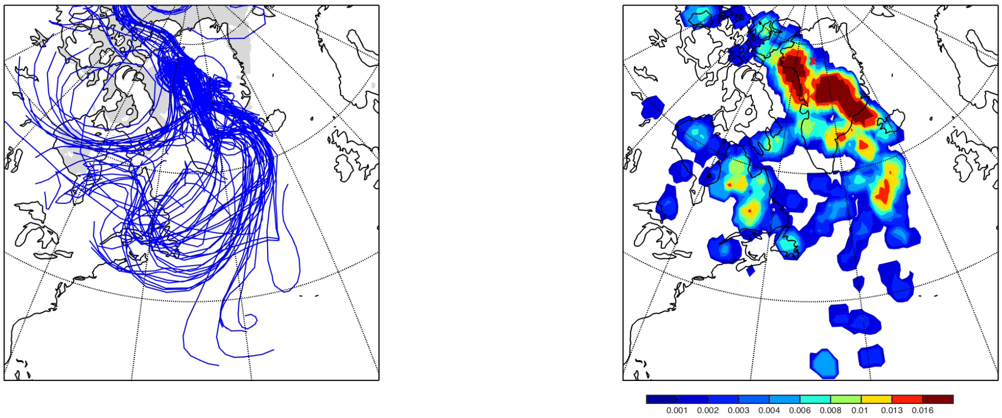

(a) Trajectories for 17.06.10.

(b) Uptake for 17.06.10.

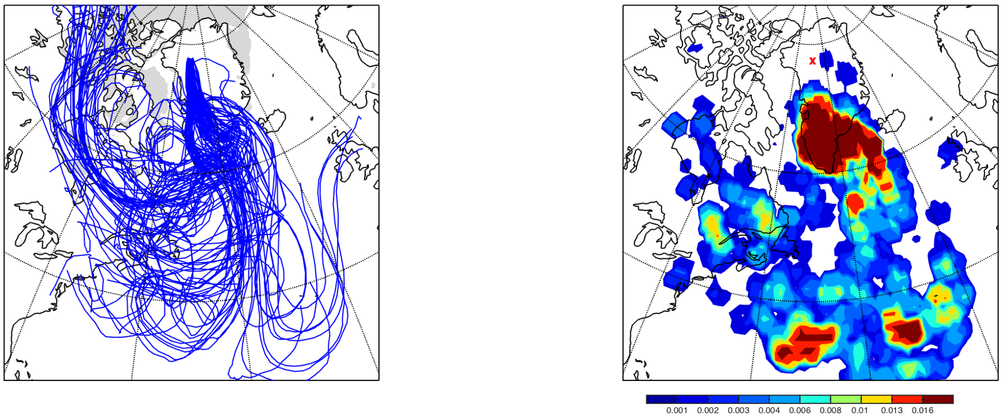

(c) Trajectories for 18.06.10.

(d) Uptake for 18.06.10.

Figure 5.23: The moisture source for water vapour identified with a 10-days back trajectory for 17 to 18 June 2010. The right panels shows the path of the water vapour (blue line). The grey area indicates where the sea ice concentration exceeds 50%. The left panels shows the location of the moisture uptake (in mm $6h^{-1}$).

and the uptake time, land fraction and source latitude had decreased. D-excess had a high correlation with land fraction ($R^2 = 0.39$) and source longitude ($R^2 = 0.46$), from 18 to 20 June.

Temperature and integrated water vapour for the period are shown in Figure 5.25 and 5.26. The start of the period was characterized by cool and dry air. On 19 July, shown in Figure 5.26b, the remains of an atmospheric river was hitting NEEM and gave more humid and warm air. After 20 June, the temperature and humidity decreased back to their initial values.

From Figure 5.24b and the increase in uptake distance and source latitude, and reduction in land fraction, the moisture reaching NEEM 19 June seems to be dominated by

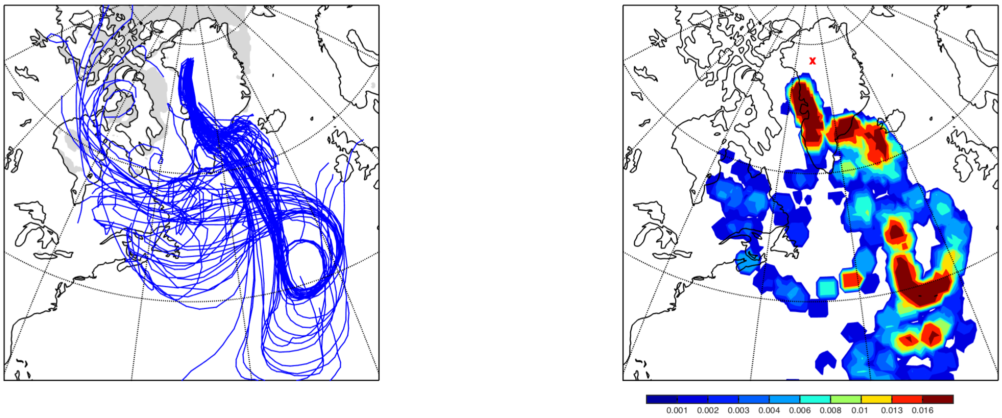

(a) Trajectories for 19.06.10.

(b) Uptake for 19.06.10.

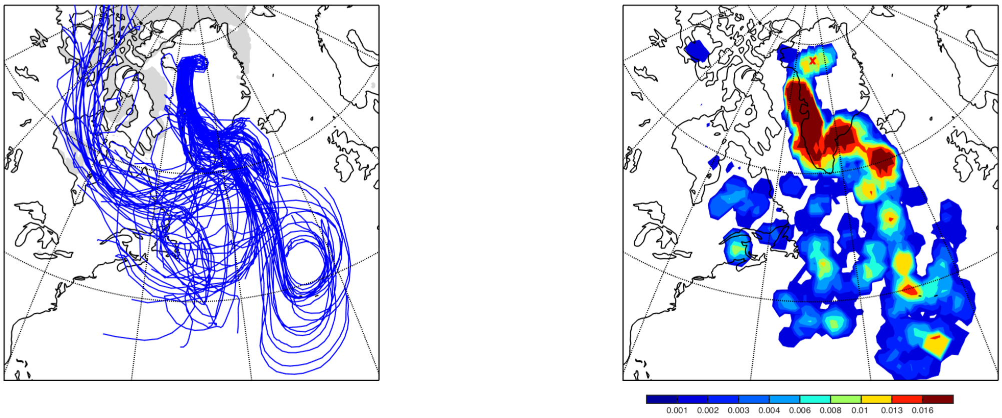

(c) Trajectories for 20.06.10.

(d) Uptake for 20.06.10.

Figure 5.24: The moisture source for water vapour identified with a 10-days back trajectory for 19 and 20 June 2010. The right panels shows the path of the water vapour (blue line). The grey area indicates where the sea ice concentration exceeds 50%. The left panels shows the location of the moisture uptake (in mm 6h^{-1}).

moisture from the subtropical North Atlantic Ocean. From the clear increase in the uptake distance and decrease in the uptake time, the water vapour must have had a much higher velocity than normal. An uptake from the subtropical North Atlantic Ocean is, however, likely to have a much lower d-excess, than what was observed here and the d-excess signal is likely not from the evaporation location, and may have been shifted on its way to NEEM.

The clear change in d-excess corresponded exactly in time with the very low windspeed. The low windspeed and the maximum land fraction being high, could mean that the moisture had been affected by the moisture taken up at Greenland. Low windspeed could also give higher ability for moisture uptake.

From Figure 5.24b, we can see that the moisture uptake was also high over the south

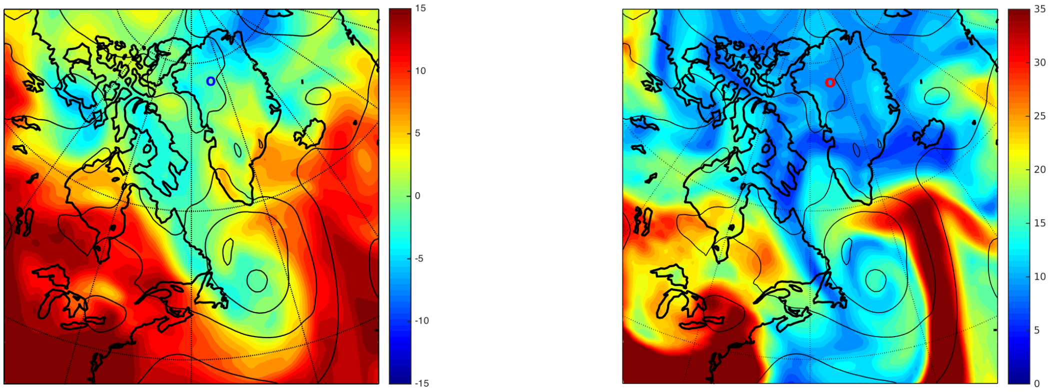

(a) Temperature on 17.06.10.

(b) Integrated water vapour on 17.06.10.

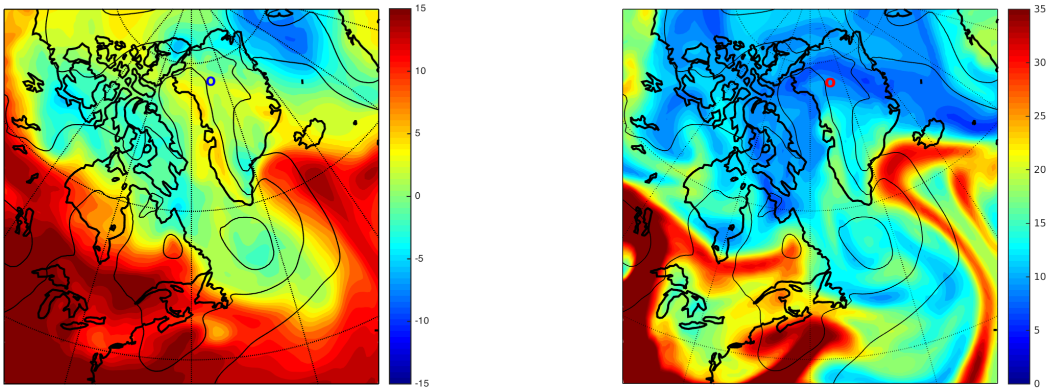

(c) Temperature on 18.06.10.

(d) Integrated water vapour on 18.06.10.

Figure 5.25: The temperature [°C] at 850 hPa (right panels) and the integrated water vapour [kg m^2] between 1000 to 500 hPa (left panels) for the period from 17 to 18 June 2010. The SLP contours are plotted every 10 hPa. All the figures are at 00 h.

of Greenland. Uptake from Greenland, where the air is very dry, gives high probability of kinetic fractionation, leading to a depleted signal in δD and a high d-excess.

5.3.3 25 June - 3 July 2010

The measurements from 25 June to 3 July are displayed in Figure 5.27. From 28 June to 1 July we saw a big change in d-excess from 30.2‰ to 59.4‰, associated with a temperature decrease from -6.3°C to -19.2°C and humidity decrease from 4182.4 ppmv to 1792.7 ppmv. A d-excess of 59.4‰ is the highest recorded d-excess of the measurements. The d-excess quickly returned to its originally value after 1 July.

The measurements of temperature and humidity were characterized by a lot of fluctua-

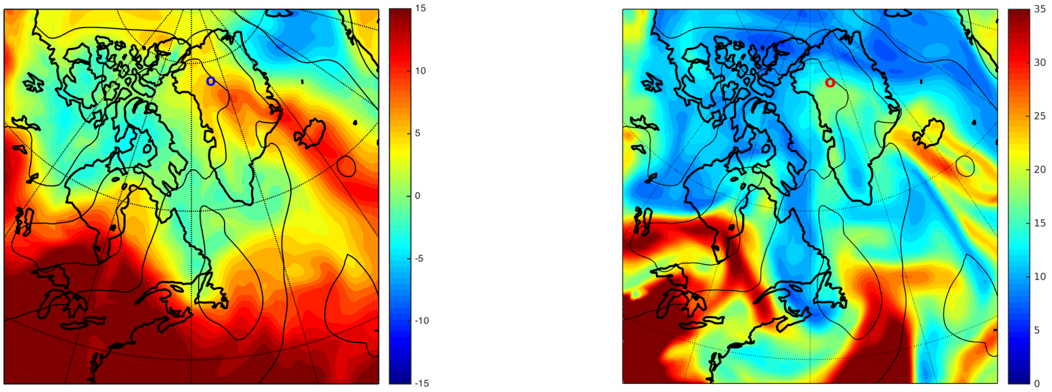

(a) Temperature on 19.06.10. (b) Integrated water vapour on 19.06.10.

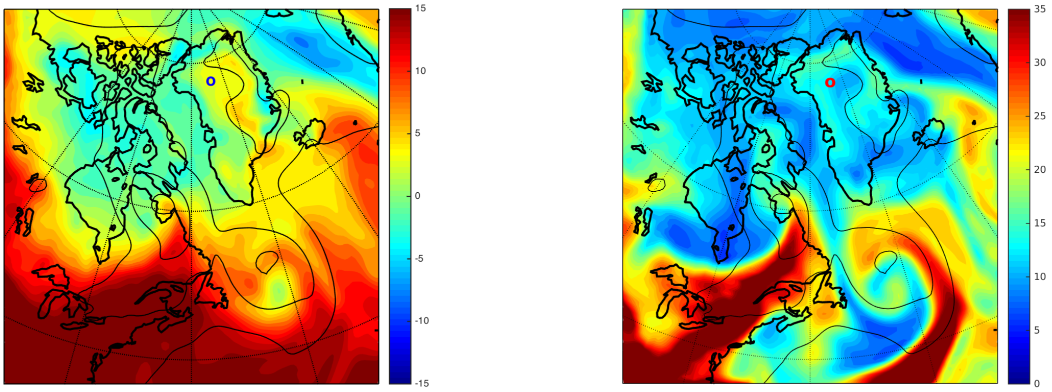

(c) Temperature on 20.06.10. (d) Integrated water vapour on 20.06.10.

Figure 5.26: The temperature [°C] at 850 hPa (right panels) and the integrated water vapour [kg m^2] between 1000 to 500 hPa (left panels) for the period from 19 to 20 June 2010. The SLP contours are plotted every 10 hPa. All the figures are at 00 h.

tions, and the correlation with d-excess was zero. D-excess and δD had a smaller correlation ($R^2 = 0.27$), and change oppositely. The wind speed also had its lowest value with the biggest change in d-excess, the correlation was however poor.

The origin of moisture found from Lagrangian moisture source diagnostic is shown as a time series in Figure 5.28, and the trajectories and uptake locations are illustrated in Figure 5.29 and 5.30.

The moisture uptake showed that the day containing the biggest change in d-excess, 27 and 28 June, shown in Figure 5.29b and d, had moisture uptake from higher latitudes. The following days, 29 and 30 June, shown in Figure 5.29f and 5.30b, had contributions from the south and west. The contribution from the west was moving over sea ice before reaching NEEM.

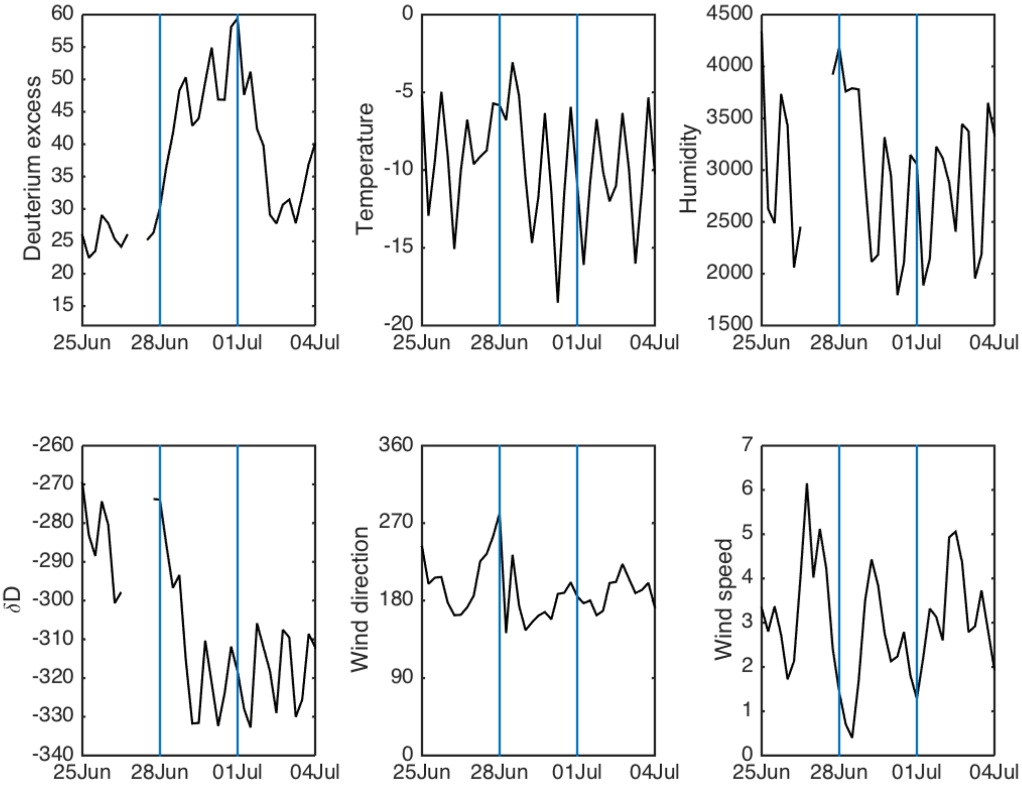

Figure 5.27: The measurements from NEEM for the period 25 June 00 h to 03 July 00 h, in 2010. Showing the changes in d-excess [‰], temperature [°C], humidity [ppmv], δD [‰], wind direction [°] and speed [m s^{-1}]. The blue vertical line shows the chosen division of the period, 28 June and 01 July.

From the time series of the moisture source shown in Figure 5.28, we can see clear changes in all the parameters at the two biggest increases in d-excess. The skin temperature clearly increased, the uptake distance and time shortened, land fraction clearly increased, surface specific humidity decreased and the location of the source latitude clearly decreased.

The correlation between d-excess and the result from the evaporation location, for the whole period was however very low. From 28 to 30 June, the highest correlation with d-excess was the land fraction ($R^2 = 0.10$) and source latitude ($R^2 = 0.09$). The correlation with the skin temperature ($R^2 = 0.05$), surface specific humidity ($R^2 = 0.06$), uptake distance ($R^2 = 0.00$), uptake time ($R^2 = 0.02$) and source longitude ($R^2 = 0.00$) was poor.

The temperature and integrated water vapour plots are shown in Figure 5.31 and 5.32. The period was characterized by a low amount of integrated water vapour and colder temperatures. The cold temperatures and low integrated water vapour extended down to 50^o, where the warm moist air seemed trapped toward souther latitudes.

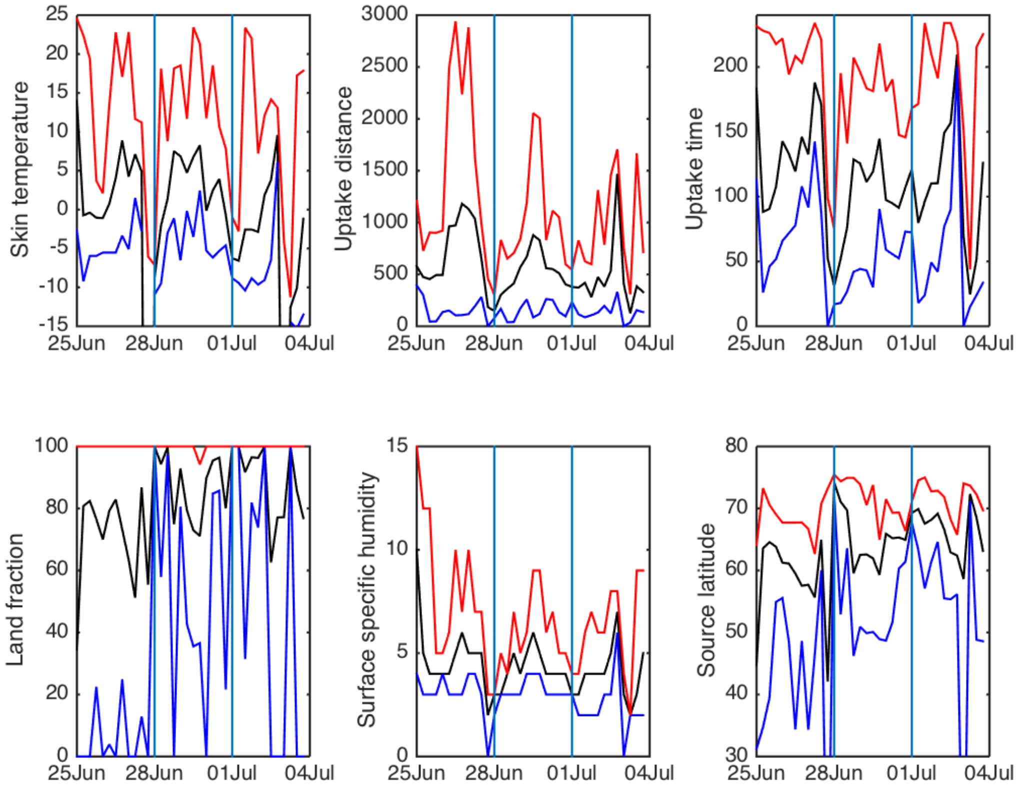

Figure 5.28: Time series of the moisture source properties for the period from 25 June to 4 July 2010, showing the skin temperature [°C], uptake distance [km], uptake time [h], land fraction [%], surface specific humidity [g kg^{-1}], and source latitude [°N]. The black curve shows the average, the red the maximum and the blue the minimum values of the moisture source arriving at a given time (every 6 h).

Uptakes from higher latitudes are characterized by a more depleted signal in δD, which could give higher d-excess values. Relative dry air with high temperature contrast between surface air temperature and sea surface temperature will typically have higher d-excess (Uemura *et al.*, 2008). The cold dry air from higher latitudes moves over open water, removing heat from the ocean surface, and getting a more depleted δD signal (Kurita, 2011).

Pfahl and Sodemann (2014) found a relationship between d-excess and relative humidity for moisture uptake over ocean. Following their Figure 1, an expansion of the figure to a d-excess of 60‰ will give a relative humidity close to 0, an abnormally small value. Our minimum surface specific humidity was equal to 0 g kg^{-1}. The land fraction was however relatively close to 100% (all uptake from land) at the time when the d-excess reached 59.4‰. This may suggest that the relationship is also applicable for uptake over land. The average specific humidity of 3 g kg^{-1} was however higher than what was predicted by Pfahl and Sodemann (2014).

The markedly change in d-excess was also corresponding exactly in time with the very low windspeed, meaning that the moisture could have been affected by the cold underlying snow, which also could have played a part in the increased d-excess value.

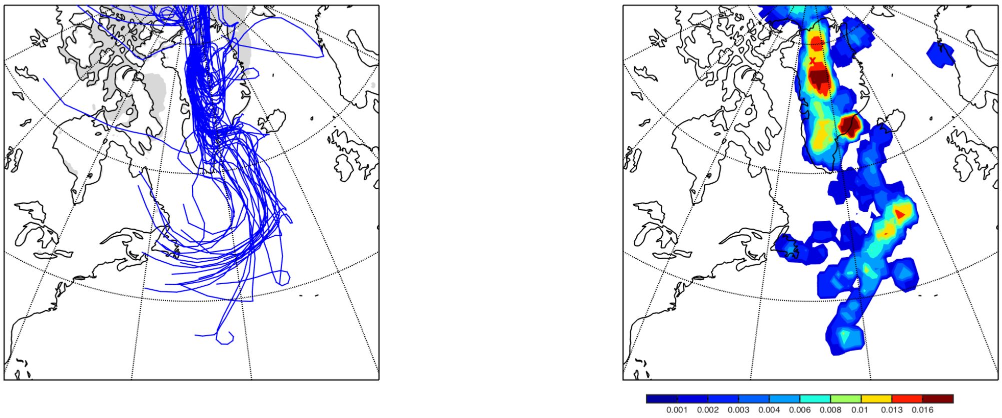

(a) Modelled trajectories for 27.06.10. (b) The uptake for 27.06.10.

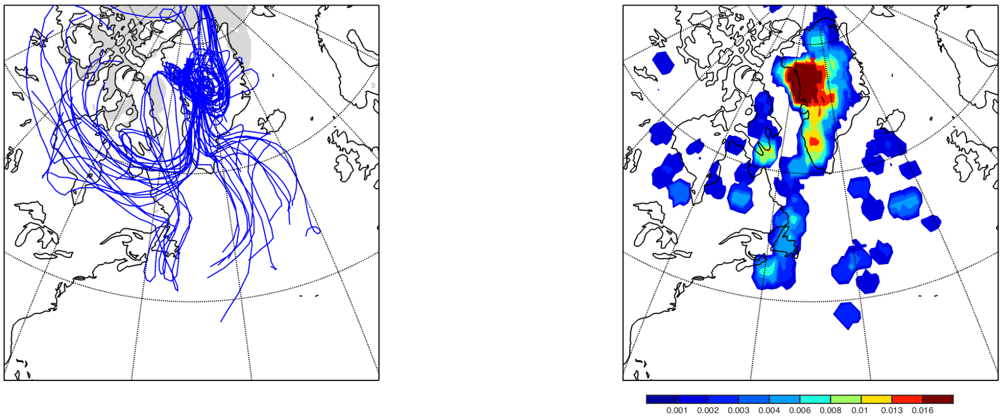

(c) Modelled trajectories for 28.06.10. (d) The uptake for 28.06.10.

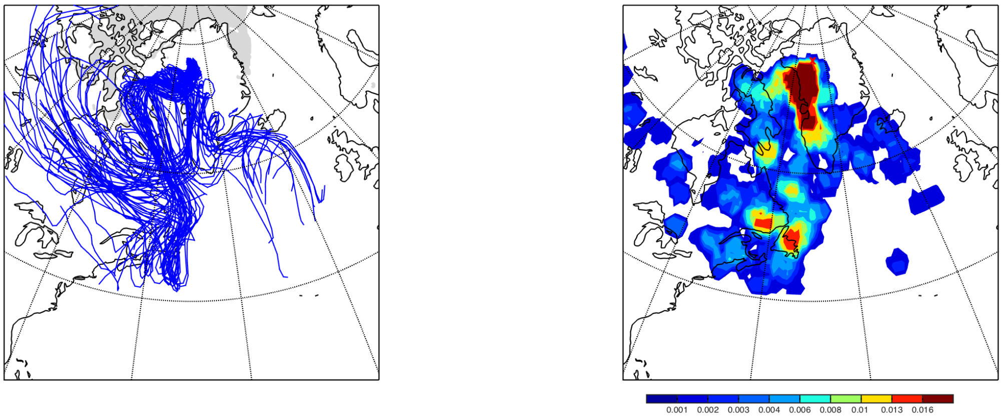

(e) Modelled trajectories for 29.06.10. (f) The uptake for 29.06.10.

Figure 5.29: The moisture source for water vapour identified with a 10-days back trajectory for 27 to 29 June 2010. The right panels shows the path of the water vapour (blue line). The grey area indicate where the sea ice concentration exceeds 50%. The left panels shows the moisture uptake (in mm $6h^{-1}$).

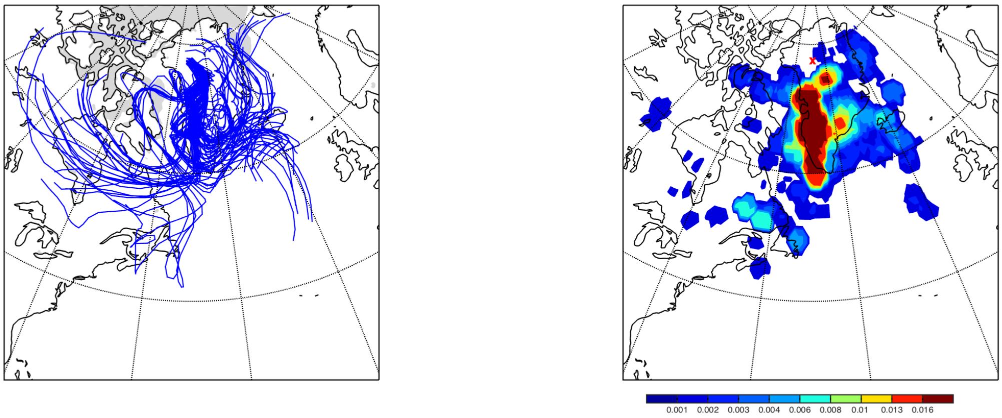

(a) Modelled trajectories for 30.06.10.

(b) The uptake for 30.06.10.

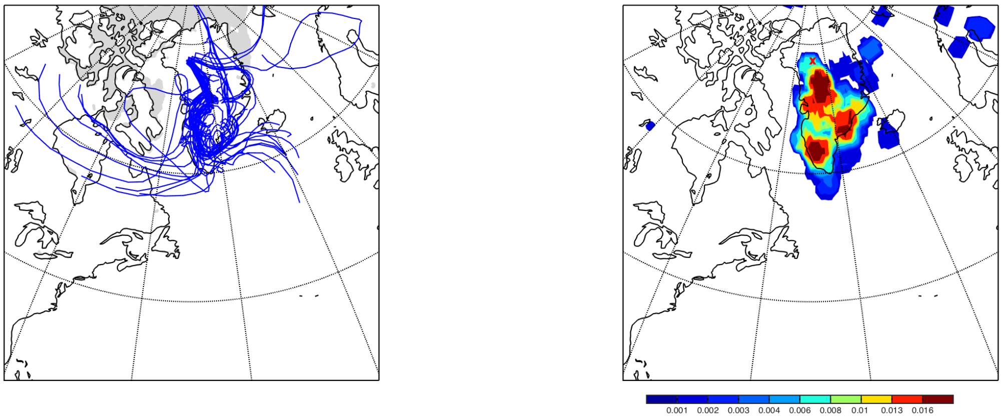

(c) Modelled trajectories for 01.07.10.

(d) The uptake for 01.07.10.

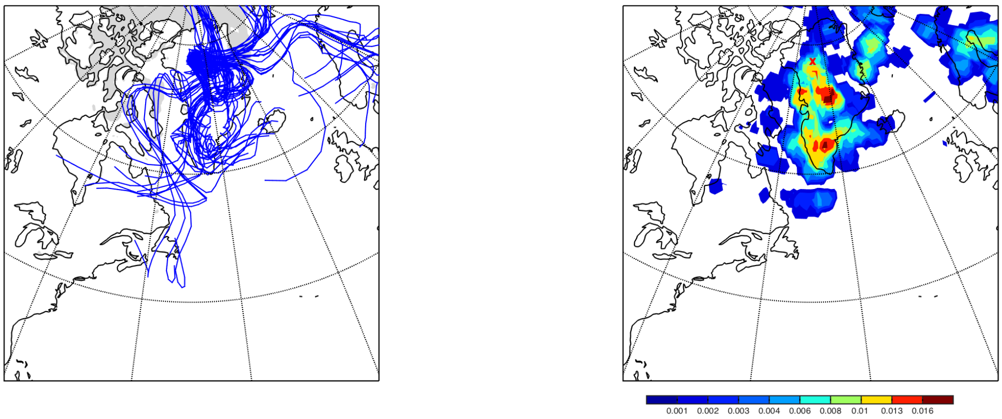

(e) Modelled trajectories for 02.07.10.

(f) The uptake for 02.07.10.

Figure 5.30: The moisture source for water vapour identified with a 10-days back trajectory for 30 June to 2 July 2010. The right panels shows the path of the water vapour (blue line). The grey area indicate where the sea ice concentration exceeds 50%. The left panels shows the moisture uptake (in mm $6h^{-1}$).

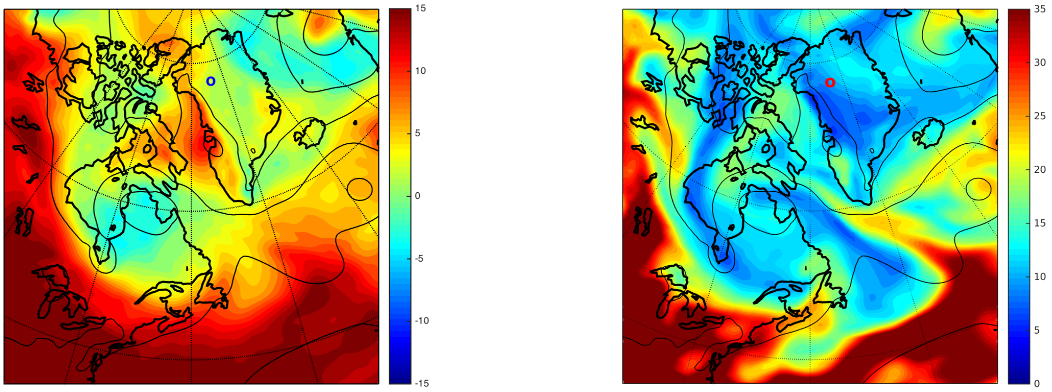

(a) Temperature on 27.06.10. (b) Integrated water vapour on 27.06.10.

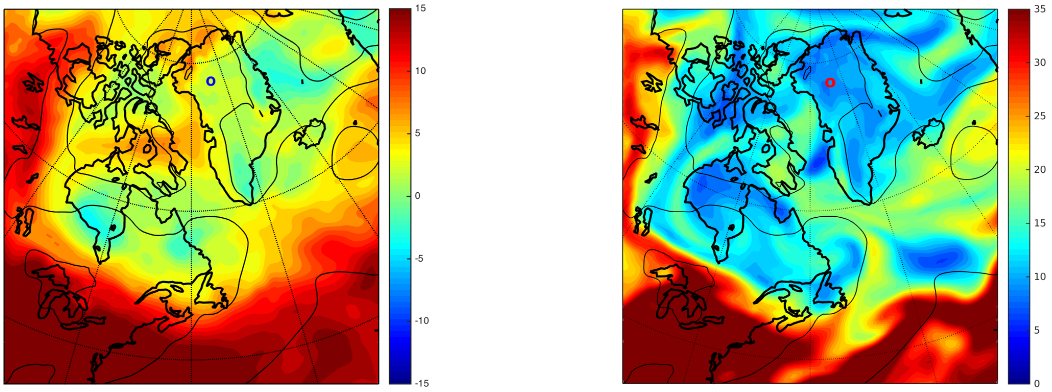

(c) Temperature on 28.06.10. (d) Integrated water vapour on 28.06.10.

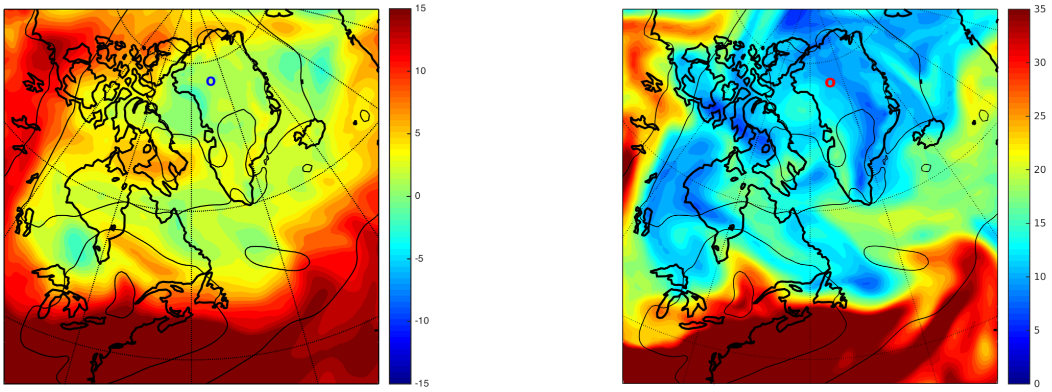

(e) Temperature on 29.06.10. (f) Integrated water vapour on 29.06.10.

Figure 5.31: The temperature [°C] at 850 hPa (right panels) and the integrated water vapour [kg m^2] between 1000 and 500 hPa (left panels) for the period from 27 to 29 June 2010. The SLP contours are plotted every 10 hPa. All the figures are at 00 h.

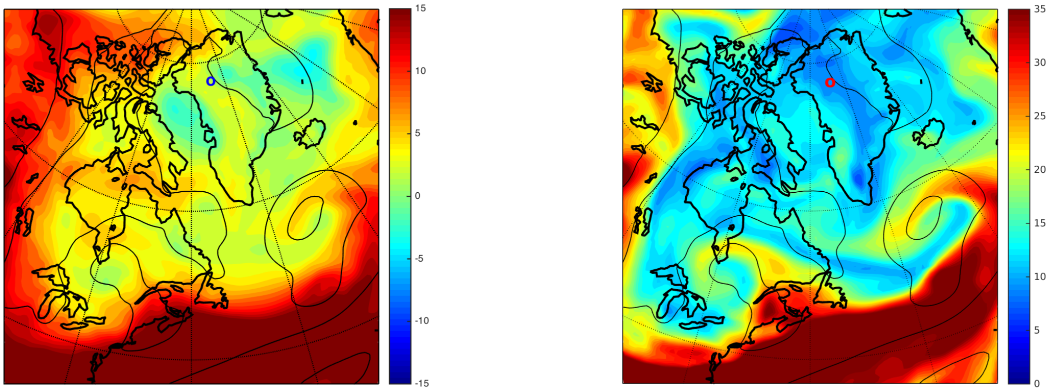

(a) Temperature on 30.06.10.

(b) Integrated water vapour on 30.06.10.

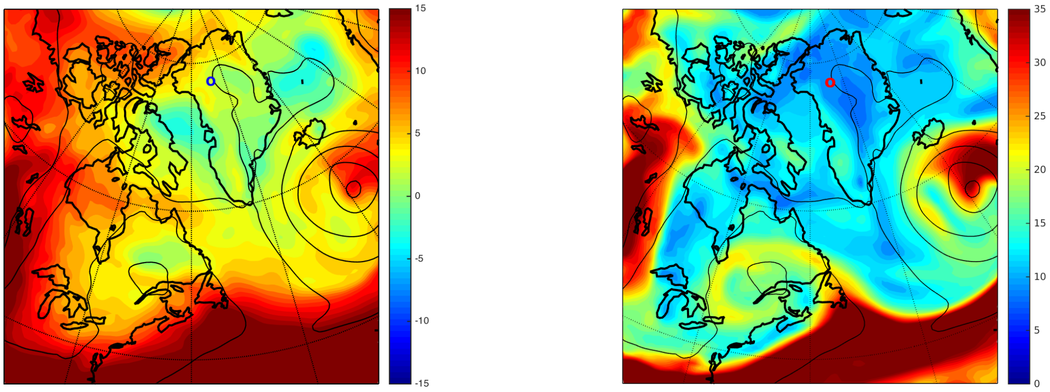

(c) Temperature on 01.07.10.

(d) Integrated water vapour on 01.07.10.

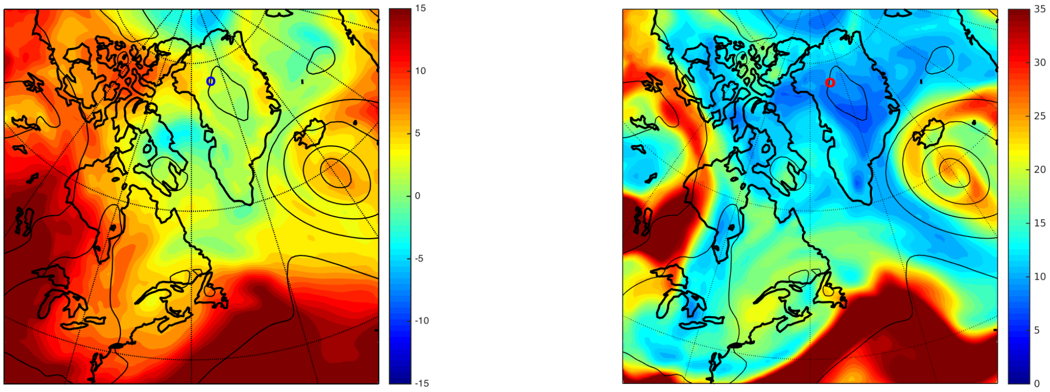

(e) Temperature on 02.07.10.

(f) Integrated water vapour on 02.07.10.

Figure 5.32: The temperature [°C] at 850 hPa (left panels) and the integrated water vapour [kg m^2] between 1000 and 500 hPa (left panels) for the period from 30 June to 02 July 2010. The SLP contours are plotted every 10 hPa. All the figures are at 00 h.

Chapter 6

Discussion and conclusion

This section summarizes our findings on the Arctic moisture uptake, through studying the moisture source to NEEM and Tustervatn and their stable isotopes. With the use of a Lagrangian moisture source diagnostic, we have estimated the moisture source and compared it with observations of the stable isotopes.

The moisture sources of NEEM and Tustervatn are largely separate and show clear differences in the uptake from an inland location to a location near the coast, but they also show some distinct similarities. NEEM had an average uptake of 410 mm/month, while Tustervatn had an average of 2830 mm/month. Both NEEM and Tustervatn showed an increase in the moisture uptake from winter to summer. The moisture to NEEM had contributions from Greenland, the north of America and the ocean areas from the Norwegian Sea to the North Atlantic Ocean. Tustervatn had most of its moisture uptake from Norway and the oceans from the Norwegian Sea to the North Atlantic Ocean. Notably was the high moisture uptake at the remains of the Gulf Stream in the North Atlantic Ocean.

Both NEEM and Tustervatn showed a shift in the moisture uptake from local uptake in the winter to moisture transport from lower latitudes in the summer, which is consistent with findings from Kurita (2011) of a shift in the moisture uptake to the Arctic.

The two study sites showed agreement in the seasonal cycle of land fraction, skin temperature, uptake distance and source latitude, but differed in value.

From our comparison of the measurements with the moisture source diagnostic, we demonstrate that d-excess is highly correlated with latitude. D-excess increase when the moisture source is predominantly from Arctic sites, and decrease when the moisture source is from subtropical origin. This is consistent with findings from Kurita (2011) and Steen-Larsen *et al.* (2013). Our comparison also displayed some clear dependencies for d-excess, most markedly were the dependency with land fraction, skin temperature, surface specific humidity and source latitude.

The case studies from NEEM support the hypothesis that d-excess is related to the moisture origin (Jouzel *et al.*, 2013), and demonstrate the connection with moisture transport from the mid-latitude and Arctic region. Case studies from 2010 support the high probability of kinetic fractionation at higher latitudes, over a cold ocean surface.

The case studies from 2010 showed a clear dependence with the wind speed at the measurement site, the relationship is shown in Figure 6.1. The year 2010 was selected because of its higher d-excess. The correlation between d-excess and wind speed is however low, but it seems that the high value of d-excess corresponds with low wind speed. This could suggest that d-excess could be affected by the cold underlying surface.

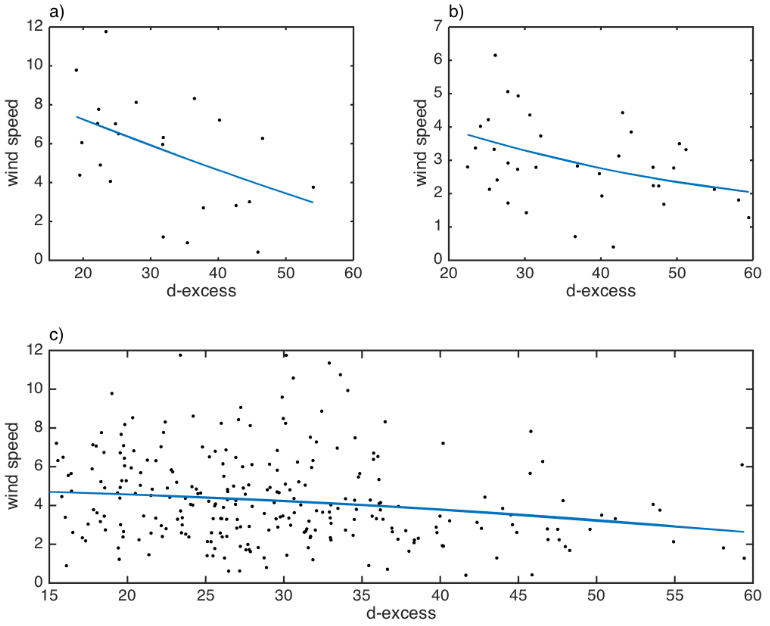

Figure 6.1: Relationship between d-excess [‰] and wind speed [m s^{-1}]. (a) Shows the case study from 16 to 21 June 2010. (b) The case study from 25 June to 3 July. (c) All the measurements from 2010. The blue line shows the linear trend.

One hypothesis of the connection between high d-excess and low wind speed is that the low windspeed give the isotopes the ability to penetrate into the snow (Steen-Larsen, 2015, pers. comm.), which will give high probability of kinetic fractionation. This is however not validated.

The stable isotopes, δ^{18}O and δD, are not expected to preserve the conditions from the evaporation site, and a dependency with the temperature and humidity at the measuring site is expected to be of more relevance. This is also the case for the δD measurements from NEEM, having a high correlation with the temperature and humidity. At Tustervatn, there were unfortunately only conducted measurements of δ^{18}O. The stable isotopes, δ^{18}O and δD, both showed a high dependency with the skin temperature and the surface specific humidity. The δD measurements also showed a high dependency with the source latitude. The higher dependencies for δ^{18}O and δD with temperature is in agreement with the temperature dependency from Dansgaard (1964). The higher dependency for δD than δ^{18}O is expected due to the equilibrium fractionation effect being around 10 times larger for δ^{18}O (Uemura *et al.*, 2008).

From meteorological maps of the moisture reaching Tustervatn (not shown) a high δ^{18}O corresponds with higher temperatures and integrated water vapour. This is consistent with our findings of a correlation with the skin temperature and surface specific humidity, and could also be the reason for the small dependency found with the source latitude.

The study can be considered as an approach to finding the mean condition of the moisture transport to NEEM in Greenland and Tustervatn in Norway. The Lagrangian moisture source diagnostic could however contain analysis errors, from uncertainties in the observations or in the data assimilation. The simplification in the precipitation and vapour estimate at the starting point, assuming to be given from Δq^0 for the last 6 hours, could give an increase in the moisture uptake. This will however not be of high importance for the drier interior of Greenland, but the more humid areas near the coast may give a positive bias. Trajectories going further backward than 10 days may lead to significant deviations from the actual movement of the air parcels (Stohl and Seibert, 1998). The relevant moisture uptakes are however assumed to take place in the first 3 to 7 days (Sodemann, 2006), and the uncertainty is also taken into account statistically by considering a large number of trajectories. Nevertheless, this thesis gives an indication of the most relevant moisture sources to the two Arctic sites and could give an idea of the seasonal cycles occurring at the Arctic.

Appendix A

Results from the Lagrangian moisture source diagnostic

A.1 Moisture source to NEEM

The moisture source from the Lagrangian moisture source diagnostic for each month in 2010 and 2011 is shown in Figure A.1 and A.2.

A.2 Moisture source to Tustervatn

The moisture source from the Lagrangian moisture source diagnsotic for each month in 1997, 1999 and 2003 is shown in Figure A.3 - A.5.

A.3 Annual trends

Time series of the moisture source properties for Tustervatn from the Lagrangian moisture source diagnostic, for the years from 1997 to 2000, is shown in Figure A.6 for land fraction and skin temperature, Figure A.7 for uptake distance and time, and Figure A.8 for source longitude and latitude.

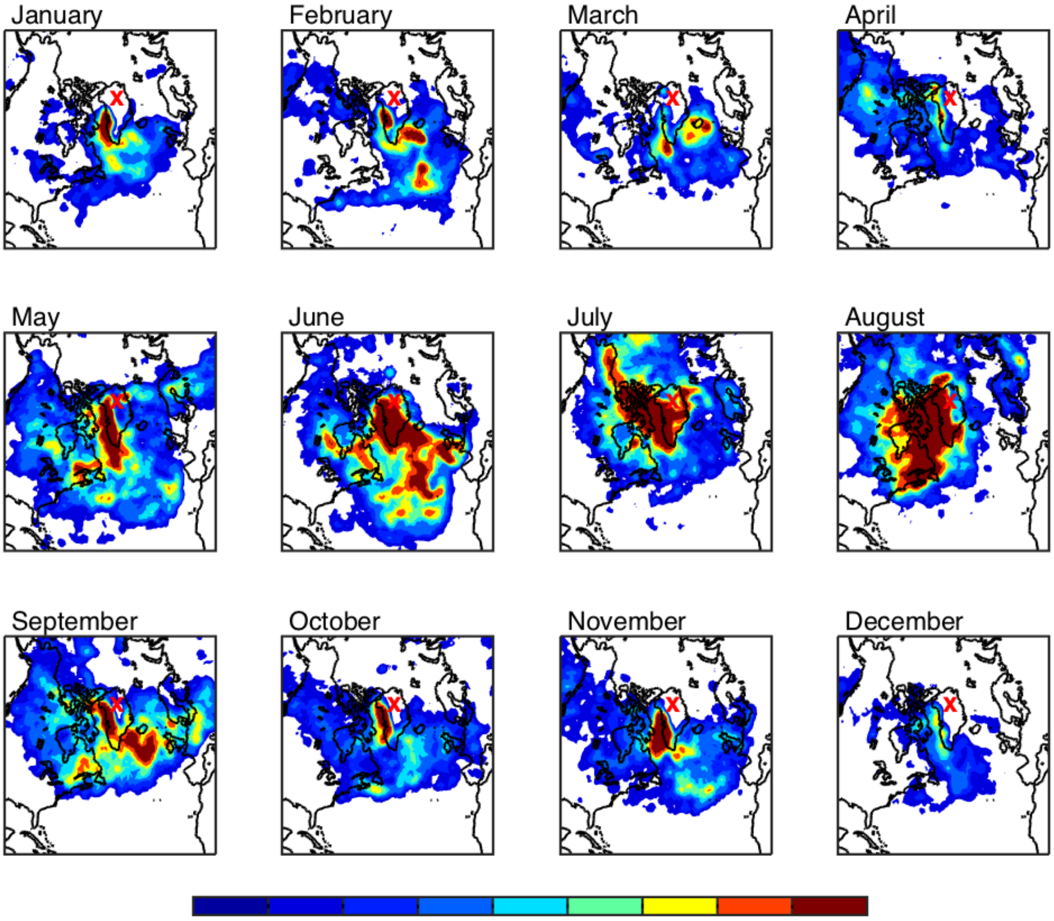

Figure A.1: The moisture source for water vapour at NEEM identified with a 20-days back trajectory for 2010, showing the location of the moisture uptake (in mm/month) for each month. The red cross shows the location of NEEM (77.45°N, 51.05°W.)

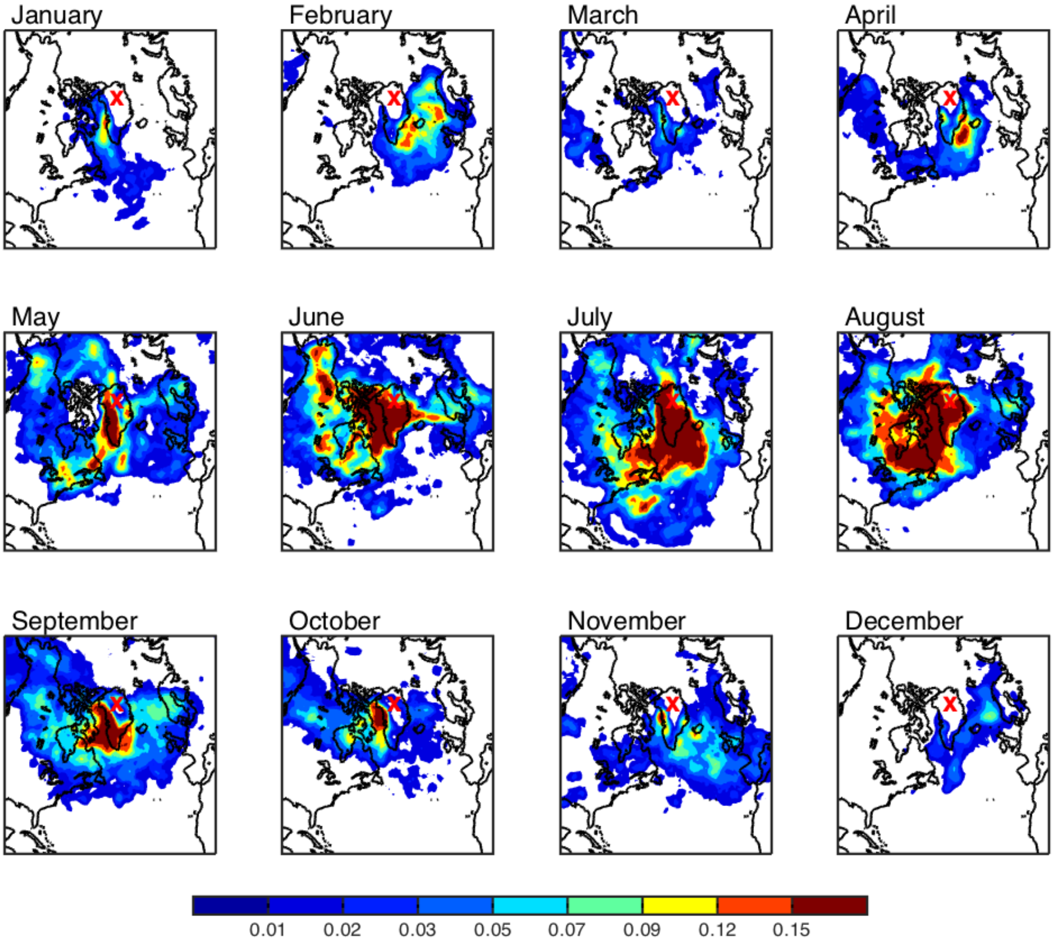

Figure A.2: The moisture source for water vapour at NEEM identify with a 20-days back trajectory for 2011, showing the location of the moisture uptake (in mm/month) for each month. The red cross shows the location of NEEM (77.45°N, 51.05°W).

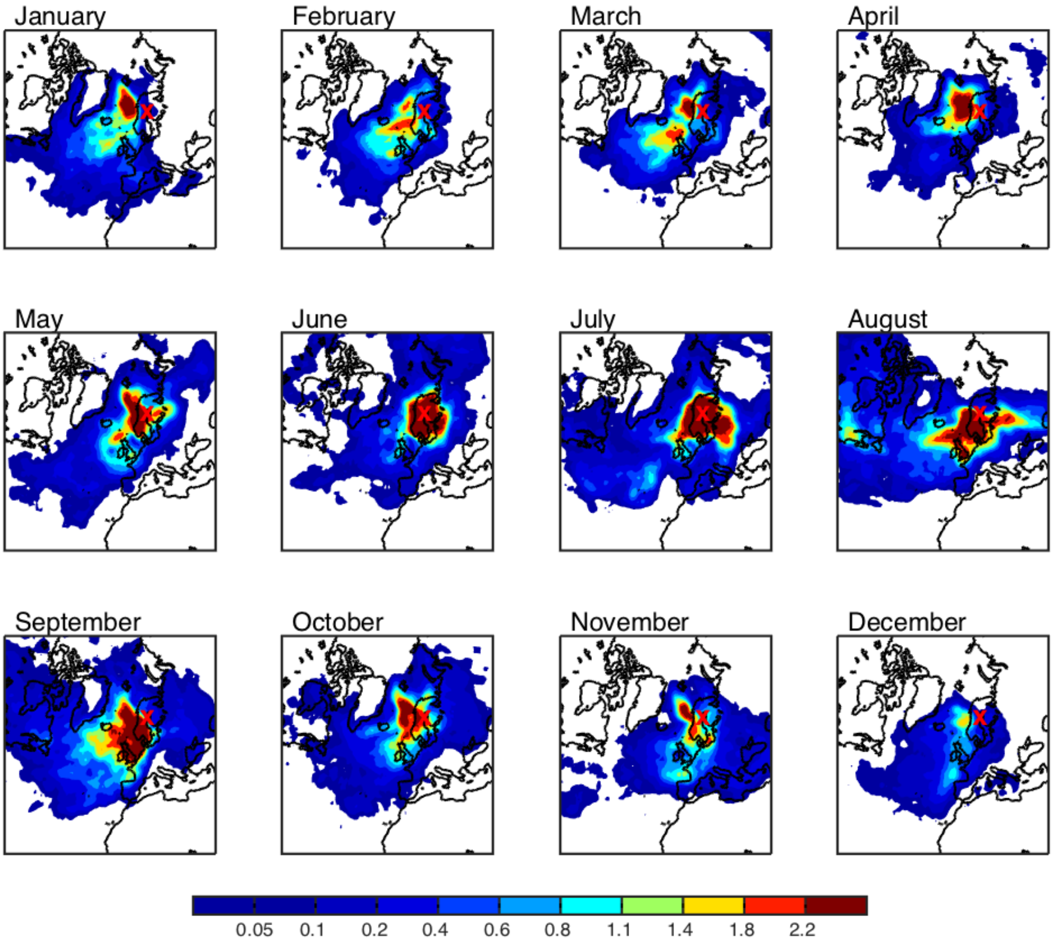

Figure A.3: The moisture source for water vapour at Tustervatn identify with a 20-days back trajectory for 1997, showing the location of the moisture uptake (in mm/month) for each month. The red cross shows the location of Tustervatn (65.83°N, 13.92°E).

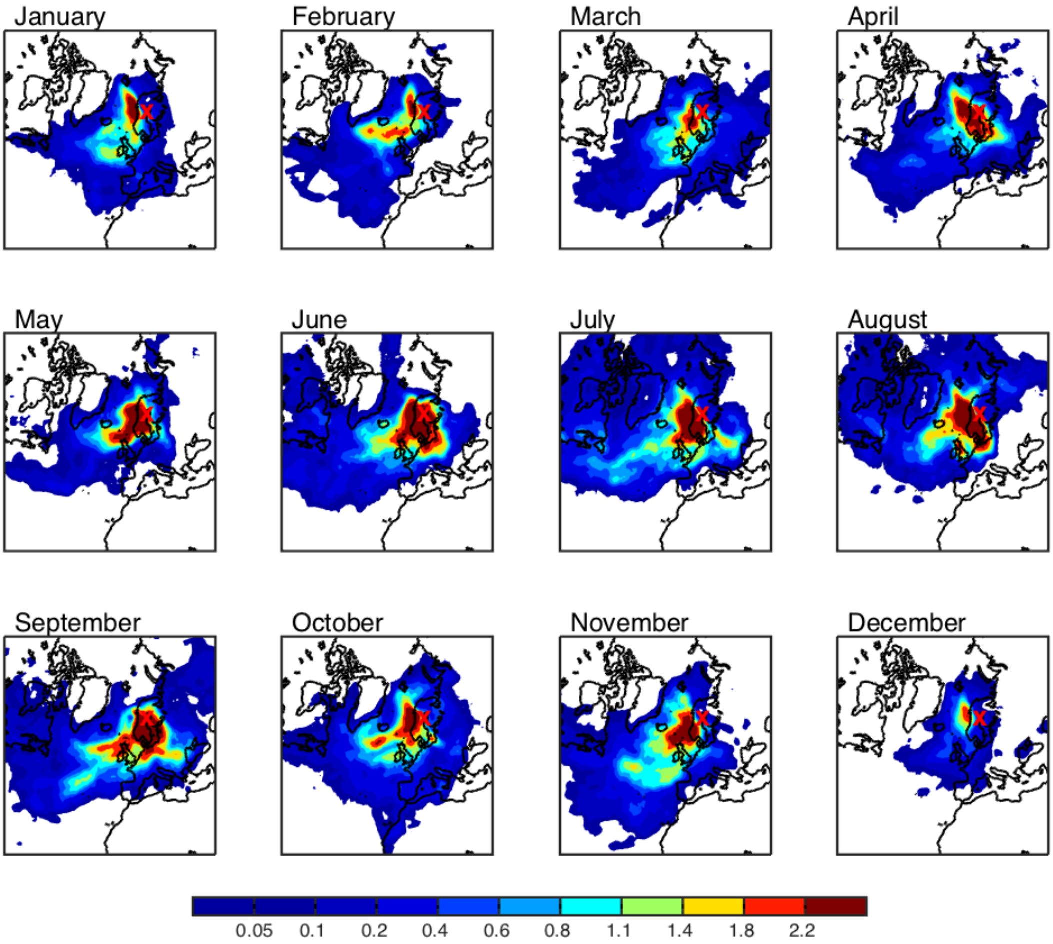

Figure A.4: The moisture source for water vapour at Tustervatn identify with a 20-days back trajectory for 1999, showing the location of the moisture uptake (in mm/month) for each month. The red cross shows the location of Tustervatn (65.83°N, 13.92 °E).

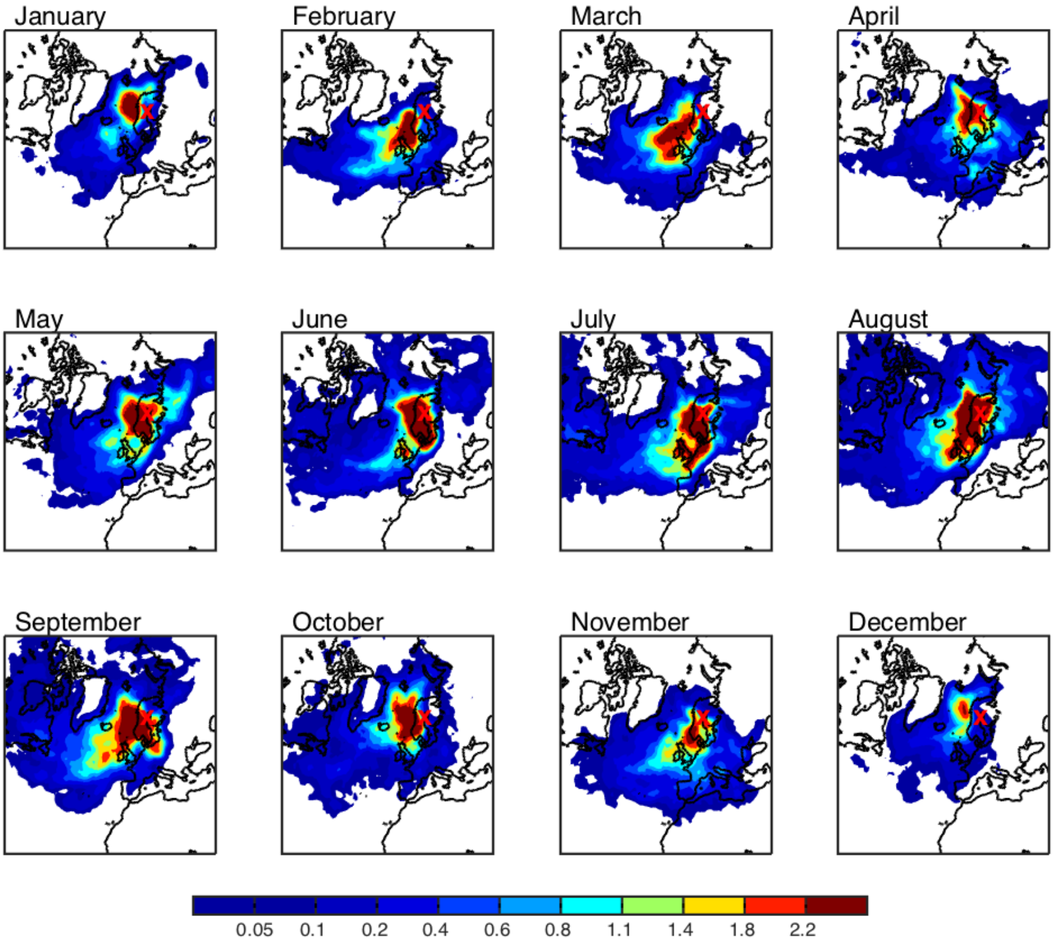

Figure A.5: The moisture source for water vapour at Tustervatn identify with a 20-days back trajectory for 2003, showing the location of the moisture uptake (in mm/month) for each month. The red cross shows the location of Tustervatn (65.83°N, 13.92°E).

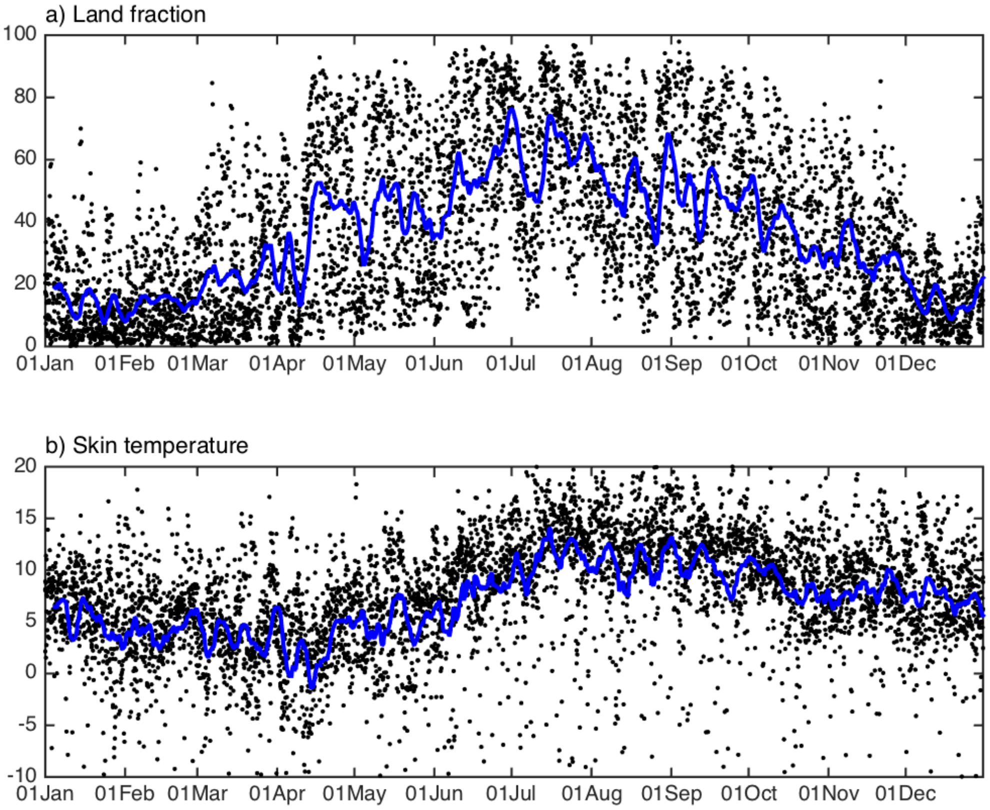

Figure A.6: Time series of the moisture source properties for the years from 1997 to 2000. (a) Land fraction [%] of the moisture uptake. (b) Skin temperature [°C] at the location of the moisture uptake. The black dots indicate an average of the moisture reaching Tustervatn every 6 hours. The blue line indicate the running mean.

a) Uptake distance

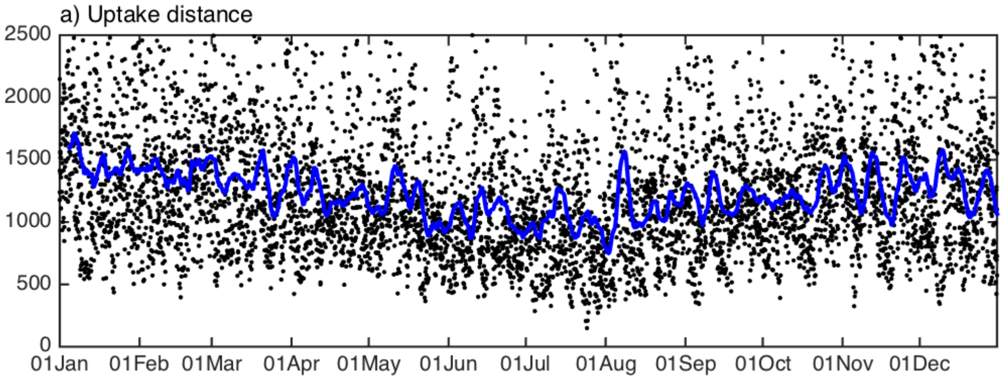

b) Uptake time

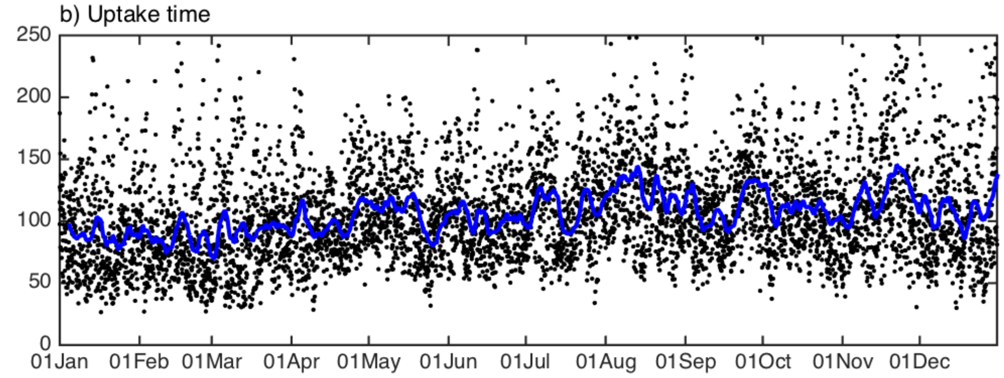

Figure A.7: Time series of the moisture source properties for the years from 1997 to 2000. (a) Uptake distance [km] for the moisture uptake. (b) Uptake time [h] for the moisture uptake. The black dots indicate an average of the moisture reaching Tustervatn every 6 hours. The blue line indicate the running mean.

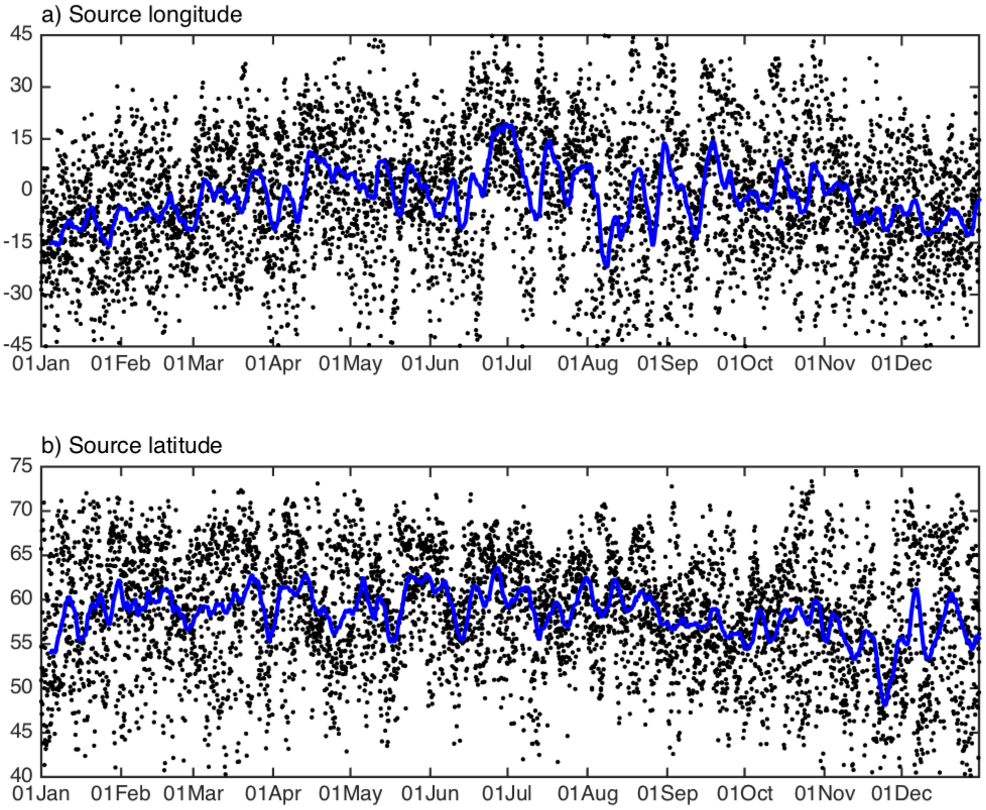

Figure A.8: Time series of the moisture source properties for the years from 1997 to 2000. (a) Source longitude of the moisture uptake [°]. (b) Source latitude of the moisture uptake [°]. The black dots indicate an average of the moisture reaching Tustervatn every 6 hours. The blue line indicate the running mean.

Appendix B

Comparison with the measurements

B.1 The summer field at NEEM

Data from the summer field campaign for 2010 and 2011 are illustrated in Figure B.1 and B.2. D-excess and $\delta^{18}O$, from our measurements, are shown in (a) and (b). The result from the Lagrangian moisture source diagnostic are shown in (c) to (i), illustrating the land fraction, skin temperature and surface specific humidity at the uptake location, uptake distance and time and the source longitude and latitude. The shaded periods are periods with high and low d-excess.

The average values of the periods shown in Figure B.1 and B.2, are displayed in Table B.1. The correlation between d-excess and δD with the variables from the Lagrangian moisture source diagnostic is shown in Table B.2.

Table B.1: The average values of d-excess [‰], δD [‰], land fraction [%], skin temperature [°C], surface specific humidity [g kg^{-1}] uptake distance [km], uptake time [h], source longitude [°W] and latitude [°N], for the period shown in Figure B.1, B.2, and 5.9, for 2010 to 2012.

	Red period: Low d-excess	Black period:	Blue period: High d-excess
D-excess	17.7 ± 3.5	25.3 ± 5.5	36.1 ± 8.7
δD	−253.5 ± 30.7	−287.1 ± 31.3	−311.7 ± 20.6
Land fraction	72.5 ± 18.6	76.8 ± 17.0	81.9 ± 11.1
Skin temperature	10.3 ± 14.6	10.1 ± 9.7	6.3 ± 9.0
Surface specific humidity	6.7 ± 2.1	6.4 ± 1.6	5.4 ± 1.2
Uptake distance	1298.7 ± 454.7	1266.0 ± 441.8	1044.0 ± 336.7
Uptake time	234.1 ± 59.5	209.5 ± 60.9	207.1 ± 52.9
Source longitude	50.6 ± 29.6	49.8 ± 38.2	43.9 ± 33.2
Source latitude	53.4 ± 6.8	57.9 ± 6.2	62.4 ± 4.0

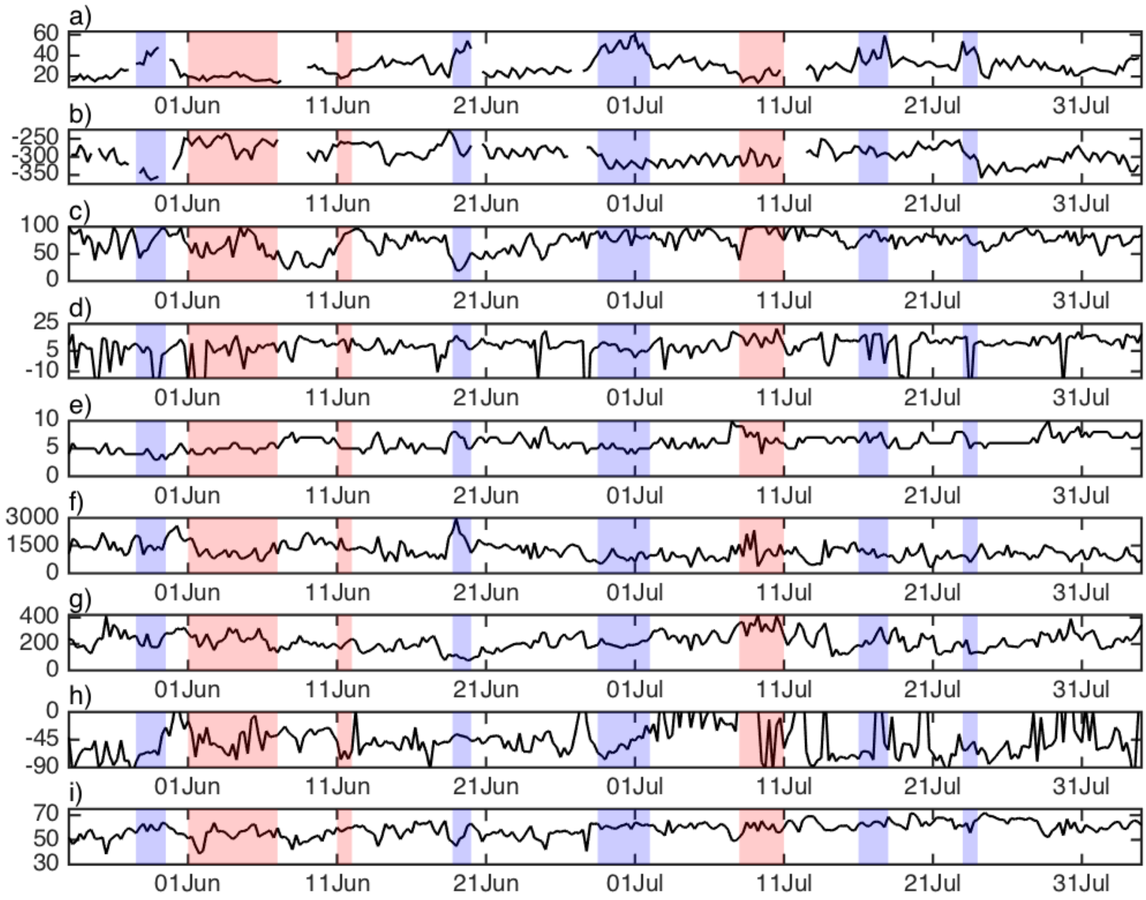

Figure B.1: Data from the summer field campaign at NEEM, from 24 May to 4 August 2010. (a) Shows the d-excess [‰], (b) δD [‰], (c) land fraction [%], (d) skin temperature [^oC], (e) surface specific humidity [g kg^{-1}], (f) uptake distance [km], (g) uptake time [h], (h) source longitude [^{o}] and (i) source latitude [^{o}]. The black curve shows the average of all the moisture reaching NEEM in an interval of 6 h. The blue and red shaded periods are periods with high and low d-excess.

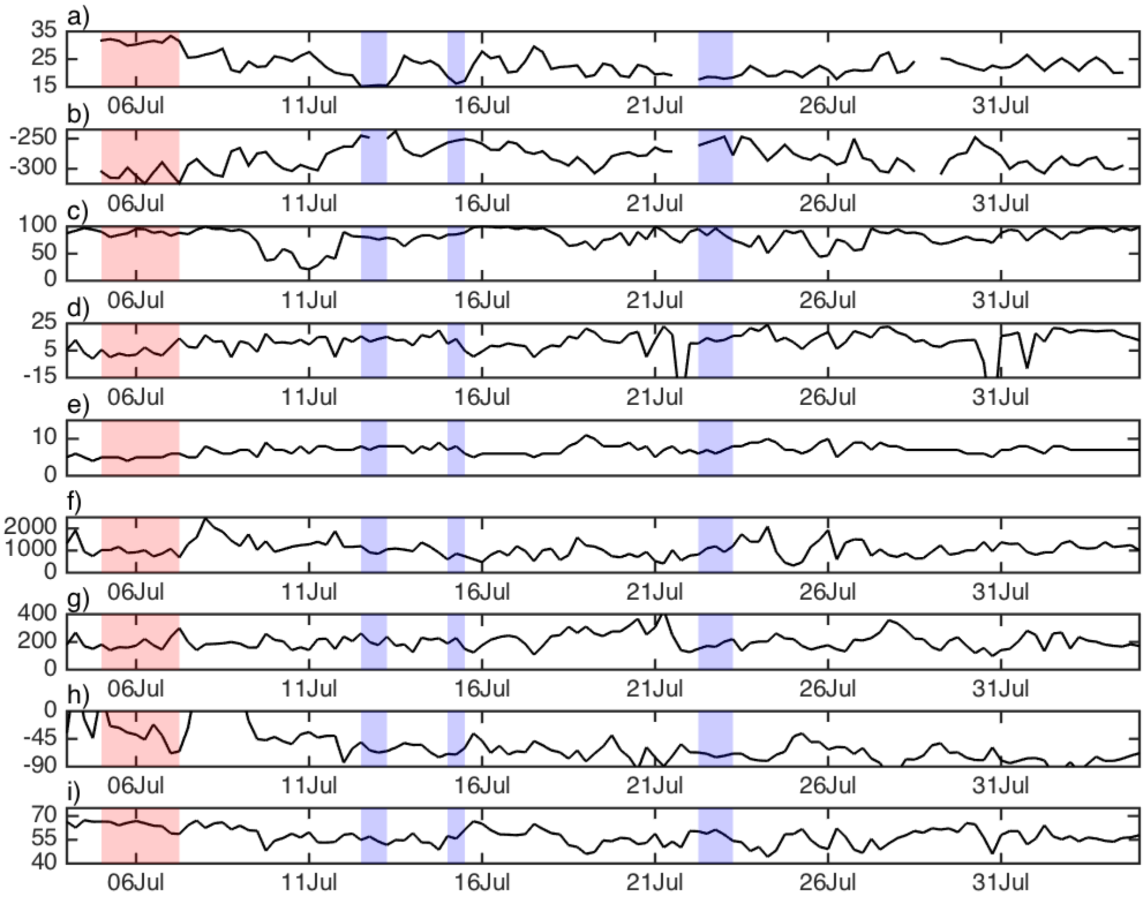

Figure B.2: Data from the summer field campaign at NEEM, from 4 July to 4 August 2011. (a) Shows the d-excess [‰], (b) δD [‰], (c) land fraction [%], (d) skin temperature [$^o C$], (e) surface specific humidity [g kg^{-1}], (f) uptake distance [km], (g) uptake time [h], (h) source longitude [^{o}] and (i) source latitude [^{o}]. The black curve shows the average of all the moisture reaching NEEM in an interval of 6 h. The blue and red shaded periods are periods with high and low d-excess.

Table B.2: Correlation for d-excess and δD, with the variables from the Lagrangian moisture source diagnostic for NEEM. From the data from 2010 to 2012.

	D-excess:		δD:	
	R	R^2	R	R^2
Land fraction	0.05	0.00	−0.09	0.01
Skin temperature	−0.13	0.02	0.17	0.03
Surface specific humidity	−0.27	0.07	0.43	0.18
Uptake distance	−0.15	0.02	0.09	0.01
Uptake time	−0.12	0.02	−0.06	0.00
Source longitude	0.09	0.01	−0.12	0.02
Source latitude	0.41	0.17	−0.44	0.20

B.2 δ^{18}O measurements from Tustervatn

The average values for the variables from the Lagrangian moisture source diagnostic, for the chosen division of δ^{18}O, is shown in Table B.3. The correlation between δ^{18}O and the variables from the Lagrangian moisture source diagnostic is shown in Table B.4.

Table B.3: The average values of δ^{18}O [‰], land fraction [%], skin temperature [°C], surface specific humidity [g kg^{-1}], precipitation estimate [mm $6h^{-1}$], uptake distance [km], uptake time [h], source longitude [°W] and latitude [°N], for the periods displayed. Data from 2002 to 2004.

	Red period: δ^{18}O < -19.0‰	Black period: -19.0 < δ^{18}O < -6.2‰	Blue period: δ^{18}O > -6.2‰
$\delta^{18}O$	-22.0 ± 2.4	-11.0 ± 3.1	-5.2 ± 0.8
Land fraction	27.6 ± 23.0	23.6 ± 23.7	10.8 ± 10.1
Skin temperature	6.8 ± 4.2	9.6 ± 4.4	10.5 ± 3.6
Surface specific humidity	4.3 ± 1.8	5.4 ± 2.2	5.2 ± 1.8
Precipitation estimate	0.05 ± 0.06	0.06 ± 0.06	0.06 ± 0.05
Uptake distance	1300.6 ± 736.9	1162.0 ± 555.5	1297.2 ± 520.5
Uptake time	79.0 ± 36.6	72.6 ± 34.4	73.1 ± 37.9
Source longitude	2.5 ± 18.4	-2.0 ± 16.1	-11.5 ± 13.1
Source latitude	58.3 ± 8.2	60.2 ± 7.1	58.5 ± 7.6

Table B.4: Correlation between δ^{18}O and the variables from the Lagrangian moisture source diagnostic for Tustervatn. From the data from 2002 to 2004.

	δ^{18}O:	
	R	R^2
Land fraction	-0.16	0.03
Skin temperature	0.28	0.08
Surface specific humidity	0.19	0.04
Precipition estimate	0.11	0.01
Uptake distance	0.03	0.00
Uptake time	0.00	0.00
Source longitude	-0.25	0.06
Source latitude	0.00	0.00

Bibliography

Benetti M, Reverdin G, Pierre C, Merlivat L, Risi C, Steen-Larsen HC, Vimeux F. 2014. Deuterium excess in marine water vapor: Dependency on relative humidity and surface wind speed during evaporation. *Journal of Geophysical Research-Atmospheres* **119**(2): 584–593, doi:10.1002/2013jd020535.

Bonne JL, Steen-Larsen HC, Risi C, Werner M, Sodemann H, Lacour JL, Fettweis X, Cesana G, Delmotte M, Cattani O, Vallelonga P, Kjaer HA, Clerbaux C, Sveinbjornsdottir AE, Masson-Delmotte V. 2015. The summer 2012 greenland heat wave: In situ and remote sensing observations of water vapor isotopic composition during an atmospheric river event. *Journal of Geophysical Research-Atmospheres* **120**(7): 2970–2989, doi:10.1002/2014jd022602.

Cappa CD, Hendricks MB, DePaolo DJ, Cohen RC. 2003. Isotopic fractionation of water during evaporation. *Journal of Geophysical Research-Atmospheres* **108**(D16), doi:10.1029/2003jd003597.

Christensen JH, Christensen OB. 2003. Climate modelling: Severe summertime flooding in europe. *Nature* **421**(6925): 805–806, doi:10.1038/421805a.

Dansgaard W. 1964. Stable isotopes in precipitation. *Tellus* **16**(4): 436–468.

Duetsch ML, Pfahl S, Sodemann H, Wernli H. 2013. Stable water isotope fractionation along trajectories. Master's thesis, Swiss Federal Institute of Technology Zurich.

Gat JR. 1996. Oxygen and hydrogen isotopes in the hydrologic cycle. *Annual Review of Earth and Planetary Sciences* **24**: 225–262, doi:10.1146/annurev.earth.24.1.225.

Jouzel J, Delaygue G, Landais A, Masson-Delmotte V, Risi C, Vimeux F. 2013. Water isotopes as tools to document oceanic sources of precipitation. *Water Resources Research* **49**(11): 7469–7486, doi:10.1002/2013wr013508.

Kurita N. 2011. Origin of arctic water vapor during the ice-growth season. *Geophysical Research Letters* **38**, doi:10.1029/2010gl046064.

Merlivat L, Jouzel J. 1979. Global climatic interpretation of the deuterium-oxygen-18 relationship for precipitation. *Journal of Geophysical Research-Oceans and Atmospheres* **84**(NC8): 5029–5033, doi:10.1029/JC084iC08p05029.

Neff W, Compo GP, Ralph FM, Shupe MD. 2014. Continental heat anomalies and the extreme melting of the greenland ice surface in 2012 and 1889. *Journal of Geophysical Research-Atmospheres* **119**(11): 6520–6536, doi:10.1002/2014jd021470.

Newell RE, Newell NE, Zhu Y, Scott C. 1992. Tropospheric rivers - a pilot-study. *Geophysical Research Letters* **19**(24): 2401–2404, doi:10.1029/92gl02916.

Nghiem SV, Hall DK, Mote TL, Tedesco M, Albert MR, Keegan K, Shuman CA, DiGirolamo NE, Neumann G. 2012. The extreme melt across the greenland ice sheet in 2012. *Geophysical Research Letters* **39**, doi:10.1029/2012gl053611.

Pfahl S, Sodemann H. 2014. What controls deuterium excess in global precipitation? *Climate of the Past* **10**(2): 771–781, doi:10.5194/cp-10-771-2014.

Samuels-Crow KE, Galewsky J, Sharp ZD, Dennis KJ. 2014. Deuterium excess in subtropical free troposphere water vapor: Continuous measurements from the chajnantor plateau, northern chile. *Geophysical Research Letters* **41**(23): 8652–8659, doi: 10.1002/2014gl062302.

Sodemann H. 2006. Tropospheric transport of water vapour: Lagrangian and eulerian perspectives. PhD thesis, Swiss Federal Institute of Technology Zurich.

Sodemann H, Schwierz C, Wernli H. 2008. Interannual variability of greenland winter precipitation sources: Lagrangian moisture diagnostic and north atlantic oscillation influence. *Journal of Geophysical Research-Atmospheres* **113**(D3), doi:10.1029/2007jd008503.

Sodemann H, Stohl A. 2013. Moisture origin and meridional transport in atmospheric rivers and their association with multiple cyclones. *Monthly Weather Review* **141**(8): 2850–2868, doi:10.1175/mwr-d-12-00256.1.

Steen-Larsen HC, Johnsen SJ, Masson-Delmotte V, Stenni B, Risi C, Sodemann H, Balslev-Clausen D, Blunier T, Dahl-Jensen D, Ellehoj MD, Falourd S, Grindsted A, Gkinis V, Jouzel J, Popp T, Sheldon S, Simonsen SB, Sjolte J, Steffensen JP, Sperlich P, Sveinbjornsdottir AE, Vinther BM, White JWC. 2013. Continuous monitoring of summer surface water vapor isotopic composition above the greenland ice sheet. *Atmospheric Chemistry and Physics* **13**(9): 4815–4828, doi:10.5194/acp-13-4815-2013.

Steen-Larsen HC, Masson-Delmotte V, Hirabayashi M, Winkler R, Satow K, Prie F, Bayou N, Brun E, Cuffey KM, Dahl-Jensen D, Dumont M, Guillevic M, Kipfstuhl S, Landais A, Popp T, Risi C, Steffen K, Stenni B, Sveinbjornsdottir AE. 2014. What controls the isotopic composition of greenland surface snow? *Climate of the Past* **10**(1): 377–392, doi:10.5194/cp-10-377-2014.

Steen-Larsen HC, Masson-Delmotte V, Sjolte J, Johnsen SJ, Vinther BM, Breon FM, Clausen HB, Dahl-Jensen D, Falourd S, Fettweis X, Gallee H, Jouzel J, Kageyama M, Lerche H, Minster B, Picard G, Punge HJ, Risi C, Salas D, Schwander J, Steffen K, Sveinbjoernsdottir AE, Svensson A, White J. 2011. Understanding the climatic signal in the water stable isotope records from the neem shallow firn/ice cores in northwest greenland. *Journal of Geophysical Research-Atmospheres* **116**, doi:10.1029/2010jd014311.

Stohl A, Seibert P. 1998. Accuracy of trajectories as determined from the conservation of meteorological tracers. *Quarterly Journal of the Royal Meteorological Society* **124**(549): 1465–1484, doi:10.1002/qj.49712454907.

Theakstone WH. 2008. Dating stratigraphic variations of ions and oxygen isotopes in a high- altitude snowpack by comparison with daily variations of precipitation chemistry at a low-altitude site. *Hydrology Research* **39**(2): 101–112, doi:10.2166/nh.2008.039.

Theakstone WH. 2011. A seven-year study of oxygen isotopes in daily precipitation at a site close to the arctic circle, tustervatn, norway: Trajectory analysis and links with the north atlantic oscillation. *Atmospheric Environment* **45**(29): 5101–5109, doi: 10.1016/j.atmosenv.2011.06.034.

Uemura R, Matsui Y, Yoshimura K, Motoyama H, Yoshida N. 2008. Evidence of deuterium excess in water vapor as an indicator of ocean surface conditions. *Journal of Geophysical Research-Atmospheres* **113**, doi:10.1029/2008jd010209.

van den Broeke MR, Smeets CJPP, van de Wal RSW. 2011. The seasonal cycle and interannual variability of surface energy balance and melt in the ablation zone of the west greenland ice sheet. *Cryosphere* **5**(2): 377–390, doi:10.5194/tc-5-377-2011.

Werner M, Heimann M, Hoffmann G. 2001. Isotopic composition and origin of polar precipitation in present and glacial climate simulations. *Tellus Series B-Chemical and Physical Meteorology* **53**(1): 53–71, doi:10.1034/j.1600-0889.2001.01154.x.